

MODERN ELECTROMAGNETIC SCATTERING

by

Alex J. Yuffa

Report Documentation Page		Form Approved OMB No. 0704-0188
Public reporting burden for the collection of information is estimated to average 1 hour per response, including the time for reviewing instructions, searching existing data sources, gathering and maintaining the data needed, and completing and reviewing the collection of information. Send comments regarding this burden estimate or any other aspect of this collection of information, including suggestions for reducing this burden, to Washington Headquarters Services, Directorate for Information Operations and Reports, 1215 Jefferson Davis Highway, Suite 1204, Arlington VA 22202-4302. Respondents should be aware that notwithstanding any other provision of law, no person shall be subject to a penalty for failing to comply with a collection of information if it does not display a currently valid OMB control number.		
1. REPORT DATE 10 AUG 2013	2. REPORT TYPE Final	3. DATES COVERED 1 Aug 2010 - 31 Dec 2016
4. TITLE AND SUBTITLE Modern Electromagnetic Scattering / PhD Dissertation		5a. CONTRACT NUMBER N/A
		5b. GRANT NUMBER N00014-10-1-0958
		5c. PROGRAM ELEMENT NUMBER N/A
6. AUTHOR(S) Alex J. Yuffa Applied Physics Colorado School of Mines		5d. PROJECT NUMBER N/A
		5e. TASK NUMBER N/A
		5f. WORK UNIT NUMBER N/A
7. PERFORMING ORGANIZATION NAME(S) AND ADDRESS(ES) Department of Physics Colorado School of Mines Golden, Colorado 80401		8. PERFORMING ORGANIZATION REPORT NUMBER 65
9. SPONSORING/MONITORING AGENCY NAME(S) AND ADDRESS(ES) Office of Naval Research (ONR) 875 North Randolph Street - Suite 1425 Code 03R Arlington, VA 22203-1995		10. SPONSOR/MONITOR'S ACRONYM(S) ONR
		11. SPONSOR/MONITOR'S REPORT NUMBER(S) N/A
12. DISTRIBUTION/AVAILABILITY STATEMENT Approved for public release, distribution unlimited		
13. SUPPLEMENTARY NOTES N/A, The original document contains color images.		

14. ABSTRACT

We develop a numerically stable algorithm for electromagnetic wave propagation through planar stratified media. This algorithm is implemented in a modern programming language and is suitable for the study of such applications as Anderson localization and perfect lensing. Our algorithm remains numerically stable even in the presence of large absorption. Furthermore, in the context of the linear response laws and causality, we analyze a vanishing absorption approximation, which is commonly used in wave scattering problems. We show that it is easy to violate causality in the frequency-domain by making the vanishing absorption approximation. We also develop an orders-of-scattering approximation, termed âscreened cylindrical void/coreâ (SCV) approximation, for wave scattering from a large host cylinder containing N eccentrically embedded core cylinders. The SCV approximation is developed via separation of variables and a cluster T -matrix. We establish the limitations of the SCV approximation and it is in good agreement with the numerically-exact solution. Furthermore, we illustrate that the large host cylinder model with N cylindrical inclusions can be used to theoretically and experimentally investigate strong multiple scattering effects in random media, such as Anderson localization.

15. SUBJECT TERMS

16. SECURITY CLASSIFICATION OF:

a. REPORT

unclassified

b. ABSTRACT

unclassified

c. THIS PAGE

unclassified17. LIMITATION
OF ABSTRACT**SAR**18. NUMBER
OF PAGES**132**19a. NAME OF
RESPONSIBLE PERSON

A thesis submitted to the Faculty and the Board of Trustees of the Colorado School of Mines in partial fulfillment of the requirements for the degree of Doctor of Philosophy (Applied Physics).

Golden, Colorado

Date _____

Signed: _____

Alex J. Yuffa

Signed: _____

Dr. John A. Scales
Thesis Advisor

Golden, Colorado

Date _____

Signed: _____

Dr. Thomas E. Furtak
Professor and Head
Department of Physics

ABSTRACT

We develop a numerically stable algorithm for electromagnetic wave propagation through planar stratified media. This algorithm is implemented in a modern programming language and is suitable for the study of such applications as Anderson localization and perfect lensing. Our algorithm remains numerically stable even in the presence of large absorption. Furthermore, in the context of the linear response laws and causality, we analyze a vanishing absorption approximation, which is commonly used in wave scattering problems. We show that it is easy to violate causality in the frequency-domain by making the vanishing absorption approximation.

We also develop an orders-of-scattering approximation, termed “screened cylindrical void/core” (SCV) approximation, for wave scattering from a large host cylinder containing N eccentrically embedded core cylinders. The SCV approximation is developed via separation of variables and a cluster T -matrix. We establish the limitations of the SCV approximation and it is in good agreement with the numerically-exact solution. Furthermore, we illustrate that the large host cylinder model with N cylindrical inclusions can be used to theoretically and experimentally investigate strong multiple scattering effects in random media, such as Anderson localization.

TABLE OF CONTENTS

ABSTRACT	iii
LIST OF FIGURES	viii
LIST OF TABLES	xi
ACKNOWLEDGMENTS	xii
CHAPTER 1 INTRODUCTION	1
1.1 One-dimensional scattering and absorption free media	2
1.2 Large host cylinder with holes	4
1.3 References Cited	6
CHAPTER 2 OBJECT-ORIENTED ELECTRODYNAMIC <i>S</i> -MATRIX CODE WITH MODERN APPLICATIONS	8
2.1 Abstract	8
2.2 Introduction	8
2.3 Background	10
2.3.1 Pathological cases at normal incidence	12
2.4 Wave propagation in stratified media	12
2.4.1 Pathological cases at oblique incidence	14
2.4.2 Origin and numerical treatment of the pathologies	14
2.5 Polarization	15
2.5.1 Parallel polarization	16
2.5.2 Perpendicular polarization	17

2.6	Linear system	18
2.6.1	S -matrix	19
2.7	Conserved quantities	20
2.7.1	Energy densities for parallel polarization	22
2.7.2	Energy densities for perpendicular polarization	23
2.8	Transmission and reflection coefficients	23
2.9	Multilayer classes	24
2.10	Python and numerical efficiency	27
2.11	Numerical stability and accuracy	28
2.12	Conclusions	30
2.13	Acknowledgment	31
2.14	References Cited	32
CHAPTER 3 LINEAR RESPONSE LAWS AND CAUSALITY IN ELECTRODYNAMICS		36
3.1	Abstract	36
3.2	Introduction	36
3.3	Background	39
3.4	Drude model	42
3.4.1	A constant electric field	43
3.4.2	A monochromatic field	44
3.5	Plasma	45
3.5.1	Plasma in a constant electric field	47
3.5.2	Plasma in a monochromatic electric field	47

3.6	Damped harmonic oscillator	47
3.7	Concluding remarks	50
3.8	Acknowledgment	51
3.9	References Cited	51
A.1	Appendix A - Distribution theory	53
A.1.1	The Fourier transform of tempered distributions	56
A.1.2	Support and structure of tempered distributions	59
CHAPTER 4 MEASURING THE VOID: THEORETICAL STUDY OF SCATTERING BY A CYLINDRICAL ANNULUS		63
4.1	Abstract	63
4.2	Introduction	63
4.3	Intuitive derivation of the SCV approximation	66
4.4	Rigorous derivation of the SCV approximation	69
4.5	Energy conservation	72
4.6	Conclusions	75
4.7	Acknowledgment	75
4.8	References Cited	75
CHAPTER 5 SCATTERING FROM A LARGE CYLINDER WITH AN ECCENTRICALLY EMBEDDED CORE: AN ORDERS-OF-SCATTERING APPROXIMATION		77
5.1	Abstract	77
5.2	Introduction	77
5.3	Background and conventions	80
5.4	Host cylinder	81

5.5	Composite cylinder	81
5.6	The SCV approximation and its physical interpretation	85
5.7	Numerical examples and limitations	87
5.8	Conclusions	91
5.9	Acknowledgment	91
5.10	References Cited	91
CHAPTER 6 GENERALIZATION OF THE SCV APPROXIMATION TO A CLUSTER OF ECCENTRICALLY EMBEDDED CORES		94
6.1	Host cylinder with and without core cylinders	95
6.2	Cluster T -matrix	98
6.3	Connection with localization and random matrices	102
6.4	Summary	105
6.5	References Cited	105
APPENDIX A - DISSERTATION DEFENSE SLIDES		107
APPENDIX B - PERMISSIONS TO USE COPYRIGHTED MATERIAL		119

LIST OF FIGURES

Figure 1.1	John A. Scales (top) and Philippe Goy (bottom) calibrating MPL's AB Millimetre VNA, which Goy designed and build	2
Figure 1.2	A schematic representation of constructive interference of three partially scattered waves is shown. The scatterers are denoted by disks and the region of constructive interference is highlighted.	2
Figure 1.3	The cross-sectional view of the planar stratified media (multilayer stack) is shown.	3
Figure 1.4	Artistic rendering (not to scale) of our millimeter-wave random medium model. The holes are shown in a simple pattern for illustration purposes only.	4
Figure 1.5	The measured amplitude and phase of the total transmitted field at 160 GHz are shown.	5
Figure 2.1	The cross-sectional view of the multilayer stack is shown. The multilayer stack consists of $p + 1$ regions made of a RHM. A parallel polarized wave is incident from a semi-infinite ambient medium (region p). The origin of the coordinate system is set on the planar interface separating regions p and $p - 1$. The 0th region is a semi-infinite substrate.	13
Figure 2.2	The ratio of total computational time required to compute $T(f_i, \phi_j)$ and $R(f_i, \phi_j)$, where $1 \leq \{i, j\} \leq 10^3$, using openTMM and a pure Fortran 90 code. Each multilayer stack is composed of the same number of pseudorandom layers of the following types: right-handed layers with/without absorption and left-handed layers with/without absorption.	29
Figure 2.3	δ_v is shown for a multilayer stack composed of the same number of pseudorandom layers of the following types: right-handed layers with/without absorption and left-handed layers with/without absorption.	30
Figure 3.1	The input signal, $S(t)$, is shown along with the output signal, $S(t) - C_1(t)$, of a system that only absorbs the $C_1(t)$ component of $S(t)$, without affecting other components.	38

Figure 4.1	The cross-sectional view of the cylindrical scattering objects is shown. The origin of the coordinate system (r, θ) , where $-\pi \leq \theta < \pi$, is concentric with the cylindrical objects. In each panel, the region is denoted by a boxed number and the permittivity of each region is also indicated. For example, region three, $r < r_2$, in panel (a) has a permittivity of ϵ_1 and region one, $r > r_2$, in panel (c) has a permittivity of ϵ_2	65
Figure 4.2	The magnitude and phase of the far-field pattern in the forward direction for a Teflon cylindrical annulus in vacuum, with an outer radius of 10 cm at 100 GHz, is shown. The permittivity of Teflon at 100 GHz is 2.05 with a negligible loss-tangent . In the computation of (4.16), we only summed the first $N = \lceil k_1 r_2 + 4(k_1 r_2)^{1/3} + 2 \rceil$ terms [3, Appendix C]	72
Figure 4.3	The rate \mathbb{W}^{ext} (normalized by $Lc/8\pi$) at which energy is extinguished by the cylindrical void from the total field outside the host cylinder is shown as a function of $k_2 r_2$. The above plot was produced with the same parameters as the ones described in the caption of Figure 4.2.	74
Figure 5.1	The cross-sectional view of the composite cylinder, with regions labeled by a number, is shown. Region 1 is the space outside of the composite cylinder ($r > a$), Region 2 is the host cylinder, and Region 3 is the core cylinder. The origin of the (r, θ) coordinate system, where $-\pi \leq \theta < \pi$, is centered on the host cylinder, and the origin of the (ρ, ϕ) coordinate system, where $-\pi \leq \phi < \pi$, is centered on the core cylinder. The axes of these two coordinate systems are parallel to each other and the center of the (ρ, ϕ) coordinate system is offset by $r_0 \cos \theta_0 \hat{\mathbf{x}} + r_0 \sin \theta_0 \hat{\mathbf{y}}$ with respect to the origin of the (r, θ) coordinate system.	78
Figure 5.2	The spectral radius of \mathbf{F} at 100 GHz for a Teflon host cylinder ($a = 10$ cm) with an eccentrically embedded quartz core cylinder is shown as a function of $ k_3 b$, and eccentricity, r_0/a (with $\theta_0 = 0$). The permittivity of Teflon and quartz at 100 GHz is 2.1 and 3.8 with a negligible loss-tangent , respectively.	85
Figure 5.3	The relative error in Q^{ext} (in percent) is shown as a function of $ k_3 b$ and eccentricity, r_0/a , for various θ_0 angles. The top row shows the relative error if only the $\ell = 0$ term is retained in (5.13), i.e., the SCV approximation, and the bottom row shows the relative error if the $\ell = 0$ and $\ell = 1$ terms are retained. The above plot was produced with the same parameters as the ones described in the caption of Figure 5.2	89

Figure 5.4 The spectral radius of \mathbf{F} at eigenfrequency 99.823859 GHz is shown as a function $|k_3|b$ and eccentricity, r_0/a (with $\theta_0 = 0$). The above plot was produced with the same parameters as the ones described in the caption of Figure 5.2 90

Figure 6.1 The cross-sectional view of the composite cylinder is shown. Region $N + 2$ is the space outside of the composite cylinder ($r > a$), region $N + 1$ is the host cylinder, and regions $1, \dots, N$ are the core cylinders. The origin of the global (r, θ) coordinate system, where $-\pi \leq \theta < \pi$, is centered on the host cylinder, and the origin of the local (ρ_i, ϕ_i) coordinate system, where $-\pi \leq \phi_i < \pi$, is centered on the i th core cylinder. The axes of the (r, θ) and (ρ_i, ϕ_i) coordinate systems are parallel to each other and the center of the (ρ_i, ϕ_i) coordinate system is offset by \mathbf{r}_i with respect to the origin of the (r, θ) coordinate system. . . . 95

LIST OF TABLES

Table 2.1	The first column contains the name (as it appears in the code) of the object attribute (method) of the class Layer , the second column contains a description of the method, and the third column contains references to the section where a more detailed description may be found.	25
Table 2.2	The first column contains the name (as it appears in the code) of the object attribute of the class Boundary , the second column contains a description of the attribute, and the third column contains references to a section and/or equation where a more detailed description of the attribute may be found.	26
Table 2.3	The height, h , relative permittivity, ϵ_{rel} , and the relative permeability, μ_{rel} , of each layer were pseudorandomly chosen from the intervals shown in the table. E.G., from the second line of the table, we see that 125 layers have thickness between 1 mm and 10 mm, and relative permittivity/permeability between -10 and -1 . A 500-layer stack was used for the Poynting theorem and the FIM test. For the de Hoop reciprocity theorem test, a multilayer stack consisting of 5, 9, 13, . . . , 501 layers was used.	31
Table 3.1	A brief description of the symbols introduced in the appendix.	41

ACKNOWLEDGMENTS

They say it takes a village to raise a kid; well, it took a lot more than that to raise me. To thank every individual who has helped to get me to this point in my life would deforest the Amazon rainforest. Be that as it may, I must thank some individuals here, as without them, this final academic endeavor wouldn't have been possible at all.

I would like to thank Dr. Frank V. Kowalski, Dr. Paul A. Martin, Dr. John A. Scales, Dr. Craig P. Taylor, and Dr. David M. Wood for serving on my Thesis Committee and for partaking in many helpful discussions. I'm particularly thankful to:

- Dr. Kowalski for introducing me to the beauty of wave interference through the swimming pool field trip;
- Dr. Wood for his very entertaining lectures and brutal homeworks. The latter was an awesome preparation for the frustration that research brings, and the former turned sorrow into blissfulness;
- Dr. Martin for his almost inhuman mastery and knowledge of multiple scattering that he has so selflessly shared with me over the years.

I am especially grateful to my angelic advisor Dr. John A. Scales for opening my eyes to all walks of life in Physics. John not only painstakingly taught me about theoretical, computational, and experimental physics, but also showed me how to think. I will cherish all of our conversations in the group office and his patience with me. I will never be able to properly thank John for everything that he has done for me, as it goes well beyond Physics. For example, how do I thank John for motivating and helping me to quit smoking? Or for his endless encouragement when I was down? I will forever be in your debt, John, as it is simply impossible to even describe the positive impact you have had on my life. Thank you John for being such a great mentor and friend.

Having spent most of my formative years (with $N \gg 1$) imprisoned inside the four walls of Meyer Hall, I must express my most sincere gratitude to Dr. John A. DeSanto, Dr. Bill Law, and Dr. Jim A. McNeil for their care and support. I must also say the most majestic thank you to Matt Berg, Jason Dardano, Hans Ecke, Mike Fellingner, Alan Martin, Barbara Pratt-Johnson, Jennifer Strong, and Scott Strong for greatly improving my life inside and outside those four walls for the last N years.

All of the above would not have been possible if I didn't have the most supportive and understanding family in the universe. My sister, Anna Neimark, who is my endless source of inspiration and has been my editor-in-chief throughout my academic endeavors. My parents, Irene Yuffa-Neymark and Leonid Neymark, whose unconditional love and support has enabled me to reach this point in my life. My grandparents, Vladimir Jouravlev and the late Valentina Jouravleva, who have planted in me the thirst for knowledge and taught me the value of perseverance. My love, Irina Pomirchy, whose kindness, understanding, and empathy made the last thrust toward a Ph.D. possible. Thank you all!

CHAPTER 1

INTRODUCTION

It has over 150 years since James Clerk Maxwell published the much-celebrated equations that now bear his name. He probably could not have imagined that, in the 21st century, his equations would be utilized to study various wave scattering phenomena. The main goal of this dissertation is to use Maxwell's equations to design multiple scattering experiments that can be realized in the Mesoscopic Physics Laboratory (MPL) at the Colorado School of Mines. These modeled experiments not only need to be theoretically sound, but they also need to be computationally and experimentally verifiable. At the MPL, we have the rare ability to measure *both* the amplitude and the phase of electric fields at frequencies approaching 1 THz with the AB Millimetre millimeter/sub-millimeter Vector Network Analyzer (VNA), see Figure 1.1. This unique ability allows us to study one of the most fascinating multiple scattering phenomena, namely, the localization of electromagnetic waves. Fifty years after the publication of Anderson's seminal work [1], localization continues to be a thriving area of research in theoretical and experimental physics [2–7].

Localization, a coherent multiple scattering effect, has been observed in a variety of classical and quantum mechanical systems. To gain a pictorial understanding of how a wave may become spatially localized, consider a wave, $U^{(\text{inc})}(\mathbf{r})$, incident on a medium composed of N identical and lossless scatterers randomly distributed in space. The total wave, $U^{(\text{total})}(\mathbf{r})$, is the sum of the incident and partially scattered waves, i.e., $U^{(\text{total})}(\mathbf{r}) = U^{(\text{inc})}(\mathbf{r}) + \sum_{i=1}^N U^{(i)}(\mathbf{r})$, where $U^{(i)}(\mathbf{r})$ is the wave scattered by the i th scatterer. These waves may interfere constructively in some region of space (see Figure 1.2) and destructively in other regions of space, thus localizing $U^{(\text{total})}(\mathbf{r})$ in space.

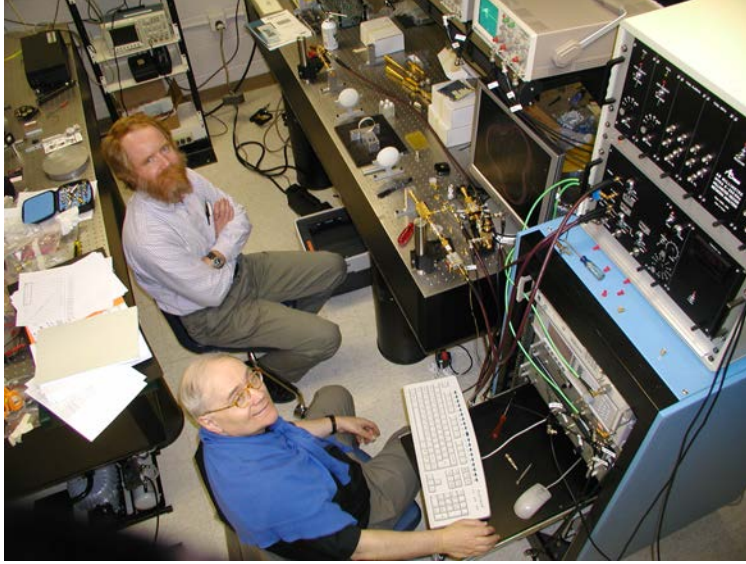


Figure 1.1: John A. Scales (top) and Philippe Goy (bottom) calibrating MPL’s AB Millimetre VNA, which Goy designed and build [8].

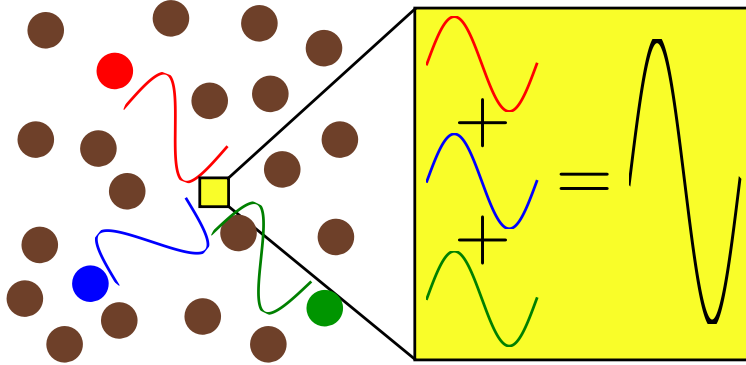


Figure 1.2: A schematic representation of constructive interference of three partially scattered waves is shown. The scatterers are denoted by disks and the region of constructive interference is highlighted.

1.1 One-dimensional scattering and absorption free media

The first use of the VNA at the MPL was to study localization in planar stratified media (see Figure 1.3) composed of 100 randomly shuffled quartz and Teflon layers [7]. In the course of this study, it became apparent that the standard transfer matrix algorithm [9–11] used to compute the electromagnetic field inside the multilayer stack is numerically unstable. The root cause of the numerical instability is that the transfer matrix contains

exponentially increasing and decreasing terms when absorption is non zero. In Chapter 2, we present a numerically stable algorithm for a multilayer stack, which we have developed and implemented in a modern object-oriented programming language. Furthermore, we discuss some pathological cases that arise in the limit of vanishing absorption. These cases are important as they vividly demonstrate that there is no physical principle that can be used to differentiate between a right-handed material and a left-handed material¹ if absorption is assumed to be zero.

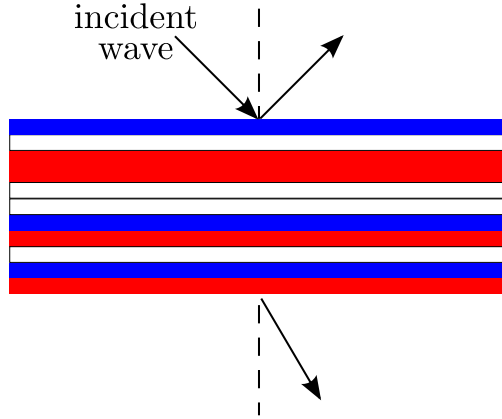


Figure 1.3: The cross-sectional view of the planar stratified media (multilayer stack) is shown.

The common zero absorption approximation is further investigated in Chapter 3 from a more general point of view. In particular, a connection between absorption and causality (the effect cannot precede the cause) is established in the context of linear response laws. Furthermore, through the use of the formal theory of tempered distributions, we establish significant differences between the frequency-domain and monochromatic time-domain Maxwell equations. This is important because although all the scattering problems in this dissertation are formulated in the frequency-domain, the actual VNA measurements are performed in the time-domain with a monochromatic incident field. As shown in Chapter 3, confusing the two domains leads to an apparent violation of causality.

¹It is customary, but historically inaccurate, to attribute the first theoretical consideration of the left-handed material to Veselago [12]. In fact, as Agranovich and Gartstein point out, such a material was theoretically considered much earlier by Mandel'shtam, see [13, §2.1] and references therein.

1.2 Large host cylinder with holes

At the MPL, we are currently fabricating a model of a millimeter-wave random medium from a large cylinder of Teflon (ultra low-loss material) with approximately 5000 holes drilled in a random pattern using a table-top three-axis CNC milling machine. The cylinder is 110 mm in length and has a diameter of 152.4 mm. The holes are 0.505 mm in diameter and are separated by a distance of 0.101 mm, giving us roughly two/three scatterers per wavelength, as required by the Ioffe–Regel criterion [14, §7.4.4] for localization. The holes are large enough to allow for the possibility of placing an intensity detector in them, thereby measuring $|U^{(\text{total})}|^2$ *inside* the sample. Our model, shown in Figure 1.4, can be illuminated from the side to make a two-dimensional system or from the end to study transverse localization. Furthermore, by illuminating the sample from the side and putting it on a rotational stage, we can generate essentially arbitrary realizations of the same random disorder. In this dissertation, we will only consider illumination from the side; however, it is important to realize that the above model is more versatile than considered here.

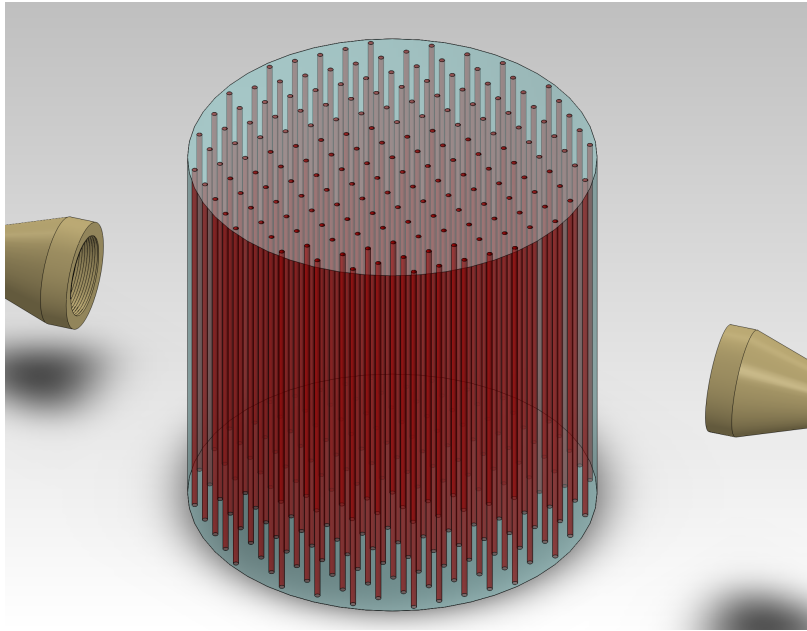


Figure 1.4: Artistic rendering (not to scale) of our millimeter-wave random medium model. The holes are shown in a simple pattern for illustration purposes only.

In order to ensure that the VNA has enough sensitivity to detect the presence of such small holes, we measured the total field in the forward direction as a function of distance with and without one concentric hole. The results of this experiment are shown in Figure 1.5, from which we clearly see that the VNA can unambiguously detect the presence of a small hole inside a large Teflon cylinder.

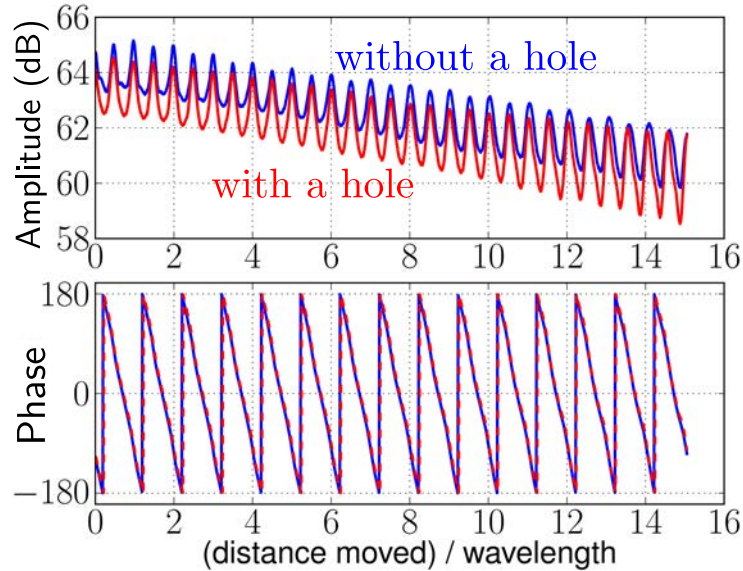


Figure 1.5: The measured amplitude and phase of the total transmitted field at 160 GHz are shown.

We believe that, in order to learn the most from the aforementioned experiments, it is necessary to have a sound theoretical model for them. The theoretical model should be realistic but computationally tractable, without many crude numerical approximations. It is possible to model our ensemble of scatterers using integral equation methods [15–17] or coupled-dipole methods [18, 19], but such methods are not computationally feasible because they yield a linear system of equations that is too large. For example, it is common practice to use supercomputers with the coupled-dipole method to model even a few scatterers of wavelength size [19]. Instead, in Chapters 4–6, we have developed an orders-of-scattering approximation based on separation of variables and a cluster T -matrix [20, 21] [22, §5.9] [23, §7.11]. This development is done in stages, as described below.

In Chapter 4, we develop an approximation, termed the screened cylindrical void/core (SCV) approximation, for a large cylinder with one concentric hole. The SCV approximation is first derived in a physically intuitive manner, and then in a mathematically rigorous manner. In Chapter 5, the SCV approximation is extended to the case of a non-concentric hole and we explicitly show that the SCV approximation can be viewed as an orders-of-scattering approximation. Furthermore, the limitations of the SCV approximation are discussed and demonstrated with explicit numerical examples. Finally, in Chapter 6, we generalize the SCV approximation to N non-concentric holes inside the large cylinder via the cluster T -matrix and suggest avenues for future research.

1.3 References Cited

- [1] P. W. Anderson, Absence of diffusion in certain random lattices, *Phys. Rev.* 109 (1958) 1492–1505.
- [2] A. Lagendijk, B. van Tiggelen, D. S. Wiersma, Fifty years of Anderson localization, *Physics Today* 62 (2009) 24–29.
- [3] S. S. Kondov, W. R. McGehee, J. J. Zirbel, B. DeMarco, Three-dimensional Anderson localization of ultracold matter, *Science* 334 (2011) 66–68.
- [4] G. Roati, C. D’Errico, L. Fallani, M. Fattori, C. Fort, M. Zaccanti, G. Modugno, M. Modugno, M. Inguscio, Anderson localization of a non-interacting Bose-Einstein condensate, *Nature* 453 (2008) 895–898.
- [5] H. Hu, A. Strybulevych, J. H. Page, S. E. Skipetrov, B. A. van Tiggelen, *Nat. Phys.* 4 (2008) 945–948.
- [6] A. A. Chabanov, A. Z. Genack, Photon localization in resonant media, *Phys. Rev. Lett.* 87 (2001) 153901.
- [7] J. A. Scales, L. D. Carr, D. B. McIntosh, V. Freilikher, Y. P. Bliokh, Millimeter wave localization: Slow light and enhanced absorption in random dielectric media, *Phys. Rev. B* 76 (2007) 085118.
- [8] P. H. Siegel, Terahertz pioneer: Philippe Goy “If you agree with the majority, you might be wrong”, *Terahertz Science and Technology, IEEE Transactions on* 3 (2013) 348–353.

- [9] R. L. Mooney, An exact theoretical treatment of reflection-reducing optical coatings, *J. Opt. Soc. Am.* 35 (1945) 574–583.
- [10] W. Weinstein, The reflectivity and transmissivity of multiple thin coatings, *J. Opt. Soc. Am.* 37 (1947) 576–577.
- [11] F. Abelès, La théorie générale des couches minces, *J. Phys. Radium* 11 (1950) 307–310.
- [12] V. G. Veselago, The electrodynamics of substances with simultaneously negative values of ϵ and μ , *Soviet Physics Uspekhi* 10 (1968) 509–514.
- [13] V. M. Agranovich, Y. N. Gartsstein, Spatial dispersion and negative refraction of light, *Phys. Usp.* 49 (2006) 1029–1044.
- [14] P. Sheng, Introduction to Wave Scattering, Localization and Mesoscopic Phenomena, Springer, Berlin, second edition, 2006.
- [15] J. A. Stratton, L. J. Chu, Diffraction theory of electromagnetic waves, *Phys. Rev.* 56 (1939) 99–107.
- [16] D. Colton, R. Kress, Integral equation methods in scattering theory, Wiley, New York, 1983.
- [17] K. E. Atkinson, The numerical solution of integral equations of the second kind, University Press, Cambridge, 1997.
- [18] B. T. Draine, P. J. Flatau, Discrete-dipole approximation for scattering calculations, *J. Opt. Soc. Am. A* 11 (1994) 1491–1499.
- [19] M. A. Yurkin, A. G. Hoekstra, The discrete dipole approximation: An overview and recent developments, *J. Quant. Spectrosc. Radiat. Transf.* 106 (2007) 558–589.
- [20] B. Peterson, S. Ström, Matrix formulation of acoustic scattering from an arbitrary number of scatterers, *J. Acoust. Soc. Am.* 56 (1974) 771–780.
- [21] R. Lim, R. H. Hackman, A formulation of multiple scattering by many bounded obstacles using a multicentered, T supermatrix, *J. Acoust. Soc. Am.* 91 (1992) 613–638.
- [22] M. I. Mishchenko, L. D. Travis, A. A. Lacis, Scattering, Absorption, and Emission of Light by Small Particles, Cambridge University Press, Cambridge, 2002.
- [23] P. A. Martin, Multiple Scattering, Cambridge University Press, Cambridge, 2006.

CHAPTER 2

OBJECT-ORIENTED ELECTRODYNAMIC S -MATRIX CODE WITH MODERN APPLICATIONS

A paper published in the *Journal of Computational Physics*.

Alex J. Yuffa^{*}, John A. Scales

Department of Physics, Colorado School of Mines, Golden, CO 80401, USA

^{*}Primary researcher and author. E-mail: ayuffa@gmail.com

2.1 Abstract

The S -matrix algorithm for the propagation of an electromagnetic wave through planar stratified media has been implemented in a modern object-oriented programming language. This implementation is suitable for the study of such applications as the Anderson localization of light and super-resolution (perfect lensing). For our open-source code to be as useful as possible to the scientific community, we paid particular attention to the pathological cases that arise in the limit of vanishing absorption.

2.2 Introduction

Electromagnetic wave propagation through planar stratified media (multilayer stack) is a century old problem in physics [1, 2]. It may be somewhat surprising that it is still relevant today. In fact, it has only relatively recently been discovered that the transmission and reflection coefficients for a multilayer stack may be written down without any computations by using a complex version of the elementary symmetric functions [3, 4]. It has also been recently discovered that the complex reflection coefficients follow the generalized version of the composition law used to add parallel velocities in the theory of special relativity, see [5, 6] and Refs. within. It is possible to use the aforementioned properties to formulate a numerical wave propagation algorithm in planar stratified media as was done in [7], yet the

resulting algorithm appears to be numerically unstable. The more traditional approach of the late 1940s, namely, the transfer matrix algorithm [8–11], is also numerically unstable. Both algorithms are numerically unstable because they contain exponentially increasing and decreasing terms, see Section 2.6. There also exists an R -matrix algorithm [12–15], but it is only conditionally stable (for reasons different from above) [12, 15]. We use a simple version of the S -matrix algorithm, which is numerically stable [15–19]. Before considering the details of the S -matrix algorithm and the need for its open-source implementation in a modern object-oriented language, we briefly mention some of the current applications we had in mind when we wrote the code.

In 1968, Veselago [20] considered a hypothetical non-active material in which the real parts of the permittivity and permeability are simultaneously negative; we refer to such a material as a *left-handed material* (LHM), but it is also known as a *negative refractive material*. It was only in the early 2000’s that such an artificial material was fabricated [21, 22], leading to an explosion of papers on the LHM, see [23] and Refs. within. One of the intriguing properties of the LHM is the ability to image with a sub-wavelength image resolution (super-resolution if you will), which has been proposed and studied in the context of a multilayer stack [24, 25]. Another general area of application is the Anderson localization of light [26, 27], which has been studied both theoretically and experimentally by Scales et al. [28], who considered wave propagation at normal incidence through a multilayer stack made of quartz and Teflon wafers. The effects of total internal reflection on light localization in a random multilayer stack at oblique incidence have also been studied under the assumption of complete phase randomization [29] along with the effects of the LHM on localization [30]. Other applications include the study of asymmetrical properties of light in a Fabry-Pérot interferometer [31, 32].

In all of the above applications, the S -matrix algorithm was or could have been used; however, to the best of our knowledge, an open-source and object-oriented implementation of the S -matrix algorithm suitable for the LHM as well as the right-handed material (RHM)

(where the real parts of the permittivity and permeability are *not* simultaneously negative) is currently unavailable. Almost certainly, there are many “in-house” implementations of some version of the algorithms discussed above being passed around among colleagues. We suspect that some users of these “in-house” algorithms may be unaware of the numerical stability issues and of pathological cases where the numerical implementation is not clear, as discussed in Section 2.4. Moreover, in the context of reproducibility of scientific work, it is important to have an open-source and publicly available implementation.

This paper is self-contained as much as possible in order for our implementation of the S -matrix algorithm to be useful to the widest possible scientific community. We also point out the benefits and drawbacks of using a high-level programming language called Python for implementing our code, see Section 2.10.

2.3 Background

The source-free macroscopic Maxwell equations with assumed harmonic time dependence, $\exp(-i\omega t)$, in the Système International (SI) unit system, at every ordinary point in space, are:

$$\nabla \cdot \mathbf{D} = 0, \quad \nabla \cdot \mathbf{B} = 0, \quad (2.1a)$$

$$\nabla \times \mathbf{E} = i\omega \mathbf{B}, \quad \nabla \times \mathbf{H} = -i\omega \mathbf{D}, \quad (2.1b)$$

where \mathbf{E} is the electric field, \mathbf{D} is the displacement field, \mathbf{B} is the magnetic field, \mathbf{H} is the magnetic intensity, and ω is the angular frequency. By an ordinary point in space, we mean a point in space in whose “neighborhood” the physical properties of the medium are continuous. Thus, strictly speaking, one cannot apply Maxwell’s equations at a surface that separates two physically different media. If the medium is isotropic and homogeneous, then $\mathbf{D} = \epsilon \mathbf{E}$ and $\mathbf{B} = \mu \mathbf{H}$, where ϵ and μ are the permittivity and the permeability, respectively. Permittivity must satisfy the Kramers–Kronig relations and is therefore a complex-valued function of angular frequency. The same is true for permeability. Thus, in general, we have $\epsilon = \epsilon(\omega) \in \mathbb{C}$ and $\mu = \mu(\omega) \in \mathbb{C}$.

The source-free macroscopic Maxwell equations are first-order linear partial differential equations (PDEs) that must be supplemented by some boundary conditions. The conventional boundary conditions for a source-free interface separating two media (1 and 2) are:

$$\mathbf{n} \cdot (\mathbf{D}^{(2)} - \mathbf{D}^{(1)}) = 0, \quad \mathbf{n} \cdot (\mathbf{B}^{(2)} - \mathbf{B}^{(1)}) = 0, \quad (2.2a)$$

$$\mathbf{n} \times (\mathbf{E}^{(2)} - \mathbf{E}^{(1)}) = \mathbf{0}, \quad \mathbf{n} \times (\mathbf{H}^{(2)} - \mathbf{H}^{(1)}) = \mathbf{0}, \quad (2.2b)$$

where \mathbf{n} is a unit normal to the interface, and the superscript on the fields indicates from which medium the interface is approached.

Taking the curl of (2.1b), then simplifying the result using the $\nabla \times (\nabla \times \mathbf{A}) = \nabla (\nabla \cdot \mathbf{A}) - \nabla^2 \mathbf{A}$ vector identity and (2.1a), we obtain the vector Helmholtz equation within each layer

$$(\nabla^2 + k^2) \begin{Bmatrix} \mathbf{E} \\ \mathbf{H} \end{Bmatrix} = \mathbf{0}, \quad (2.3)$$

where k is the complex wavenumber, and $k^2 = \mu\epsilon\omega^2$. In general, $k^2 \neq kk^*$, where $*$ denotes the complex conjugate, and the computation of k from k^2 must be done with extreme care. For example, the permittivity and permeability for an absorbing material are taken to be $\epsilon = \epsilon' + i\epsilon''$ and $\mu = \mu' + i\mu''$, respectively, where $\{\epsilon', \mu'\} \in \mathbb{R}$, $\{\epsilon'', \mu''\} \in \mathbb{R}^+$ and \mathbb{R}^+ denotes the positive real numbers.² Let $\epsilon = |\epsilon|e^{i\theta_\epsilon}$ and $\mu = |\mu|e^{i\theta_\mu}$, where $\{\theta_\epsilon, \theta_\mu\} \in [0, \pi]$.³ Then

$$k^2 = \epsilon\mu\omega^2$$

$$k = \sqrt{|\epsilon||\mu|}\omega e^{i\left(\frac{\theta_\epsilon + \theta_\mu + 2\pi n}{2}\right)}, \quad n = 0, 1, \quad (2.4)$$

where $\omega > 0$. The choice of the root in (2.4) is dictated by the physical requirement that, in an absorbing medium, the wave must decay and not exponentially grow. Let $k = k' + ik''$, $\{k', k''\} \in \mathbb{R}$. Without loss of generality, consider a plane wave propagating in the *positive* x -direction; then, we have $e^{i(kx - \omega t)} = e^{-k''x}e^{i(k'x - \omega t)}$. Therefore, k'' must be *greater*

²For the $\exp(+i\omega t)$ time dependence, $\epsilon = \epsilon' - i\epsilon''$, $\mu = \mu' - i\mu''$, where $\{\epsilon', \mu'\} \in \mathbb{R}$, $\{\epsilon'', \mu''\} \in \mathbb{R}^+$.

³We always mean the *positive* square root of x when we write \sqrt{x} , where $x \in \mathbb{R}^+$. The fundamental issue with the $w = z^{\frac{1}{2}}$ mapping is that the “square root” function has *branch points* at $z = 0$ and $z = \infty$ and thus must have a *branch cut* connecting the two branch points, see [33, vol. 1, Sec. 54].

than zero in order for the wave to decay in the positive x -direction.

2.3.1 Pathological cases at normal incidence

In the case of a perfect dielectric ($\epsilon'' = 0$ and $\mu'' = 0$), the rule for choosing a physically appropriate root in (2.4) may be established by taking the limit as absorption goes to zero.

Consider an almost perfect dielectric made of the RHM. Let $\epsilon = |\epsilon|e^{i\theta_\epsilon}$, $\mu = |\mu|e^{i\theta_\mu}$, where θ_ϵ and θ_μ are infinitesimally small *positive* numbers, then $\frac{\theta_\epsilon + \theta_\mu}{2} \ll \pi$ and $\frac{\theta_\epsilon + \theta_\mu}{2} + \pi > \pi$. Thus, we must choose the $n = 0$ root in (2.4), i.e., $k = \sqrt{|\epsilon||\mu|}e^{i(\frac{\theta_\epsilon + \theta_\mu}{2})}\omega$. In the case of a truly perfect dielectric (at fixed frequency), we may take the limit as θ_ϵ and θ_μ approach zero to obtain $k = \sqrt{|\epsilon||\mu|}\omega$.

In the case of an almost perfect dielectric made of a LHM: Let $\epsilon = |\epsilon|e^{i\theta_\epsilon}$, $\mu = |\mu|e^{i\theta_\mu}$, where θ_ϵ and θ_μ are slightly *less than* π , then $\frac{\theta_\epsilon + \theta_\mu}{2} < \pi$ and $\frac{\theta_\epsilon + \theta_\mu}{2} + \pi > \pi$. Thus, we must again choose the $n = 0$ root in (2.4), i.e., $k = \sqrt{|\epsilon||\mu|}e^{i(\frac{\theta_\epsilon + \theta_\mu}{2})}\omega$. For a truly perfect dielectric (at fixed frequency), we may take the limit as θ_ϵ and θ_μ approach π to obtain $k = \sqrt{|\epsilon||\mu|}e^{i\pi}\omega = -\sqrt{|\epsilon||\mu|}\omega$. Notice that for the LHM with zero absorption, $k < 0$, and for the RHM with zero absorption, $k > 0$.

2.4 Wave propagation in stratified media

Consider the three-dimensional space divided into $p + 1$ regions. The regions are infinite in the yz -plane, see Figure 2.1.

The interfaces separating the regions are assumed to be perfectly planar (yz -plane). The regions $\ell = 0, \dots, p - 1$ are assumed to be isotropic and homogeneous with a complex permittivity, ϵ_ℓ , and complex permeability, μ_ℓ . The region p is assumed to be isotropic and homogeneous with real permittivity, ϵ_p , and real permeability, μ_p . In other words, we have $\{\epsilon_\ell, \mu_\ell\} \in \mathbb{C}$ for $\ell = 0, \dots, p - 1$ and $\{\epsilon_p, \mu_p\} \in \mathbb{R}$.

A monochromatic plane wave in the ℓ th region is given by

$$\begin{Bmatrix} \mathbf{E}_\ell(\mathbf{r}, t) \\ \mathbf{H}_\ell(\mathbf{r}, t) \end{Bmatrix} = \begin{Bmatrix} \mathbf{E}_\ell \\ \mathbf{H}_\ell \end{Bmatrix} e^{i(\mathbf{k}_\ell \cdot \mathbf{r} - \omega t)}, \quad \ell = 0, \dots, p, \quad (2.5)$$

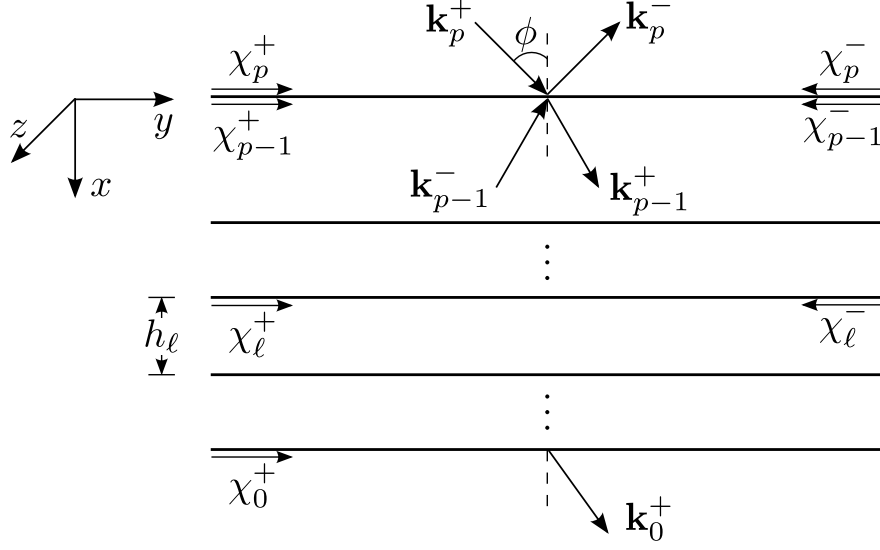


Figure 2.1: The cross-sectional view of the multilayer stack is shown. The multilayer stack consists of $p + 1$ regions made of a RHM. A parallel polarized wave is incident from a semi-infinite ambient medium (region p). The origin of the coordinate system is set on the planar interface separating regions p and $p - 1$. The 0th region is a semi-infinite substrate.

where $\mathbf{r} = x \hat{\mathbf{x}} + y \hat{\mathbf{y}} + z \hat{\mathbf{z}}$, $\{\mathbf{E}_\ell, \mathbf{H}_\ell\}$ are the *complex* vector amplitudes, $\mathbf{k}_\ell = k_{x,\ell} \hat{\mathbf{x}} + k_{y,\ell} \hat{\mathbf{y}} + k_{z,\ell} \hat{\mathbf{z}}$ is the *complex* wavevector. It is clear that (2.5) satisfies (2.3) if

$$\mathbf{k}_\ell \cdot \mathbf{k}_\ell = k_{x,\ell}^2 + k_{y,\ell}^2 + k_{z,\ell}^2 = k_\ell^2 = \epsilon_\ell \mu_\ell \omega^2. \quad (2.6)$$

Without loss of generality, we can set $k_{z,\ell} = 0$ because we can always rotate the coordinate system so that the y -axis is parallel to the part of the \mathbf{k} vector that lies in the yz -plane, see Figure 2.1.⁴ The solution given by (2.5) in each region must also satisfy the boundary conditions given by (2.2). Substituting (2.5) into (2.2) yields,

$$k_{y,p} = k_{y,\ell}, \quad \ell = 0, \dots, p - 1, \quad (2.7)$$

where $k_{y,p} \in \mathbb{R}$ because we have assumed that the region p has real permittivity and permeability. Therefore, from (2.7) we have $k_{y,\ell} \in \mathbb{R}$, but note that in general, $k_{x,\ell} \in \mathbb{C}$ for

⁴We could have chosen to set $k_{y,\ell} = 0$, and then rotated the coordinate system so that the z -axis is parallel to the part of the \mathbf{k} vector that lies in the yz -plane. The point is that \mathbf{k} can always be made into a two-dimensional vector.

$\ell = 0, \dots, p-1$. Using (2.6) and (2.7) yields

$$k_{x,\ell} = (\epsilon_\ell \mu_\ell \omega^2 - k_{y,p}^2)^{1/2} \quad \text{with} \quad \text{Im}[k_{x,\ell}] > 0 \quad (2.8)$$

for $\ell = 0, \dots, p$, where Im denotes the imaginary part, and the root choice, $\text{Im}[k_{x,\ell}] > 0$, is dictated by the decaying wave requirement, see Section 2.3.

2.4.1 Pathological cases at oblique incidence

It is clear from (2.8) that if $\epsilon_\ell'' = 0$, $\mu_\ell'' = 0$ and $\epsilon_\ell \mu_\ell \omega^2 > k_{y,p}^2$, then the root choice is not resolved by the $\text{Im}[k_{x,\ell}] > 0$ requirement. In order to resolve the root choice, we proceed by taking a limit as absorption goes to zero just as we did in Section 2.3.1. For the RHM, let $\epsilon_\ell = |\epsilon_\ell| e^{i\theta_{\epsilon_\ell}}$, $\mu_\ell = |\mu_\ell| e^{i\theta_{\mu_\ell}}$ and for the LHM, let $\epsilon_\ell = |\epsilon_\ell| e^{i(\pi - \theta_{\epsilon_\ell})}$, $\mu_\ell = |\mu_\ell| e^{i(\pi - \theta_{\mu_\ell})}$, where θ_{ϵ_ℓ} and θ_{μ_ℓ} are infinitesimally small *positive* numbers. Then $k_{x,\ell}^2$ can be approximately written as $k_{x,\ell}^2 \approx |A| e^{\pm i\gamma}$, where $0 \leq \gamma \ll \pi$, $\lim_{\{\epsilon_\ell'', \mu_\ell''\} \rightarrow 0} \gamma = 0$, and the positive (negative) sign in the exponential corresponds to the RHM (LHM). Thus, we have

$$\text{Im}[k_{x,\ell}] = \sqrt{|A|} \left\{ \sin\left(\frac{\pm\gamma}{2}\right), \sin\left(\frac{\pm\gamma}{2} + \pi\right) \right\},$$

where it is clear that for the RHM (LHM) the first (second) root must be chosen in order for $\text{Im}[k_{x,\ell}] > 0$. Therefore, if $\epsilon_\ell'' = 0$, $\mu_\ell'' = 0$ and $\epsilon_\ell \mu_\ell \omega^2 > k_{y,p}^2$, then for the RHM we have $k_{x,\ell} = +\sqrt{|\epsilon_\ell| |\mu_\ell| \omega^2 - k_{y,p}^2}$, and for the LHM we have $k_{x,\ell} = -\sqrt{|\epsilon_\ell| |\mu_\ell| \omega^2 - k_{y,p}^2}$.

2.4.2 Origin and numerical treatment of the pathologies

The limiting procedure carried out in Section 2.3.1 and 2.4.1 appears to be reasonable, but unfortunately, it is also not physically attainable, even in principle! If we view $\epsilon(\omega)$ and $\mu(\omega)$, where $\omega = \omega' + i\omega''$, in the context of the Kramers–Kronig relations, then $\epsilon(\omega)$ and $\mu(\omega)$ are analytic functions in the upper-half ω -plane. Furthermore, it can be shown that $\epsilon(\omega)$ and $\mu(\omega)$ are never purely real for any finite ω except for $\omega' = 0$ (positive imaginary axis), e.g., see [34, Section 123] and [35, Section 82]. Therefore, the common practice of replacing $\epsilon' + i\epsilon''$ by ϵ' and $\mu' + i\mu''$ by μ' even in an infinitesimally small ω' interval *cannot* be justified. Moreover, by considering the *global* behavior of $k_{x,\ell}$ it can be shown that for a

non-active medium $k_{x,\ell}$ is never zero [36]. However, we see from (2.8) that $k_{x,\ell}$, for any $\ell \neq p$ may be equal to zero if ϵ_ℓ and μ_ℓ are purely real. Of course, this case only occurs when the angle of incidence precisely equals one of the critical angles, and from the global properties of ϵ and μ we see that such angles *cannot* exist.

The above discussion suggests that the pathological cases only occur in an *unphysical* approximation, i.e., $\epsilon \approx \epsilon'$ and $\mu \approx \mu'$. In our numerical code, the user may select how to deal with the pathologies from the following two schemes:

1. If a region contains purely real permittivity and permeability, then the real permittivity and permeability are replaced by a slightly absorbing permittivity and permeability, respectively, i.e., for $\ell \neq p$, $\epsilon'_\ell \rightarrow \epsilon'_\ell + i\epsilon''_\ell$ and $\mu'_\ell \rightarrow \mu'_\ell + i\mu''_\ell$, where ϵ''_ℓ and μ''_ℓ are small positive numbers.
2. If a region contains purely real permittivity and permeability, then the $k_{x,\ell}$ is computed as describe in Section 2.3.1 and 2.4.1. If this scheme is chosen, then the code may produce erroneous results at or very near the critical angles.

2.5 Polarization

The most general polarization state is an *elliptical* polarization state. However, there is no need to consider this general case because an elliptical polarization state can always be decomposed into a linear combination of two linearly independent polarization states, namely, the *parallel* polarization state and the *perpendicular* polarization state. In what follows, it is convenient to express $\mathbf{E}_\ell(\mathbf{r}, t)$ and $\mathbf{H}_\ell(\mathbf{r}, t)$ in terms of each other by substituting (2.5) into (2.1b) (with $\mathbf{D}_\ell = \epsilon_\ell \mathbf{E}_\ell$) and using the vector identity

$$\nabla \times \begin{Bmatrix} \mathbf{E}_\ell(\mathbf{r}, t) \\ \mathbf{H}_\ell(\mathbf{r}, t) \end{Bmatrix} = i\mathbf{k}_\ell \times \begin{Bmatrix} \mathbf{E}_\ell \\ \mathbf{H}_\ell \end{Bmatrix} e^{i(\mathbf{k}_\ell \cdot \mathbf{r} - \omega t)},$$

to obtain

$$\mathbf{E}_\ell(\mathbf{r}, t) = -\frac{\mathbf{k}_\ell \times \mathbf{H}_\ell(\mathbf{r}, t)}{\epsilon_\ell \omega}, \quad (2.9a)$$

$$\mathbf{H}_\ell(\mathbf{r}, t) = \frac{\mathbf{k}_\ell \times \mathbf{E}_\ell(\mathbf{r}, t)}{\mu_\ell \omega}. \quad (2.9b)$$

2.5.1 Parallel polarization

A monochromatic plane wave is said to have parallel polarization if the electric field is parallel to the *plane of incidence*. The plane of incidence is defined by the wavevector \mathbf{k} and the normal vector to the surface \mathbf{n} ; i.e., \mathbf{k} and \mathbf{n} lie in the plane of incidence. From Figure 2.1, we have \mathbf{k} in the xy -plane and $\mathbf{n} = \pm \hat{\mathbf{x}}$, thus, the plane of incidence is the xy -plane.

Consider a parallel polarized incident plane wave of angular frequency ω propagating in the *positive* x -direction. Maxwell's equations (2.1) are linear PDEs, thus, the total wave inside each region may be decomposed into reflected and transmitted waves with the following wavevectors:

$$\mathbf{k}_\ell^\pm = \pm k_{x,\ell} \hat{\mathbf{x}} + k_{y,\ell} \hat{\mathbf{y}}, \quad (2.10)$$

where $k_{x,\ell}$ is given by (2.8), $k_{y,\ell}$ is given by (2.7), $+$ indicates a transmitted wave propagating in the $+x$ -direction, and $-$ indicates a reflected wave propagating in the $-x$ -direction; notice that there is no reflected wave in the 0th region, see Figure 2.1. The magnetic intensity in each region is given by

$$\mathbf{H}_\ell^\pm(\mathbf{r}, t) = \epsilon_\ell \omega E_\ell^\pm \exp [i (\mathbf{k}_\ell^\pm \cdot \mathbf{r} - \omega t)] \hat{\mathbf{z}}, \quad (2.11)$$

where E_ℓ^+ is the *complex* amplitude associated with the transmitted wave, E_ℓ^- is the *complex* amplitude associated with the reflected wave, and $E_{\ell=0}^- \equiv 0$. Substituting (2.11) into (2.9a) yields

$$\mathbf{E}_\ell^\pm(\mathbf{r}, t) = E_\ell^\pm \exp [i (\mathbf{k}_\ell^\pm \cdot \mathbf{r} - \omega t)] [-k_{y,\ell} \hat{\mathbf{x}} \pm k_{x,\ell} \hat{\mathbf{y}}]. \quad (2.12)$$

From (2.2b), we see that the y -component of the total electric field and the total magnetic intensity are continuous across the interface. It is convenient to define a new symbol for the y -component of the electric field evaluated on the interface. Let

$$\chi_\ell^\pm = \pm k_{x,\ell} E_\ell^\pm \exp \left[\pm i k_{x,\ell} \sum_{s=\ell+1}^p h_s \right], \quad (2.13)$$

where h_ℓ is the thickness of the ℓ th region and, for convenience, we set $h_{\ell=0} = h_{\ell=p} \equiv 0$. In (2.13), $\chi_{\ell=0,\dots,p-1}^\pm$ denotes the y -component of the electric field at the interface between regions ℓ and $\ell + 1$ (the interface is approached from the ℓ th region), and $\chi_{\ell=p}^\pm$ denotes the y -component of the electric field at the interface between regions p and $p - 1$ (the interface is approached from region p), see Figure 2.1. Substituting (2.11) and (2.12) into (2.2b), and using (2.13) to simplify the result, yields

$$e^{+ik_{x,\ell+1}h_{\ell+1}}\chi_{\ell+1}^+ + e^{-ik_{x,\ell+1}h_{\ell+1}}\chi_{\ell+1}^- = \chi_\ell^+ + \chi_\ell^-, \quad (2.14a)$$

$$w_{\ell+1} (e^{+ik_{x,\ell+1}h_{\ell+1}}\chi_{\ell+1}^+ - e^{-ik_{x,\ell+1}h_{\ell+1}}\chi_{\ell+1}^-) = w_\ell (\chi_\ell^+ - \chi_\ell^-), \quad (2.14b)$$

for $\ell = 0, \dots, p - 1$, where

$$w_\ell = \frac{\epsilon_\ell \omega}{k_{x,\ell}}, \quad \ell = 0, \dots, p. \quad (2.15)$$

After we obtain a linear system for the perpendicular polarization case, we will solve the linear system given by (2.14), see Section 2.6.

2.5.2 Perpendicular polarization

A monochromatic plane wave is said to have perpendicular polarization if the electric field is perpendicular to the *plane of incidence*. The electric field in each region is given by

$$\mathbf{E}_\ell^\pm(\mathbf{r}, t) = E_\ell^\pm \exp [i (\mathbf{k}_\ell^\pm \cdot \mathbf{r} - \omega t)] \hat{\mathbf{z}}, \quad (2.16)$$

where \mathbf{k}_ℓ^\pm is given by (2.10), and the $^\pm$ superscripts have the same meaning as in Section 2.5.1. Also as in Section 2.5.1, we set $E_{\ell=0}^- \equiv 0$ because there is no reflected wave in the 0th region.

Substituting (2.16) into (2.9b) yields

$$\mathbf{H}_\ell^\pm(\mathbf{r}, t) = \frac{E_\ell^\pm}{\mu_\ell \omega} \exp [i (\mathbf{k}_\ell^\pm \cdot \mathbf{r} - \omega t)] [k_{y,\ell} \hat{\mathbf{x}} \mp k_{x,\ell} \hat{\mathbf{y}}]. \quad (2.17)$$

From (2.2b), we see that both the total electric field and the y -component of the total magnetic intensity are continuous across the interface. Let the electric field evaluated on the interface be denoted by

$$\chi_\ell^\pm = E_\ell^\pm \exp \left[\pm i k_{x,\ell} \sum_{s=\ell+1}^p h_s \right], \quad (2.18)$$

where $\chi_{\ell=0,\dots,p-1}^\pm$ denotes the z -component of the electric field at the interface between regions ℓ and $\ell+1$ (the interface is approached from the ℓ th region) and $\chi_{\ell=p}^\pm$ denotes the z -component of the electric field at the interface between regions p and $p-1$ (the interface is approached from region p). Substituting (2.16) and (2.17) into (2.2b), and using (2.18) to simplify the result, yields (2.14), where

$$w_\ell = -\frac{k_{x,\ell}}{\mu_\ell \omega}, \quad \ell = 0, \dots, p. \quad (2.19)$$

Notice that the linear system for the perpendicular polarization case is the same as the linear system for the parallel polarization case, but the definitions of χ_ℓ^\pm and w_ℓ are different.

2.6 Linear system

The traditional approach to solving the linear system given by (2.14) is to rewrite it as

$$\begin{bmatrix} \chi_{\ell+1}^+ \\ \chi_{\ell+1}^- \end{bmatrix} = M_\ell \begin{bmatrix} \chi_\ell^+ \\ \chi_\ell^- \end{bmatrix}, \quad \ell = 0, \dots, p-1, \quad (2.20a)$$

where

$$M_\ell = \frac{1}{2w_{\ell+1}} \begin{bmatrix} (w_{\ell+1} + w_\ell) \psi_{\ell+1}^{-1} & (w_{\ell+1} - w_\ell) \psi_{\ell+1}^{-1} \\ (w_{\ell+1} - w_\ell) \psi_{\ell+1} & (w_{\ell+1} + w_\ell) \psi_{\ell+1} \end{bmatrix}, \quad (2.20b)$$

and $\psi_\ell = \exp(ik_{x,\ell} h_\ell)$. To compute χ_0^\pm , we iterate (2.20a) until $\ell = p-1$ to obtain

$$\begin{bmatrix} \chi_p^+ / \chi_0^+ \\ \chi_p^- / \chi_0^+ \end{bmatrix} = M_{p-1} M_{p-2} \cdots M_0 \begin{bmatrix} 1 \\ 0 \end{bmatrix}. \quad (2.21)$$

After computing χ_0^+ from (2.21), we can find χ_ℓ^\pm from (2.20a). The approach outlined above is the standard transfer matrix method, but unfortunately it is numerically unstable because the top half of M_ℓ grows exponentially and the bottom half of M_ℓ decreases exponentially if $\text{Im}[k_{x,\ell}h_\ell] \neq 0$. To avoid the numerical instability, we must reformulate the linear system given by (2.14) in terms of ψ_ℓ or ψ_ℓ^{-1} alone. If $\text{Im}[k_{x,\ell}h_\ell]$ is large, then ψ_ℓ may cause underflow errors and ψ_ℓ^{-1} may cause overflow errors. Generally speaking, underflow is preferred to overflow because when underflow occurs, the (normal) number is rounded to the nearest subnormal number or to 0.0; thus, it is desirable to reformulate the linear system in terms of ψ_ℓ instead of ψ_ℓ^{-1} (see Section 2.6.1).

2.6.1 S -matrix

In this section, we present a particularly simple version of the S -matrix formulation of (2.14) that avoids numerical instabilities. To derive the S -matrix, we write a scattering matrix (S -matrix) for an “aggregate layer” consisting of $0, \dots, \ell$ layers to obtain

$$\begin{bmatrix} \chi_\ell^- \\ \chi_0^+ \end{bmatrix} = \begin{bmatrix} s_\ell^{(1,1)} & s_\ell^{(1,2)} \\ s_\ell^{(2,1)} & s_\ell^{(2,2)} \end{bmatrix} \begin{bmatrix} 0 \\ \chi_\ell^+ \end{bmatrix}. \quad (2.22)$$

Using (2.20) to eliminate χ_ℓ^\pm from (2.22) and comparing the result to (2.22) with $\ell \rightarrow \ell + 1$ yields

$$s_{\ell+1}^{(1,2)} = \frac{w_{\ell+1} - w_\ell \left[1 - s_\ell^{(1,2)}\right] \left[1 + s_\ell^{(1,2)}\right]^{-1}}{w_{\ell+1} + w_\ell \left[1 - s_\ell^{(1,2)}\right] \left[1 + s_\ell^{(1,2)}\right]^{-1}} \psi_{\ell+1}^2, \quad (2.23a)$$

$$s_{\ell+1}^{(2,2)} = \frac{2w_{\ell+1}s_\ell^{(2,2)}}{w_{\ell+1} \left[1 + s_\ell^{(1,2)}\right] + w_\ell \left[1 - s_\ell^{(1,2)}\right]} \psi_{\ell+1}, \quad (2.23b)$$

for $\ell = 0, \dots, p-1$, where $s_0^{(1,2)} = 0$ and $s_0^{(2,2)} = 1$. Substituting $\ell = p$ into (2.22) yields $\chi_0^+/\chi_p^+ = s_p^{(2,2)}$, where $s_p^{(2,2)}$ is computed recursively from (2.23b). Using (2.20) to compute χ_ℓ^\pm would make the algorithm numerically unstable. To avoid introducing numerical instability

in the computation of χ_ℓ^\pm , we eliminate χ_0^+ and $\chi_{\ell+1}^-$ from (2.20) and (2.22) to obtain

$$\chi_\ell^+ = \frac{2w_{\ell+1}\psi_{\ell+1}}{w_{\ell+1}\left[1 + s_\ell^{(1,2)}\right] + w_\ell\left[1 - s_\ell^{(1,2)}\right]}\chi_{\ell+1}^+, \quad (2.24a)$$

for $\ell = p-1, \dots, 0$ and

$$\chi_\ell^- = s_\ell^{(1,2)}\chi_\ell^+, \quad \ell = p, \dots, 1. \quad (2.24b)$$

Notice that χ_ℓ^\pm only depends on $s_\ell^{(1,2)}$. The S -matrix algorithm is numerically stable because (2.23a) and (2.24) only depend on ψ_ℓ .

Originally, (2.23a) and (2.24) were derived in [16] by citing the general scattering-theory paradigm that requires existence of a linear relationship between χ_ℓ^- and χ_ℓ^+ , i.e., $\chi_\ell^- = s_\ell^{(1,2)}\chi_\ell^+$, and then substituting it directly into (2.20) to obtain (2.23a) and (2.24a). Arguably our derivation is just as simple as in [16] but follows the traditional S -matrix formulation [15, 17] more closely.

We would like to note that it is possible to formulate an S -matrix algorithm where χ_ℓ^\pm are computed directly from χ_p^+ [18, 19], but such a formulation requires recursive computation of *three* elements of an S -matrix rather than just *one* element in our formulation. Moreover, it is also possible to obtain formulas that directly relate χ_ℓ^\pm to χ_p^+ from our formulation by simply multiplying out (2.24), i.e., $\chi_\ell^+ = \tilde{s}_{\ell+1}^{(2,2)}\tilde{s}_{\ell+2}^{(2,2)}\dots\tilde{s}_p^{(2,2)}\chi_p^+$ and $\chi_\ell^- = s_\ell^{(1,2)}\left(\tilde{s}_{\ell+1}^{(2,2)}\tilde{s}_{\ell+2}^{(2,2)}\dots\tilde{s}_p^{(2,2)}\right)\chi_p^+$, where $\tilde{s}_{\ell+1}^{(2,2)} = s_{\ell+1}^{(2,2)}/s_\ell^{(2,2)}$.

2.7 Conserved quantities

In the case of the RHM, the time-averaged complex Poynting theorem for harmonic fields is given by

$$\nabla \cdot \mathbf{S} + Q^{(e)} + Q^{(m)} + 2i\omega(u^{(e)} - u^{(m)}) = 0, \quad (2.25a)$$

where $\mathbf{S} = \frac{1}{2}\mathbf{E} \times \mathbf{H}^*$ is the complex Poynting vector and

$$u^{(e)} = \frac{\epsilon'}{4} \mathbf{E} \cdot \mathbf{E}^* = \frac{\epsilon'}{4} \|\mathbf{E}\|^2, \quad (2.25b)$$

$$u^{(m)} = \frac{\mu'}{4} \mathbf{H} \cdot \mathbf{H}^* = \frac{\mu'}{4} \|\mathbf{H}\|^2, \quad (2.25c)$$

$$Q^{(e)} = \frac{\omega \epsilon''}{2} \mathbf{E} \cdot \mathbf{E}^* = \frac{\omega \epsilon''}{2} \|\mathbf{E}\|^2, \quad (2.25d)$$

$$Q^{(m)} = \frac{\omega \mu''}{2} \mathbf{H} \cdot \mathbf{H}^* = \frac{\omega \mu''}{2} \|\mathbf{H}\|^2. \quad (2.25e)$$

In (2.25), $u^{(e)}$ is the *real* time-averaged electric density, $u^{(m)}$ is the *real* time-averaged magnetic density, $Q^{(e)}$ and $Q^{(m)}$ represent time-averaged electric and magnetic losses, respectively (e.g., Joule heating [37, Sec. 2.19, Sec. 2.20]). Substituting the total electric field and the total magnetic intensity into (2.25b) and (2.25c), respectively, yields

$$u_\ell^{(e)} = \frac{\epsilon'_\ell}{4} \left(\|\mathbf{E}_\ell^+\|^2 + \|\mathbf{E}_\ell^-\|^2 + 2\text{Re} [\mathbf{E}_\ell^+ \cdot \mathbf{E}_\ell^{-*}] \right), \quad (2.26a)$$

$$u_\ell^{(m)} = \frac{\mu'_\ell}{4} \left(\|\mathbf{H}_\ell^+\|^2 + \|\mathbf{H}_\ell^-\|^2 + 2\text{Re} [\mathbf{H}_\ell^+ \cdot \mathbf{H}_\ell^{-*}] \right), \quad (2.26b)$$

where Re denotes the real part.

In the case of the LHM, the complex Poynting theorem for harmonic fields given by (2.25) is *mathematically* correct. However, the identification of the real electric density (2.25b) and the real magnetic density (2.25c) is troublesome because both are *negative*. It was pointed out by Veselago [20] that the LHM must be accompanied by frequency dispersion, in which case the real electric density and the real magnetic density are not given by (2.25b) and (2.25c), respectively. Moreover, simultaneously negative permittivity and permeability occur very near resonance and there is therefore no frequency interval for the LHM where permittivity and permeability may be reasonably approximated by a constant. For a more detailed discussion see [23, 38, 39].

Another conserved quantity is the *fundamental invariant in multilayers* (FIM) [40, 41], given by

$$w_{\ell+1} \left[(\psi_{\ell+1} \chi_{\ell+1}^+)^2 - (\psi_{\ell+1}^{-1} \chi_{\ell+1}^-)^2 \right] = w_\ell \left[(\chi_\ell^+)^2 - (\chi_\ell^-)^2 \right], \quad (2.27)$$

for $\ell = 0, \dots, p-1$. The FIM is a product of the continuity conditions for the electric field (2.14a) and magnetic intensity (2.14b). However, the FIM is *not* an energy conservation statement because it contains $(\chi_\ell^\pm)^2$ and $(\chi_{\ell+1}^\pm)^2$ instead of $|\chi_\ell^\pm|^2$ and $|\chi_{\ell+1}^\pm|^2$. In our view, the FIM is particularly interesting because its structure is similar to that of the space-time interval of special relativity, $ds^2 = dx^2 - c^2 dt^2$, where c is the speed of light. Moreover, it has been pointed out in [42] that many results associated with wave propagation through planar stratified media are more easily derived through an analogy with special relativity. In this paper, we don't pursue the analogy between wave propagation through a multilayer stack and the theory of special relativity any further, but we do want to stress that this analogy is not a mere coincidence.

2.7.1 Energy densities for parallel polarization

It is convenient to introduce a new symbol for the transverse component (the y -component) of the electric field as a function of distance, x , into the multilayer stack. For $\ell = 0, \dots, p$, let

$$\Gamma_\ell^\pm(x) = \pm k_{x,\ell} E_\ell^\pm \exp[\pm i k_{x,\ell} x] \quad (2.28)$$

then,

$$\begin{aligned} |\Gamma_\ell^\pm(x)|^2 &= |k_{x,\ell}|^2 |E_\ell^\pm|^2 \exp(\mp 2\text{Im}[k_{x,\ell}]x), \\ \text{Re}[\Gamma_\ell^+(x)\Gamma_\ell^{-*}(x)] &= -|k_{x,\ell}|^2 \text{Re}[E_\ell^+ E_\ell^{-*} e^{+2i\text{Re}[k_{x,\ell}]x}]. \end{aligned} \quad (2.29)$$

Substituting (2.12) into (2.26a) and using (2.29) to simplify the result yields

$$\begin{aligned} u_\ell^{(e)}(x) &= \frac{\epsilon'_\ell}{4} \left[\left(1 + \frac{k_{y,p}^2}{|k_{x,\ell}|^2} \right) (|\Gamma_\ell^+(x)|^2 + |\Gamma_\ell^-(x)|^2) \right. \\ &\quad \left. + 2 \left(1 - \frac{k_{y,p}^2}{|k_{x,\ell}|^2} \right) \text{Re}[\Gamma_\ell^+(x)\Gamma_\ell^{-*}(x)] \right]. \end{aligned} \quad (2.30)$$

Substituting (2.11) into (2.26b) and using (2.29) to simplify the result yields

$$u_\ell^{(m)}(x) = \frac{\mu'_\ell |w_\ell|^2}{4} \left(|\Gamma_\ell^+(x)|^2 + |\Gamma_\ell^-(x)|^2 - 2\text{Re}[\Gamma_\ell^+(x)\Gamma_\ell^{-*}(x)] \right), \quad (2.31)$$

where w_ℓ is given by (2.15).

2.7.2 Energy densities for perpendicular polarization

Again, it is convenient to introduce a new symbol for the transverse component (the z -component) of the electric field as a function of distance, x , into the multilayer stack. For $\ell = 0, \dots, p$, let

$$\Gamma_\ell^\pm(x) = E_\ell^\pm \exp[\pm i k_{x,\ell} x] \quad (2.32)$$

then,

$$\begin{aligned} |\Gamma_\ell^\pm(x)|^2 &= |E_\ell^\pm|^2 \exp(\mp 2 \operatorname{Im}[k_{x,\ell}] x), \\ \operatorname{Re} [\Gamma_\ell^+(x) \Gamma_\ell^{-*}(x)] &= \operatorname{Re} [E_\ell^+ E_\ell^{-*} e^{+2i \operatorname{Re}[k_{x,\ell}] x}]. \end{aligned} \quad (2.33)$$

Substituting (2.16) into (2.26a) and using (2.33) to simplify the result yields

$$u_\ell^{(e)}(x) = \frac{\epsilon'_\ell}{4} \left[|\Gamma_\ell^+(x)|^2 + |\Gamma_\ell^-(x)|^2 + 2 \operatorname{Re} [\Gamma_\ell^+(x) \Gamma_\ell^{-*}(x)] \right]. \quad (2.34)$$

Substituting (2.17) into (2.26b) and using (2.33) to simplify the result yields

$$\begin{aligned} u_\ell^{(m)}(x) &= \frac{\mu'_\ell |w_\ell|^2}{4} \left[\left(1 + \frac{k_{y,p}^2}{|k_{x,\ell}|^2} \right) (|\Gamma_\ell^+(x)|^2 + |\Gamma_\ell^-(x)|^2) \right. \\ &\quad \left. - 2 \left(1 - \frac{k_{y,p}^2}{|k_{x,\ell}|^2} \right) \operatorname{Re} [\Gamma_\ell^+(x) \Gamma_\ell^{-*}(x)] \right], \end{aligned} \quad (2.35)$$

where w_ℓ is given by (2.19).

2.8 Transmission and reflection coefficients

The transmission coefficient, T , and the reflection coefficient, R , are given by

$$T = \frac{\operatorname{Re}[\mathbf{S}_0^+] \cdot \hat{\mathbf{x}}}{\operatorname{Re}[\mathbf{S}_p^+] \cdot \hat{\mathbf{x}}}, \quad (2.36a)$$

$$R = -\frac{\operatorname{Re}[\mathbf{S}_p^-] \cdot \hat{\mathbf{x}}}{\operatorname{Re}[\mathbf{S}_p^+] \cdot \hat{\mathbf{x}}}, \quad (2.36b)$$

with

$$\mathbf{S}_0^+ = \frac{1}{2} \mathbf{E}_0^+ \times \mathbf{H}_0^{+*} \quad \text{and} \quad \mathbf{S}_p^\pm = \frac{1}{2} \mathbf{E}_p^\pm \times \mathbf{H}_p^{\pm*},$$

where it is understood that \mathbf{E}_p^\pm and $\mathbf{H}_p^{\pm*}$ are evaluated at the interface between regions p and $p-1$ (the interface is approached from region p), and \mathbf{E}_0^+ and \mathbf{H}_0^{+*} are evaluated at the interface between regions 1 and 0 (the interface is approached from the 0th region).

In the case of the parallel polarization state, substituting (2.11) and (2.12) into (2.36), and using (2.13) to simplify the result, yields

$$T = \frac{k_{x,p}}{\epsilon_p} \frac{\text{Re}[\epsilon_0^* k_{x,0}]}{|k_{x,0}|^2} \left| \frac{\chi_0^+}{\chi_p^+} \right|^2, \quad (2.37a)$$

$$R = \left| \frac{\chi_p^-}{\chi_p^+} \right|^2. \quad (2.37b)$$

In the case of the perpendicular polarization state, substituting (2.17) and (2.16) into (2.36), and using (2.18) to simplify the result, yields

$$T = \frac{\mu_p}{k_{x,p}} \text{Re} \left[\frac{k_{x,0}^*}{\mu_0^*} \right] \left| \frac{\chi_0^+}{\chi_p^+} \right|^2, \quad (2.38a)$$

$$R = \left| \frac{\chi_p^-}{\chi_p^+} \right|^2. \quad (2.38b)$$

The transmission and reflection coefficients, given by (2.37) for the parallel polarization state and by (2.38) for the perpendicular polarization state, are valid for both a right- and a left-handed material.

2.9 Multilayer classes

Python is a multi-paradigm programming language that supports object-oriented programming, structured programming, and a subset of functional and aspect-oriented programming styles. There is a large number of numerical libraries available for use with Python. We chose to use a numerical library called SciPy [43] for numerical computations because, in our opinion, a reader familiar with MATLABTM and/or Fortran 90/95 will find SciPy a very natural and

easy-to-use library.

In order for our multilayer classes, namely **Boundary** and **Layer**, which are collectively called **openTMM**,⁵ to be as useful as possible to the scientific community, we paid particular attention to the readability, usability, and maintainability of the code. Both classes are implemented in an object-oriented programming style as described below.

The **Boundary** class is meant to be a base class (*superclass* in the Python lexicon) that will be inherited by the derived classes (*subclasses* in the Python lexicon). The derived classes perform “high-level” computations such as computing the energy density and the transmission and reflection coefficients. The derived **Layer** class inherits the **Boundary** and computes the quantities described in Table 2.1. The benefit of using inheritance in our multilayer calculations is that other developers may extend the **Layer** class or write their own derived class to compute the desired quantity of interest without having to implement the low-level code, e.g., the code for computing $k_{x,\ell}$ and the S -matrix. The **Boundary** superclass

Table 2.1: The first column contains the name (as it appears in the code) of the object attribute (method) of the class **Layer**, the second column contains a description of the method, and the third column contains references to the section where a more detailed description may be found.

Name	Description	Refs.
field	Transverse component of the electric field as a function of distance, $\Gamma^\pm(x)$	2.7.1 2.7.2
energy	Electric/magnetic energy density as a function of distance, $u^{(e,m)}(x)$	2.7.1 2.7.2
loss	Electric/magnetic losses as a function of distance, $Q^{(e,m)}(x)$	2.7
divPoynting	Divergence of the Poynting vector as a function of distance, $\nabla \cdot \mathbf{S}(x)$	2.7
FIM	FIM at each boundary interface	2.7
FIMvsDist	FIM as a function of distance	2.7
TRvsFreq TRvsAngle TRvsFreqAndAngle	Transmission and reflection coefficients as a function of frequency $f = \omega/2\pi$ and/or angle of incidence ϕ , i.e., $\{T(f), R(f)\}$, $\{T(\phi), R(\phi)\}$, $\{T(f, \phi), R(f, \phi)\}$	2.8

⁵**openTMM** is an open-source software distributed under the MIT license and is available from <http://pypi.python.org/pypi/openTMM>.

computes a “minimal” set of “basic” quantities, see Table 2.2, that are used by the `Layer` subclass. Each function/method in the `Boundary` and `Layer` class contains a documentation header (*docstring* in the Python lexicon), which describes the function/method in detail and includes an example of its use. To access the docstrings, the user may use Python’s `help` function or if more user friendly formatting is desired, the user may use SciPy’s `info` function. For example, the docstring for `Layer.energy` function may be accessed via

```
>>> help(openTMM.Layer.energy)
>>> scipy.info(openTMM.Layer.energy)
```

and all docstings contained in a class may be accessed via

```
>>> help(openTMM.ClassName)
>>> scipy.info(openTMM.ClassName)
```

where `ClassName` is either `Boundary` or `Layer`. This interactive documentation feature of Python makes it a very convenient language to use and largely eliminates the need to produce separate code documentation. The `help/scipy.info` functions are similar to the *Manual*

Table 2.2: The first column contains the name (as it appears in the code) of the object attribute of the class `Boundary`, the second column contains a description of the attribute, and the third column contains references to a section and/or equation where a more detailed description of the attribute may be found.

Name	Description	Refs.
<code>self.h</code>	Thickness of each layer, h_ℓ	(2.13), (2.18)
<code>self.epsRel</code>	Relative permittivity of each region, $\epsilon_\ell/\epsilon_{\text{vacuum}}$	Section 2.4
<code>self.muRel</code>	Relative permeability of each region, $\mu_\ell/\mu_{\text{vacuum}}$	Section 2.4
<code>self.pol</code>	Polarization state	Section 2.5
<code>self.kx</code>	x -component of the wavevector, $k_{x,\ell}$	(2.8)
<code>self.w</code>	Scaled <code>self.kx</code> (polarization dependent), w_ℓ	(2.15), (2.19)
<code>self.chiPlus</code>	Transverse component of the electric field evaluated on the interface, χ_ℓ^+/χ_p^+	(2.13), (2.18)
<code>self.chiMinus</code>	Transverse component of the electric field evaluated on the interface, χ_ℓ^-/χ_p^+	(2.13), (2.18)

pager utils (man pages) of Unix-like operating systems; could one imagine using a Linux shell without `man python`?

2.10 Python and numerical efficiency

There is some concern about the speed of computations in Python because it is *byte-compiled*, not a compiled language such as Fortran 90/95 or C/C++. However, in our opinion, the code readability (less error-prone syntax), flexibility (effortless integration with other software) and ease-of-use of Python (leading to shorter development times) in many cases outweigh any performance benefits of compiled languages. An interested reader may consult [44–47] for a fuller discussion of why Python is a language of choice for scientific software development. Typically, computationally intensive routines in Python are implemented in compiled languages and therefore, the difference in computation time between Python and compiled languages is acceptable for many applications [45–48]. In the Python lexicon, the mixing of programming languages is called the *Pythonic approach*; this is the approach we use with the computationally intensive part of the **Boundary** superclass.

It is relatively obvious that the computationally intensive part of the **Boundary** superclass is the computation of χ_ℓ^\pm , i.e., the solution of the linear system described in Section 2.6. Therefore, the computation of χ_ℓ^\pm is implemented in Fortran 90 and the Python bindings are built by F2PY [49] (F2PY is now part of SciPy). However, implementing “workhorse functions” in a compiled language reduces the readability and maintainability of code to some extent. Therefore, we strongly encourage developers to only implement workhorse functions in compiled languages when they lead to severe bottlenecks. It is often the case that bottlenecks can only be identified after code profiling (performance analysis). For example, it is not obvious that the square root function in the computation of $k_{x,\ell}$ is relatively time-consuming. The computation of $k_{x,\ell}$ is relatively expensive because SciPy’s square root function, `scipy.sqrt`, does an element-by-element analysis of the input array to find if it contains any real elements less than zero. If a real, less-than-zero element is found, SciPy converts the whole input array to a complex data type and passes it to NumPy [50], which

uses an efficient C code to compute the square root. In our case, SciPy’s time-consuming element-by-element analysis is unnecessary because of a priori knowledge about $k_{x,\ell}$, see Section 2.4. We could avoid `scipy.sqrt` by directly using NumPy’s square root function, but this is not the most convenient approach because NumPy’s square root function of a complex number $z = |z|e^{i\theta}$ returns $\sqrt{|z|}e^{i\theta/2}$, where $-\pi < \theta \leq \pi$, but (2.8) requires that $\text{Im}[k_{x,\ell}] > 0$. To avoid this inconvenience, we choose to implement our own square root subroutine, `cmplx_sqrt`, which returns the square root in an appropriate quadrant as required by (2.8). The `cmplx_sqrt` is implemented in Fortran 90 with Python binding build by F2PY and depends on Fortran’s intrinsic square root function, `SQRT`.

To confirm that the run-time of the Python `Boundary` superclass is acceptable, we compared it to a `Boundary` class implemented in pure Fortran 90. From Figure 2.2, we see that for a large number of layers ($\gtrsim 300$) the Python code is only 25 percent slower than the pure Fortran 90 code. However, for a small number of layers ($\lesssim 20$) the Python code is about 10 times slower than the pure Fortran 90 code, see inset in Figure 2.2, but this is not major concern because such a small number of layers has an absolute execution time about a second or so in Python. We believe that the run-time discrepancy between a small and a large number of layers is caused by SciPy’s overhead cost, which does not increase significantly as a function of array size.

2.11 Numerical stability and accuracy

To demonstrate the numerical stability and accuracy of `openTMM`, we numerically checked the complex Poynting theorem given by (2.25a), the fundamental invariant in multilayers given by (2.27), and the de Hoop reciprocity theorem [51, Section 6]. The de Hoop reciprocity theorem states that if $\epsilon_0 = \epsilon_p$ and $\mu_0 = \mu_p$, then the transmitted wave is unaffected by a 180 degree rotation of the multilayer stack around the z -axis, see Figure 2.1. We measure the accuracy of a computed quantity in terms of the number of significant digits it agrees with the theoretical value and we denote this measure of accuracy by δ_v . Approximately, δ_v

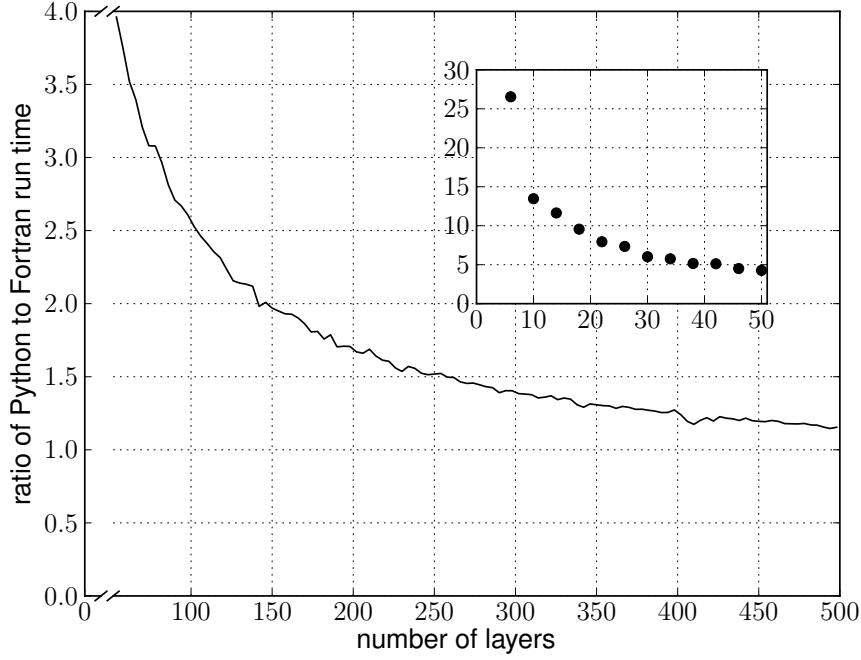


Figure 2.2: The ratio of total computational time required to compute $T(f_i, \phi_j)$ and $R(f_i, \phi_j)$, where $1 \leq \{i, j\} \leq 10^3$, using `openTMM` and a pure Fortran 90 code. Each multilayer stack is composed of the same number of pseudorandom layers of the following types: right-handed layers with/without absorption and left-handed layers with/without absorption.

is given by

$$\delta_{\tilde{v}} \approx \min \left\{ -\log \left| \frac{v - \tilde{v}_{\text{Re}}}{v} \right|, -\log \left| \frac{v - \tilde{v}_{\text{Im}}}{v} \right| \right\} \quad (2.39)$$

where v is the theoretical value and $\{\tilde{v}_{\text{Re}}, \tilde{v}_{\text{Im}}\}$ are the numerically computed value. For a numerical check of the complex Poynting theorem \tilde{v}_{Re} is given as $-\text{Re}[\nabla \cdot \mathbf{S}] / [Q^{(\text{e})} + Q^{(\text{m})}]$ and \tilde{v}_{Im} is given as $-\text{Im}[\nabla \cdot \mathbf{S}] / [2\omega(u^{(\text{e})} - u^{(\text{m})})]$. For the FIM test, \tilde{v}_{Re} (\tilde{v}_{Im}) is the ratio of the the real (imaginary) part of the left-hand side to the real (imaginary) part of the right-hand side of (2.27). For the de Hoop reciprocity test, $\tilde{v}_{\text{Re}} = \text{Re}[\chi_0^+] / \text{Re}[\chi_p^+]$ and $\tilde{v}_{\text{Im}} = \text{Im}[\chi_0^+] / \text{Im}[\chi_p^+]$, where χ_0^+ is the transmitted wave before the 180 degree rotation of the multilayer stack and χ_p^+ is the transmitted wave after the rotation. For all three numerical checks, $v = 1$ and all computations are performed in double-precision (≈ 16 significant digits). From Figure 2.3, we see that the three numerical checks are satisfied with an accuracy of $\delta_{\tilde{v}} \geq 12$. Despite the fact that some of the layers in the stack chosen for

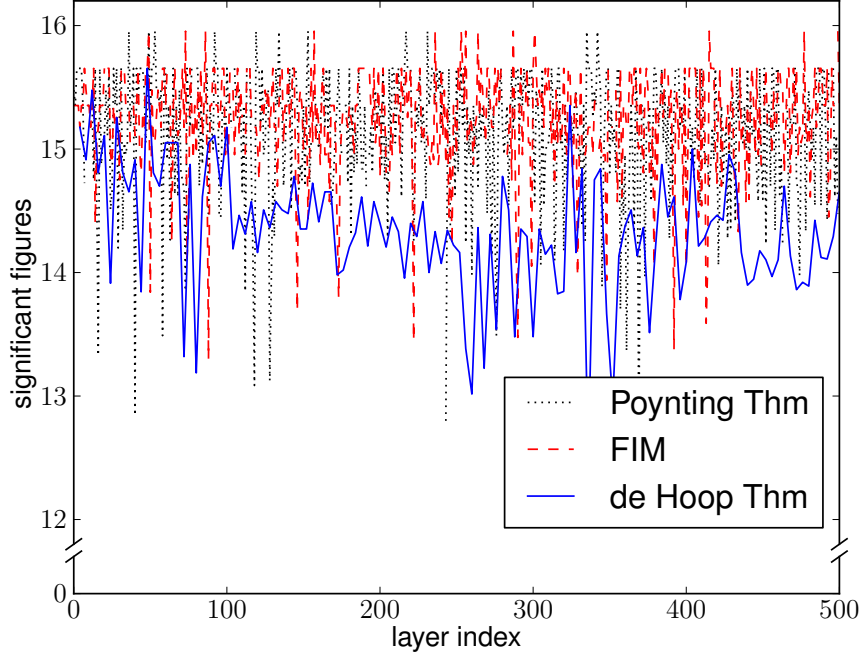


Figure 2.3: $\delta_{\bar{v}}$ is shown for a multilayer stack composed of the same number of pseudorandom layers of the following types: right-handed layers with/without absorption and left-handed layers with/without absorption.

Figure 2.3 have very high absorption, $\text{Im}[k_{x,\ell}h_\ell] \approx 30$, we see that $\delta_{\bar{v}}$ does not decrease as a function of distance into the stack, which confirms that our S -matrix algorithm is indeed numerically stable. The composition of the multilayer stack is summarized in Table 2.3. To produce Figure 2.3, we used a normally incident plane wave of frequency 100 GHz and the first pathological case scheme, see Section 2.4.2.

2.12 Conclusions

A numerically stable S -matrix algorithm for electromagnetic wave propagation through planar stratified media composed of a right-handed and/or left-handed material has been implemented in Python. Pathological cases caused by an unphysical approximation of zero absorption have been carefully examined and numerically circumvented (see Section 2.4.2). The numerical computations were implemented in an object-oriented programming style by dividing them into two classes, **Boundary** and **Layer**. The **Boundary** class performs com-

Table 2.3: The height, h , relative permittivity, ϵ_{rel} , and the relative permeability, μ_{rel} , of each layer were pseudorandomly chosen from the intervals shown in the table. E.G., from the second line of the table, we see that 125 layers have thickness between 1 mm and 10 mm, and relative permittivity/permeability between -10 and -1 . A 500-layer stack was used for the Poynting theorem and the FIM test. For the de Hoop reciprocity theorem test, a multilayer stack consisting of 5, 9, 13, \dots , 501 layers was used.

Test	# of layers	h (mm)	ϵ'_{rel}	ϵ''_{rel}	μ'_{rel}	μ''_{rel}
Poynting Thm & FIM	125	[1, 10]	[1, 10]	0	[1, 10]	0
	125	[1, 10]	$[-10, -1]$	0	$[-10, -1]$	0
	125	[1, 10]	$[-10, -1]$	[0.01, 0.1]	$[-10, -1]$	0
	115	[1, 10]	[1, 10]	0	[1, 10]	[0.01, 0.1]
	10	[10, 15]	[2, 10]	[0, 2]	[1, 10]	0
de Hoop Thm	$\{1, \dots, 125\}$	[1, 10]	[1, 10]	0	[1, 10]	0
	$\{1, \dots, 125\}$	[1, 10]	$[-10, -1]$	0	$[-10, -1]$	0
	$\{1, \dots, 125\}$	[1, 10]	$[-10, -1]$	[0.01, 0.1]	$[-10, -1]$	0
	$\{1, \dots, 125\}$	[1, 10]	[1, 10]	0	[1, 10]	[0.01, 0.1]
	1	[1, 10]	[2, 10]	[0, 1]	[1, 10]	0

putationally intensive calculations, namely the solution of the linear system described in Section 2.6.1 and the square root of $k_{x,\ell}^2$. The workhorse functions of the **Boundary** class were implemented in Fortran 90 in order to avoid computational bottlenecks. The **Layer** class performs high-level calculations, such as calculation of $u^{(\text{e,m})}(x)$, $Q^{(\text{e,m})}(x)$, $\Gamma^\pm(x)$, and FIM. The code has been tested and is accurate to ≈ 12 significant digits (see Section 2.11).

We hope that our open-source and object-oriented implementation of the S -matrix algorithm, which is suitable for modern applications such as Anderson localization of light and perfect lensing, will be adopted by a wide scientific community. At the very least, we hope that our publicly available implementation of the S -matrix algorithm will encourage the scientific community to use open-source software, thus increasing the reproducibility of scientific work.

2.13 Acknowledgment

This work was partially supported by the U.S. Department of Energy under Grant DE-FG02-09ER16018. Also, this material is based upon work supported in part by the U.S. Of-

Office of Naval Research as a Multi-disciplinary University Research Initiative on Sound and Electromagnetic Interacting Waves under Grant No. N00014-10-1-0958.

2.14 References Cited

- [1] L. M. Brekhovskikh, *Waves in Layered Media*, Academic Press, New York, 1960. Translated from Russian by David Lieberman.
- [2] J. R. Wait, *Electromagnetic Waves in Stratified Media*, IEEE Press, New York, 1996.
- [3] J. M. Vigoureux, Polynomial formulation of reflection and transmission by stratified planar structures, *J. Opt. Soc. Am. A* 8 (1991) 1697–1701.
- [4] T. El-Agez, S. Taya, A. El Tayyan, A polynomial approach for reflection, transmission, and ellipsometric parameters by isotropic stratified media, *Optica Applicata* 40 (2010) 501–510.
- [5] J. M. Vigoureux, Use of Einstein’s addition law in studies of reflection by stratified planar structures, *J. Opt. Soc. Am. A* 9 (1992) 1313–1319.
- [6] J. J. Monzón, L. L. Sánchez-Soto, Fully relativisticlike formulation of multilayer optics, *J. Opt. Soc. Am. A* 16 (1999) 2013–2018.
- [7] P. Grossel, J. M. Vigoureux, F. Baïda, Nonlocal approach to scattering in a one-dimensional problem, *Phys. Rev. A* 50 (1994) 3627–3637.
- [8] R. L. Mooney, An exact theoretical treatment of reflection-reducing optical coatings, *J. Opt. Soc. Am.* 35 (1945) 574–583.
- [9] W. Weinstein, The reflectivity and transmissivity of multiple thin coatings, *J. Opt. Soc. Am.* 37 (1947) 576–577.
- [10] F. Abelès, La théorie générale des couches minces, *J. Phys. Radium* 11 (1950) 307–310.
- [11] M. Born, E. Wolf, *Principles of Optics: Electromagnetic Theory of Propagation, Interference and Diffraction of Light*, Pergamon Press, Oxford, sixth (corrected) edition, 1986.
- [12] E. L. Tan, Enhanced R -matrix algorithms for multilayered diffraction gratings, *Appl. Opt.* 45 (2006) 4803–4809.

- [13] F. Montiel, M. Nevière, Differential theory of gratings: extension to deep gratings of arbitrary profile and permittivity through the R -matrix propagation algorithm, *J. Opt. Soc. Am. A* 11 (1994) 3241–3250.
- [14] L. Li, Multilayer modal method for diffraction gratings of arbitrary profile, depth, and permittivity, *J. Opt. Soc. Am. A* 10 (1993) 2581–2591.
- [15] L. Li, Formulation and comparison of two recursive matrix algorithms for modeling layered diffraction gratings, *J. Opt. Soc. Am. A* 13 (1996) 1024–1035.
- [16] M. Auslender, S. Hava, Scattering-matrix propagation algorithm in full-vectorial optics of multilayer grating structures, *Opt. Lett.* 21 (1996) 1765–1767.
- [17] N. P. K. Cotter, T. W. Preist, J. R. Sambles, Scattering-matrix approach to multilayer diffraction, *J. Opt. Soc. Am. A* 12 (1995) 1097–1103.
- [18] D. Yuk Kei Ko, J. R. Sambles, Scattering matrix method for propagation of radiation in stratified media: attenuated total reflection studies of liquid crystals, *J. Opt. Soc. Am. A* 5 (1988) 1863–1866.
- [19] D. Yuk Kei Ko, J. C. Inkson, Matrix method for tunneling in heterostructures: Resonant tunneling in multilayer systems, *Phys. Rev. B* 38 (1988) 9945–9951.
- [20] V. G. Veselago, The electrodynamics of substances with simultaneously negative values of ϵ and μ , *Soviet Physics Uspekhi* 10 (1968) 509–514.
- [21] D. R. Smith, W. J. Padilla, D. C. Vier, S. C. Nemat-Nasser, S. Schultz, Composite medium with simultaneously negative permeability and permittivity, *Phys. Rev. Lett.* 84 (2000) 4184–4187.
- [22] R. A. Shelby, D. R. Smith, S. Schultz, Experimental verification of a negative index of refraction, *Science* 292 (2001) 77–79.
- [23] S. A. Ramakrishna, Physics of negative refractive index materials, *Reports on Progress in Physics* 68 (2005) 449–521.
- [24] J. B. Pendry, Negative refraction makes a perfect lens, *Phys. Rev. Lett.* 85 (2000) 3966–3969.
- [25] M. Scalora, G. D’Aguanno, N. Mattiucci, M. J. Bloemer, D. de Ceglia, M. Centini, A. Mandatori, C. Sibilia, N. Akozbek, M. G. Cappeddu, M. Fowler, J. W. Haus, Negative refraction and sub-wavelength focusing in the visible range using transparent metallo-dielectric stacks, *Opt. Express* 15 (2007) 508–523.

- [26] E. Abrahams (Ed.), 50 Years of Anderson Localization, World Scientific, New Jersey, 2010.
- [27] P. Sheng, Introduction to Wave Scattering, Localization and Mesoscopic Phenomena, Springer, Berlin, second edition, 2006.
- [28] J. A. Scales, L. D. Carr, D. B. McIntosh, V. Freilikher, Y. P. Bliokh, Millimeter wave localization: Slow light and enhanced absorption in random dielectric media, Phys. Rev. B 76 (2007) 085118.
- [29] K. Y. Bliokh, V. D. Freilikher, Localization of transverse waves in randomly layered media at oblique incidence, Phys. Rev. B 70 (2004) 245121.
- [30] A. A. Asatryan, S. A. Gredeskul, L. C. Botten, M. A. Byrne, V. D. Freilikher, I. V. Shadrivov, R. C. McPhedran, Y. S. Kivshar, Anderson localization of classical waves in weakly scattering metamaterials, Phys. Rev. B 81 (2010) 075124.
- [31] R. Giust, J. M. Vigoureux, M. Sarrazin, Asymmetrical properties of the optical reflection response of the Fabry–Pérot interferometer, J. Opt. Soc. Am. A 17 (2000) 142–148.
- [32] S. V. Zhukovsky, Perfect transmission and highly asymmetric light localization in photonic multilayers, Phys. Rev. A 81 (2010) 053808.
- [33] A. Markushevich, Theory of Functions of a Complex Variable, Chelsea Publishing Company, New York, second edition, 1977. 3 volumes in one, translated from Russian by Richard A. Silverman.
- [34] L. D. Landau, E. M. Lifshitz, Statistical Physics: Part 1, volume 5, Pergamon Press, Oxford, third revised and enlarged edition, 1993. Translated from Russian by J. B. Sykes and M. J. Kearsley.
- [35] L. D. Landau, E. M. Lifshitz, P. L. Petrovich, Electrodynamics of Continuous Media, volume 8, Pergamon Press, Oxford, second revised and enlarged edition, 1993. Translated from Russian by J. B. Sykes, J. S. Bell and M. J. Kearsley.
- [36] J. Skaar, On resolving the refractive index and the wave vector, Optics Letters 31 (2006) 3372–3374.
- [37] J. A. Stratton, Electromagnetic Theory, McGraw-Hill, New York, 1941.
- [38] R. Ruppin, Electromagnetic energy density in a dispersive and absorptive material, Physics Letters A 299 (2002) 309–312.

- [39] A. M. Vadim, Correct definition of the Poynting vector in electrically and magnetically polarizable medium reveals that negative refraction is impossible, *Optics Express* 16 (2008) 19152–19168.
- [40] J. M. Vigoureux, P. Grossel, A relativistic-like presentation of optics in stratified planar media, *American Journal of Physics* 61 (1993) 707–712.
- [41] J. M. Vigoureux, R. Giust, New relations in the most general expressions of the transfer matrix, *Optics Communications* 186 (2000) 21–25.
- [42] R. Giust, J. M. Vigoureux, J. Lages, Generalized composition law from 2×2 matrices, *American Journal of Physics* 77 (2009) 1068–1073.
- [43] E. Jones, T. Oliphant, P. Peterson, et al., SciPy: Open source scientific tools for Python, 2001–.
- [44] L. Prechelt, An empirical comparison of seven programming languages, *Computer* 33 (2000) 23–29.
- [45] E. Lambert, M. Fiers, S. Nizamov, M. Tassaert, S. G. .Johnson, P. Bienstman, W. Bogaerts, Python bindings for the open source electromagnetic simulator Meep, *Computing in Science and Engineering* 13 (2011) 53–65.
- [46] O. Bröker, O. Chinellato, R. Geus, Using Python for large scale linear algebra applications, *Future Generation Computer Systems* 21 (2005) 969–979.
- [47] C. Rickett, S.-E. Choi, C. Rasmussen, M. Sottile, Rapid prototyping frameworks for developing scientific applications: A case study, *The Journal of Supercomputing* 36 (2006) 123–134.
- [48] L. Dalcín, R. Paz, M. Storti, MPI for Python, *Journal of Parallel and Distributed Computing* 65 (2005) 1108–1115.
- [49] P. Peterson, F2PY: a tool for connecting Fortran and Python programs, *Int. J. Computational Science and Engineering* 4 (2009) 296–305.
- [50] T. E. Oliphant, *Guide to NumPy*, Provo, UT, 2006.
- [51] R. J. Potton, Reciprocity in optics, *Rep. Prog. Phys.* 67 (2004) 717–754.

CHAPTER 3

LINEAR RESPONSE LAWS AND CAUSALITY IN ELECTRODYNAMICS

A paper published in the *European Journal of Physics*.

Alex J. Yuffa^{*}, John A. Scales

Department of Physics, Colorado School of Mines, Golden, CO 80401, USA

^{*}Primary researcher and author. E-mail: ayuffa@gmail.com

3.1 Abstract

Linear response laws and causality (the effect cannot precede the cause) are of fundamental importance in physics. In the context of classical electrodynamics, students often have a difficult time grasping these concepts because the physics is obscured by the intermingling of the time and frequency domains. In this paper, we analyse the linear response laws and causality in the time and frequency domains with the aim of pedagogical clarity. We will show that it is easy to violate causality in the frequency domain by making a vanishing absorption approximation. Further, we will show that there can be subtle differences between Fourier transforming Maxwell equations and using a monochromatic source function. We discuss how these concepts can be obscured and offer some suggestions to improve the situation.

3.2 Introduction

When encountering Maxwell's equations in matter for the first time, students are faced with many conceptual, as well as mathematical, difficulties. In the time-domain, the four macroscopic Maxwell's equations, namely,

$$\begin{aligned}\nabla \cdot \mathbf{D} &= 4\pi\rho, & \nabla \cdot \mathbf{B} &= 0, \\ \nabla \times \mathbf{E} + \frac{1}{c} \frac{\partial \mathbf{B}}{\partial t} &= 0, & \nabla \times \mathbf{H} - \frac{1}{c} \frac{\partial \mathbf{D}}{\partial t} &= \frac{4\pi}{c} \mathbf{J},\end{aligned}\tag{3.1}$$

are straightforward enough. The problem arises in the constitutive relations connecting \mathbf{E} and \mathbf{D} or \mathbf{B} and \mathbf{H} . Whereas the time-domain Maxwell equations are real and involve only real quantities, the associated response functions are temporally non-local and their very definition involves integration with respect to time. To professionals, this issue is well understood and is almost always side-stepped notationally by writing the response equations as

$$\mathbf{D} = \epsilon \mathbf{E} \quad \text{and} \quad \mathbf{H} = \mu^{-1} \mathbf{B}, \quad (3.2)$$

and mentally juggling the time and frequency domains. Here, for simplicity, we have assumed that the medium is linear, isotropic and homogeneous (LIH). Experts understand that (3.2) means either

- (a) Fourier-domain relations of general validity (within LIH assumptions) or
- (b) time-domain relations valid only for monochromatic fields.

But to simultaneously present (3.1) and (3.2) to students (as is done in popular textbooks [1–3]) can mislead and confuse them; it obscures the important temporal non-locality of the response functions, mixes time and frequency domain concepts, and inserts complex quantities into manifestly real equations. To avoid a possible source of confusion, we use the phrase ‘Fourier-domain’ instead of ‘frequency-domain’ because the latter may also refer to a time-domain relation with a monochromatic source.

Moreover, students fail to understand the relationship between absorption, dispersion and causality (the effect cannot precede the cause [4]). To see the interplay between absorption, dispersion and causality pictorially, we follow Toll’s ingenious presentation [5] by considering an input signal $S(t)$ that is zero for $t < 0$. The input $S(t)$ is a weighted sum of many sinusoidal components, such as $C_1(t) = \sin(\omega_1 t + \psi_1)$, each of which extends from $t = -\infty$ to $t = \infty$. Notice that the weighted sum of all sinusoidal components produces a zero input signal for $t < 0$. If a system only absorbs one component, e.g., $C_1(t)$, without affecting other components, then the output of such a system would simply be $S(t) - C_1(t)$, which is

non-zero for $t < 0$, see Figure 3.1. Such a system is impossible because it violates causality; the output is non-zero before the onset of the input signal. Therefore, for causal systems, an absorption of one frequency must be accompanied by phase shifts of other frequencies in order to produce a zero output for $t < 0$, and the necessary phase shifts are prescribed by the dispersion relation. Moreover, the converse is true as well; namely, a phase shift of one frequency is necessarily accompanied by an absorption at other frequencies. From Toll's argument, we conclude that it is impossible to design a physical system that is causal and dispersionless. Therefore, when one speaks of dispersionless media, one violates a sacred physical principle (causality).

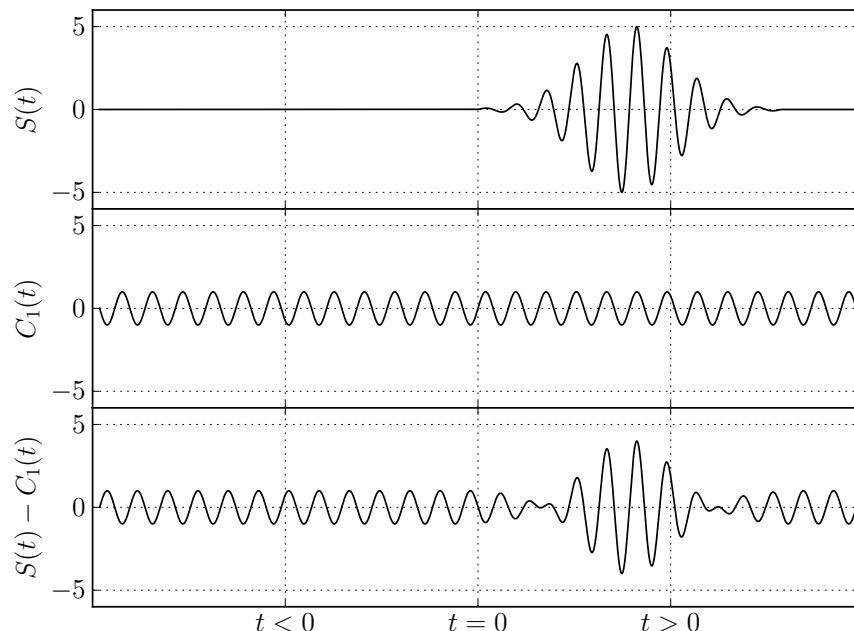


Figure 3.1: The input signal, $S(t)$, is shown along with the output signal, $S(t) - C_1(t)$, of a system that only absorbs the $C_1(t)$ component of $S(t)$, without affecting other components.

This paper is intended not only for instructors who teach advanced undergraduate and beginning graduate students, but also for the graduate students themselves. The mathematical sophistication needed to understand this paper is essentially that of a beginning graduate student. However, throughout the paper we extensively use the theory of the tempered distributions; with which a typical beginning graduate student may not be familiar.

To remedy this deficiency, we have included an example-driven tutorial on the formal theory of tempered distributions in the appendix.

3.3 Background

The time-domain relationship between \mathbf{D} and \mathbf{E} for a LIH and time-translationally invariant medium is given by⁶

$$\mathbf{D} = \mathbf{E} + 4\pi\mathbf{P} \quad \text{and} \quad \mathbf{P}(t) = \int_{-\infty}^{\infty} \chi(t-t')\mathbf{E}(t') dt', \quad (3.3a)$$

where

$$\chi(t-t') = \alpha(t-t')\Theta(t-t') \quad \text{and} \quad \Theta(t-t') = \begin{cases} 1, & t-t' > 0 \\ 0, & t-t' < 0 \end{cases}. \quad (3.3b)$$

The appearance of the Heaviside step function, Θ , in the definition of the electric susceptibility, χ , reminds us that the polarization vector, \mathbf{P} , can only depend on the past values of the applied electric field, \mathbf{E} . Therefore, (3.3) gives a causal relationship between the displacement field, \mathbf{D} , and the applied electric field. Taking the Fourier transform of (3.3) yields

$$\tilde{\mathbf{D}}(\omega) = \tilde{\mathbf{E}}(\omega) + 4\pi\tilde{\mathbf{P}}(\omega) \quad \text{and} \quad \tilde{\mathbf{P}}(\omega) = \tilde{\chi}(\omega)\tilde{\mathbf{E}}(\omega), \quad (3.4)$$

with the Fourier transform pair given by

$$\tilde{f}(\omega) = \mathcal{F}[f(t)] = \int_{-\infty}^{\infty} f(t)e^{+i\omega t} dt, \quad (3.5a)$$

$$f(t) = \mathcal{F}^{-1}[\tilde{f}(\omega)] = \frac{1}{2\pi} \int_{-\infty}^{\infty} \tilde{f}(\omega)e^{-i\omega t} d\omega. \quad (3.5b)$$

Under suitable mathematical conditions, the principle of causality in the time-domain translates into the Kramers–Kronig (KK) relations (the Hilbert transform pair) in the Fourier-domain, namely,

⁶For our purposes, it is more convenient to work with (3.3) than with $\mathbf{D} = \int_{-\infty}^{\infty} \epsilon(t-t')\mathbf{E}(t') dt'$, where $\epsilon(t-t') = \delta(t-t') + 4\pi\chi(t-t')$.

$$\mathrm{Im}\tilde{\chi}(\omega) = \mathcal{H} [\mathrm{Re}\tilde{\chi}(\eta)] = -\frac{1}{\pi} \oint_{-\infty}^{\infty} \frac{\mathrm{Re}\tilde{\chi}(\eta)}{\eta - \omega} d\eta, \quad (3.6a)$$

$$\mathrm{Re}\tilde{\chi}(\omega) = \mathcal{H}^{-1} [\mathrm{Im}\tilde{\chi}(\eta)] = \frac{1}{\pi} \oint_{-\infty}^{\infty} \frac{\mathrm{Im}\tilde{\chi}(\eta)}{\eta - \omega} d\eta, \quad (3.6b)$$

where $\mathrm{Re}\tilde{\chi}(\omega)$ and $\mathrm{Im}\tilde{\chi}(\omega)$ are the real and imaginary parts of $\tilde{\chi}(\omega)$, respectively, and \oint denotes the Cauchy principal value integral. In free space, by definition, $\chi(t - t') = 0$ and consequently, the KK relations are trivially satisfied. The KK relations can be derived in ‘two lines’ by using the Fourier representation of the Heaviside step function and utilizing the freedom to define $\alpha(t - t')$ for $t - t' < 0$ [6]. A lengthier but more traditional derivation of the KK relations is available in [7]. This derivation is self-contained and does not assume *a priori* knowledge of the theory of functions of a complex variable. For a historically accurate account on how the KK relations were first derived, see [8].

In general, it is difficult to establish an equivalence between the KK relations (3.6) and causality (3.3b). If $\tilde{\chi}(\omega)$ is a square-integrable function, then the Titchmarsh theorem [9] guarantees that (3.6) and (3.3b) are equivalent. In other words, $\chi(t - t') \propto \Theta(t - t')$ if and only if $\tilde{\chi}(\omega)$ satisfies (3.6). The square-integrability requirement on $\tilde{\chi}(\omega)$ may be somewhat relaxed. It can be shown that if $\tilde{\chi}(\omega)$ is bounded but $\mathbf{E}(t)$ and $\mathbf{P}(t)$ are square-integrable functions, then (3.6) and (3.3b) are equivalent [5]. Unfortunately, these conditions are generally not satisfied, in fact, they are not even satisfied in the idealized examples considered in this paper. Therefore, we must part with our naïve notion that χ is a classical function and treat it as a generalized function (distribution). For our purposes, it will be sufficient to treat $\chi(t)$ as a tempered distribution. A reader not familiar with the formal theory of the tempered distributions should read the appendix which, for our purposes, serves as a self-contained tutorial on tempered distributions. For the reader’s convenience, Table 3.1 provides a summary of the notation introduced in the appendix. From this point on, unless explicitly noted otherwise, the symbol $\chi(t)$ should be interpreted as a tempered distribution, i.e. $\chi(t) \in S'$. Consequently, the convolution integral in (3.3a) and the Fourier transform

Table 3.1: A brief description of the symbols introduced in the appendix.

Symbol	Description
S	The Schwartz class
S'	The class of tempered distributions
$\langle f, \phi \rangle = \int_{-\infty}^{\infty} f(t)\phi(t) dt$	Tempered distribution f ; $f \in S'$ and $\phi \in S$
$(f * \psi)(t) = \int_{-\infty}^{\infty} f(t - t')\psi(t') dt'$	Convolution of f with ψ ; $f \in S'$ and $\psi \in S$
$\text{supp}[f]$	Support of f ; $f \in S'$

pair given by (3.5) should also be interpreted in a distributional sense; see appendix A.1.1. Strictly speaking, the Hilbert transform pair given by (3.6) should also be interpreted in a distribution sense. However, for our purposes, it will be sufficient to think of the Hilbert transform as a ‘generalized’ convolution of the singular function $1/\omega$ (Hilbert kernel) with a tempered distribution $\tilde{f}(\omega)$. For a more mathematical treatment of the Hilbert transform of the tempered distributions, see [10–13]. In 1958, Taylor [14] (also, see discussion in [15]) rigorously established the equivalence between causality and the KK relations when $\tilde{\chi}(\omega)$ is a tempered distribution. This is a very important result that we will use repeatedly. We will force $\tilde{\chi}(\omega) \in S'$ to satisfy the KK relations, thereby guaranteeing that $\chi(t - t')$ vanishes for $t - t' < 0$. In other words, Taylor’s result gives causality meaning in the Fourier-domain.

To explore these fundamental issues in a pedagogical context, we will consider two textbook models that are used to derive or explain the dispersion of electromagnetic waves. The first is the Drude model of conduction in metals. The second is the damped harmonic oscillator, which arises in semi-classical models of atomic absorption. The former is just a damped harmonic oscillator model with a spring constant of zero, and where we interpret the damping in terms of electron collisions.

3.4 Drude model

In a metal, the motion of a conduction electron of charge $-e$ and mass m under the influence of an electric field \mathbf{E} is given by

$$\frac{d^2 \mathbf{r}}{dt^2} + \frac{1}{\tau} \frac{d\mathbf{r}}{dt} = -\frac{e}{m} \mathbf{E}, \quad (3.7a)$$

where τ is the collision mean free time [16]. Substituting $\delta(t - t')\mathbf{n}$ for \mathbf{E} and taking the Fourier transform, see appendix A.1.1, yields

$$\omega \left(\omega + \frac{i}{\tau} \right) \tilde{\mathbf{g}}(\omega) = \frac{e}{m} \tilde{\mathbf{E}}(\omega) \quad \text{and} \quad \tilde{\mathbf{E}}(\omega) = e^{+i\omega t'} \mathbf{n}, \quad (3.7b)$$

where $\tilde{\mathbf{g}}(\omega)$ denotes the Green's function, $\mathbf{n} = \frac{1}{\sqrt{3}}(\mathbf{x} + \mathbf{y} + \mathbf{z})$, and $\{\mathbf{x}, \mathbf{y}, \mathbf{z}\}$ is the standard basis for the three-dimensional space. Using $\tilde{\mathbf{P}}(\omega) = -n_c e \tilde{\mathbf{g}}(\omega)$, we see that the electric susceptibility is given by

$$\omega \left(\omega + \frac{i}{\tau} \right) \tilde{\chi}(\omega) = -\frac{e^2 n_c}{m}, \quad (3.8a)$$

where n_c denotes the conduction electron density (assumed to be constant). When solving (3.8a) for $\tilde{\chi}(\omega)$ we must remember that $\tilde{\chi}(\omega)$ is a tempered distribution; in other words, we seek a *distributional* solution to (3.8a). The distributional solution consists of two parts; the *particular* part, $\tilde{\chi}_p(\omega)$, given by the 'naïve division' of (3.8a), namely,

$$\tilde{\chi}_p(\omega) = -\frac{\sigma_0}{\omega(\tau\omega + i)}, \quad (3.8b)$$

where $\sigma_0 = e^2 n_c \tau / m$ is the static conductivity, and the *homogeneous* part, $\tilde{\chi}_h(\omega)$, which satisfies

$$\left\langle \omega \left(\omega + \frac{i}{\tau} \right) \tilde{\chi}_h(\omega), \phi(\omega) \right\rangle = \langle 0, \phi(\omega) \rangle \quad (3.8c)$$

for all $\phi \in S$. The solution to (3.8c) is of the form of (A.28) and *not* of (A.36) because $\omega + i/\tau$ never equals zero for real ω and finite τ . In other words, $\text{supp}[\tilde{\chi}_h(\omega)] = \{0\}$ and *not* $\{0, -i/\tau\}$. Therefore, as shown in the first example in appendix A.1.2, the form of the full

solution to (3.8a) is given by

$$\tilde{\chi}(\omega) = -\sigma_0 \left(\frac{1}{\omega(\tau\omega + i)} + \tilde{\chi}_h(\omega) \right), \quad \text{where} \quad \tilde{\chi}_h(\omega) = c_0 \delta(\omega). \quad (3.8d)$$

To find the unknown constant c_0 , we require that the response of the system be causal. According to Taylor [14], the causality requirement is the same thing as requiring that $\text{Im}\tilde{\chi} = \mathcal{H}[\text{Re}\tilde{\chi}]$, which yields $c_0 = -\pi$. Therefore, the *causal* electric susceptibility is given by

$$\tilde{\chi}(\omega) = -\sigma_0 \left(\frac{1}{\omega(\tau\omega + i)} - \pi\delta(\omega) \right), \quad (3.9a)$$

$$\chi(t - t') = \mathcal{F}^{-1}[\tilde{\chi}(\omega)] = \sigma_0 \left(1 - e^{-\frac{t-t'}{\tau}} \right) \Theta(t - t'). \quad (3.9b)$$

Notice that $\chi(t - t')$ is zero for $t < t'$ and increases monotonically to its maximum value of σ_0 for $t > t'$. The rate of the increase is controlled by the collision mean free time. In the next two subsections, we will study the effects of $\chi(t - t')$ on the response functions when a constant or monochromatic electric field is applied.

3.4.1 A constant electric field

Suppose now that a constant electric field, \mathbf{E}_0 , was turned on at $t' = 0$. Substituting $\mathbf{E}(t') = \mathbf{E}_0\Theta(t')$ and (3.9b) into (3.3a) yields

$$\mathbf{P}(t) = \sigma_0 \left(t - \tau + \tau e^{-\frac{t}{\tau}} \right) \mathbf{E}_0\Theta(t), \quad (3.10a)$$

and the current density is given by

$$\mathbf{J}(t) = \frac{\partial \mathbf{P}}{\partial t} = \sigma_0 \left(1 - e^{-\frac{t}{\tau}} \right) \mathbf{E}_0\Theta(t). \quad (3.10b)$$

The time dependence in (3.10b) reminds us that when we connect a wire to a battery, the current in the wire does not *instantaneously* reach its Ohm's law steady-state value. The rate at which the current reaches the steady-state value is controlled by the collision mean free time τ , as evident from the exponential term in (3.10b). Of course, (3.10b) reduces to Ohm's law, $\mathbf{J} = \sigma_0 \mathbf{E}_0$, when $t \gg \tau$.

3.4.2 A monochromatic field

Another simple situation is a monochromatic driving field of angular frequency ω_d that has existed since the beginning of time ($t' = -\infty$). Substituting $\mathbf{E}(t') = \mathbf{E}_0 \cos(\omega_d t')$ and (3.9b) into (3.3a) yields

$$\mathbf{D}(t) = A_1 \mathbf{E}_0 \cos(\omega_d t) + A_2 \mathbf{E}_0 \sin(\omega_d t), \quad (3.11a)$$

where

$$A_1 = 1 - \frac{4\pi\sigma_0\tau}{1 + \tau^2\omega_d^2} \quad \text{and} \quad A_2 = \frac{4\pi\sigma_0}{\omega_d(1 + \tau^2\omega_d^2)}. \quad (3.11b)$$

From (3.11a), we see that $\mathbf{D}(t)$ has one component that oscillates in-phase and one component that oscillates out-of-phase with the applied field. The out-of-phase oscillations are caused by collisions of the electrons with the ions (absorption). We can put (3.11) into a form of (3.2) if we let

$$\check{\epsilon} = A_1 + iA_2 \quad \text{and} \quad \check{\mathbf{E}} = \mathbf{E}_0 e^{-i\omega_d t}; \quad (3.12a)$$

then, (3.11) becomes

$$\mathbf{D}(t) = \text{Re}(\check{\epsilon} \check{\mathbf{E}}). \quad (3.12b)$$

Notice that, in general, $\mathbf{D}(t) \neq \text{Re}(\check{\epsilon})\text{Re}(\check{\mathbf{E}})$. Thus, what professionals mean by (3.2) is really (3.12) if they are talking about a monochromatic applied field. But what is $\check{\epsilon}$? To answer this question, let's rewrite (3.12a) in an illuminating form, namely,

$$\frac{\check{\epsilon} - 1}{4\pi} = \check{\chi}(\omega_d) = -\frac{\sigma_0}{\omega_d(\tau\omega_d + i)}. \quad (3.13)$$

Notice that (3.13) has a simple pole at $\omega_d = 0$. The root cause of this pole is our assumption that the medium is homogeneous, and the definition of homogeneity clearly depends on the spatial wavelength of the interrogating field [17, 18]. Thus, (3.13) may be devoid of physical reality near $\omega_d = 0$. Be that as it may, the resemblance between $\check{\chi}(\omega_d)$ and $\tilde{\chi}(\omega)$ is uncanny if we replace ω_d with ω in (3.13). But is such a comparison of $\check{\chi}$ and $\tilde{\chi}$ meaningful? Strictly speaking, it is *not*, because $\check{\chi}$ is a classical (ordinary) function and $\tilde{\chi}$ is a tempered

distribution (generalized function). Nevertheless, we want to compare these two objects by ‘promoting’ $\tilde{\chi}$ to be a generalized function. Let $X(\omega) = \tilde{\chi}(\omega) - \check{\chi}(\omega)$, then

$$\langle X(\omega), \phi(\omega) \rangle = \int_{-\infty}^{\infty} \pi \sigma_0 \delta(\omega) \phi(\omega) d\omega = \pi \sigma_0 \phi(0) \quad (3.14)$$

for all $\phi \in S$. From (3.14), we see that $\text{supp}[X(\omega)] = \{0\}$, i.e. the ‘promoted’ $\tilde{\chi}(\omega)$ and $\check{\chi}(\omega)$ differ in a *neighbourhood* of $\omega = 0$. In the laboratory, we actually make a Fourier-domain ‘measurement’ in the *time-domain* by driving the system for a very long time with a monochromatic field [19]. Thus, we experimentally measure $\tilde{\chi}(\omega_d)$ and not $\tilde{\chi}(\omega)$. Moreover, it is the $\tilde{\chi}(\omega)$ that satisfies the KK relations and not the $\tilde{\chi}(\omega_d)$, even if we ‘promote’ $\tilde{\chi}(\omega_d)$ to a generalized function. This crucial difference between $\tilde{\chi}(\omega)$ and $\tilde{\chi}(\omega_d)$ is often missed by students.

A mathematically inclined reader might object to the usage of $\mathbf{E}(t') = \mathbf{E}_0 \cos(\omega_d t')$ for a driving field. Clearly, $\cos(\omega_d t') \notin S$ but we have only defined the convolution (A.18) between a distribution in S' and a function in S . Of course, physically we know that a starving graduate student had to turn the field on and off. If we assume that the field was turned on/off in a smooth and slow fashion, then it could be approximated by $\cos(\omega_d t') \exp[-(at')^2]$, which does belong to the space S . A similar physical argument can be used to justify the usage of the Heaviside step function in Section 3.4.1. Moreover, under certain conditions, it is possible to define convolution of two tempered distributions [20]. This definition is beyond the scope of this paper but, if used, it would eliminate the need for the above physical argument.

3.5 Plasma

A limiting case of the Drude model is dilute neutral plasma with very large collision mean free time. If we try to expand (3.9a) around $1/\tau = 0$, we will obtain a non-causal $\tilde{\chi}(\omega)$ because the homogeneous solution $\tilde{\chi}_h(\omega)$ changes form in this limiting case. To see this, expand (3.8c) around $1/\tau = 0$ to obtain

$$\langle \omega^2 \tilde{\chi}_h(\omega), \phi(\omega) \rangle = \langle 0, \phi(\omega) \rangle, \quad (3.15a)$$

for all $\phi \in S$. The form of the solution to (3.15a) is given by, see (A.31),

$$\tilde{\chi}_h(\omega) = c_0\delta(\omega) + c_1\delta'(\omega), \quad (3.15b)$$

which differs from the homogeneous part of (3.9a) by a $\delta'(\omega)$ term. Therefore, the full solution to $\omega^2\tilde{\chi}(\omega) = -e^2n_c/m$ is given by

$$\tilde{\chi}(\omega) = -\frac{\omega_p^2}{4\pi} \left(\frac{1}{\omega^2} + c_0\delta(\omega) + c_1\delta'(\omega) \right), \quad (3.15c)$$

where $\omega_p^2 = 4\pi e^2n_c/m$ and ω_p is called the angular plasma frequency. To find the unknown constants, c_0 and c_1 , we use Taylor's causality requirement, $\text{Im}\tilde{\chi} = \mathcal{H}[\text{Re}\tilde{\chi}]$, which yields $c_0 = 0$ and $c_1 = i\pi$. Therefore, the *causal* electric susceptibility is given by

$$\tilde{\chi}(\omega) = -\frac{\omega_p^2}{4\pi} \left(\frac{1}{\omega^2} + i\pi \frac{d}{d\omega} \delta(\omega) \right), \quad (3.16a)$$

$$\chi(t-t') = \mathcal{F}^{-1}[\tilde{\chi}(\omega)] = \frac{e^2n_c}{m} (t-t') \Theta(t-t'). \quad (3.16b)$$

We compare (3.16a) to a common textbook expression for the electric susceptibility of dilute neutral plasma, given by [16]

$$\tilde{\chi}(\omega) = -\frac{\omega_p^2}{4\pi} \frac{1}{\omega^2}. \quad (3.17)$$

This differs from (3.16a) in a neighbourhood of $\omega = 0$. The difference is caused by the fact that (3.16a) is causal and valid for all ω , unlike the textbook version (3.17), which is only valid for high enough frequencies, namely, $\omega \gg 1/\tau$.

The above example illustrates that the approximation in the Fourier-domain must be done with care if we insist on a causal electric susceptibility. It is interesting to note that no such care is necessary if the approximation is done in the time-domain. For example, expanding (3.9b) around $(t-t')/\tau = 0$ immediately yields (3.16b), which is clearly causal.

3.5.1 Plasma in a constant electric field

Next, let us consider a plasma in a constant electric field \mathbf{E}_0 that was turned on at $t' = 0$. Substituting $\mathbf{E}(t') = \mathbf{E}_0\Theta(t')$ and (3.16b) into (3.3a) yields

$$\mathbf{P}(t) = \frac{e^2 n_c}{2m} t^2 \mathbf{E}_0 \Theta(t). \quad (3.18)$$

From (3.16b) and (3.18), we see that the electric susceptibility is linear in time and that the polarization vector is quadratic in time. The quadratic dependence of $\mathbf{P}(t)$ on time signifies that the dilute neutral plasma is accelerating uniformly under the influence of the applied static electric field. Moreover, from (3.3a), we see that \mathbf{D} grows quadratically in time and that at $t = 0$, the response field \mathbf{D} is equal to the applied field \mathbf{E}_0 .

3.5.2 Plasma in a monochromatic electric field

Finally, if we drive the plasma with a monochromatic field of angular frequency ω_d that existed since $t' = -\infty$, we will see another source of confusion for students. Substituting $\mathbf{E}(t') = \mathbf{E}_0 \cos(\omega_d t')$ and (3.16b) into (3.3a) yields

$$\mathbf{D}(t) = \check{\epsilon} \mathbf{E}(t) \quad \text{and} \quad \check{\epsilon} - 1 = 4\pi \check{\chi}(\omega_d) = -\frac{\omega_p^2}{\omega_d^2}. \quad (3.19)$$

Again, if we replace ω_d with ω in (3.19) and ‘promote’ $\check{\chi}(\omega)$ to be a tempered distribution, then the ‘promoted’ $\check{\chi}(\omega)$ differs from $\tilde{\chi}(\omega)$ only in a neighbourhood of $\omega = 0$. Also, notice that all quantities in (3.19) are purely real. Of course, $\mathbf{D}(t)$ oscillates in-phase with $\mathbf{E}(t)$ because we have effectively ignored collisions (absorption) in our approximation. If we let $\check{\mathbf{E}} = \mathbf{E}_0 \exp(-i\omega_d t)$, then (3.19) may be written as $\mathbf{D}(t) = \text{Re}(\check{\epsilon})\text{Re}(\check{\mathbf{E}})$, which to a student may confirm an improper interpretation of (3.2).

3.6 Damped harmonic oscillator

A damped harmonic oscillator is a simple model for the motion of a bound electron in a dielectric. The equation of motion in the time-domain is given by

$$\frac{d^2 \mathbf{r}}{dt^2} + \gamma \frac{d\mathbf{r}}{dt} + \omega_0^2 \mathbf{r} = -\frac{e}{m} \mathbf{E}, \quad (3.20a)$$

where ω_0 is the natural angular frequency and γ is the radiation damping. The Green's function for (3.20a) (obtained in the same manner and notation as in Section 3.4) is

$$(\omega - \omega_+) (\omega - \omega_-) \tilde{\mathbf{g}}(\omega) = \frac{e}{m} \tilde{\mathbf{E}}(\omega), \quad (3.20b)$$

where

$$\omega_{\pm} = \pm s - i\frac{\gamma}{2} \quad \text{and} \quad s = \sqrt{\omega_0^2 - \left(\frac{\gamma}{2}\right)^2}. \quad (3.20c)$$

If we assume that each electron in the dielectric oscillates with the same natural angular frequency, then using $\tilde{\mathbf{P}}(\omega) = -en_b \tilde{\mathbf{g}}(\omega)$ yields

$$(\omega - \omega_+) (\omega - \omega_-) \tilde{\chi}(\omega) = -\frac{e^2 n_b}{m}, \quad (3.21a)$$

where n_b denotes the density of the bounded electrons (assumed to be constant). From (3.21a), we see that $\tilde{\chi}(\omega)$ has two simple poles in the complex ω -plane. As we will soon see, the location of these poles in the complex ω -plane will dictate the form of the homogeneous solution, $\tilde{\chi}_h(\omega)$. First, consider the simplest under-damped case, namely when $s > 0$ and $\gamma \neq 0$. In this case, $\omega - \omega_+$ and $\omega - \omega_-$ never equal zero for real ω . Therefore, the homogeneous solution is simply zero, $\tilde{\chi}_h(\omega) = 0$, and the *full* solution is given by

$$\tilde{\chi}(\omega) = -\frac{e^2 n_b}{m} \frac{1}{(\omega - \omega_+) (\omega - \omega_-)}, \quad (3.21b)$$

$$\chi(t - t') = \mathcal{F}^{-1} [\tilde{\chi}(\omega)] = \frac{e^2 n_b}{m} \frac{e^{-\frac{\gamma}{2}(t-t')} \sin[s(t-t')]}{s} \Theta(t - t'). \quad (3.21c)$$

Notice that we didn't have to impose Taylor's causality requirement, $\text{Im}\tilde{\chi} = \mathcal{H}[\text{Re}\tilde{\chi}]$, as it was 'automatically' satisfied by (3.21b).

To get a better understanding of (3.21c), let's put it in a constant electric field that turns on at $t' = 0$. Substituting $\mathbf{E}(t') = \mathbf{E}_0 \Theta(t')$ and (3.21c) into (3.3a) yields

$$\mathbf{P}(t) = \mathbf{P}_0 \left[1 - e^{-\frac{\gamma}{2}t} \left(\cos(st) + \frac{\gamma \sin(st)}{2s} \right) \right] \Theta(t), \quad (3.22a)$$

where

$$\mathbf{P}_0 = \frac{e^2 n_b}{m\omega_0^2} \mathbf{E}_0. \quad (3.22b)$$

From (3.22), we see that $\mathbf{P}(t)$ monotonically increases from zero at $t = 0$ to some maximum value, and then oscillates around \mathbf{P}_0 before finally settling at \mathbf{P}_0 . The oscillations around \mathbf{P}_0 remind us that the bounded electrons oscillate around the new equilibrium position.

In the case of vanishing radiation damping, we may set $\gamma = 0$ in (3.21c) to obtain

$$\chi(t - t') = \frac{e^2 n_b}{m \omega_0} \sin [\omega_0(t - t')] \Theta(t - t'), \quad (3.23)$$

which is clearly causal. But if we set $\gamma = 0$ in (3.21b), we would violate causality! To obtain a causal $\tilde{\chi}(\omega)$, we set $\gamma = 0$ in (3.21a) to obtain

$$(\omega - \omega_0)(\omega + \omega_0) \tilde{\chi}(\omega) = -\frac{e^2 n_b}{m}. \quad (3.24a)$$

From (A.35) and (A.36), we see that the form of the full solution to (3.24a) is given by

$$\tilde{\chi}(\omega) = \frac{e^2 n_b}{2m\omega_0} \left[\frac{1}{\omega + \omega_0} - \frac{1}{\omega - \omega_0} + \tilde{\chi}_h(\omega) \right], \quad (3.24b)$$

where

$$\tilde{\chi}_h(\omega) = b_0 \delta(\omega + \omega_0) + c_0 \delta(\omega - \omega_0). \quad (3.24c)$$

As in previous examples, we find the unknown constants, b_0 and c_0 , via Taylor's causality requirement, $\text{Im} \tilde{\chi} = \mathcal{H} [\text{Re} \tilde{\chi}]$, which yields $b_0 = -i\pi$ and $c_0 = i\pi$. Therefore, the full casual solution to (3.24a) is given by

$$\tilde{\chi}(\omega) = \frac{n_b e^2}{2m\omega_0} \left[\frac{1}{\omega + \omega_0} - i\pi \delta(\omega + \omega_0) - \frac{1}{\omega - \omega_0} + i\pi \delta(\omega - \omega_0) \right], \quad (3.24d)$$

and the inverse Fourier transform of (3.24d), of course, yields (3.23). From the above example, we again conclude that when considering limiting cases of the electric susceptibility in the Fourier-domain, we must be careful not to inadvertently violate causality. However, in the time-domain, we don't have to worry about the solution not reducing to a proper form in these limiting cases.

3.7 Concluding remarks

In this paper, we have taken a somewhat contrarian approach to the linear response laws of classical electrodynamics by looking at the response functions in the time-domain. The advantage of the time-domain is that all quantities are purely real and causality is naturally expressed in terms of time. The disadvantage is that the response functions are temporally non-local, so most of us get tired of writing convolutions on the blackboard and quickly slip into a short-hand mix of time and frequency/Fourier domain notations that can confuse students profoundly.

While it is perfectly reasonable to avoid complications, such as dispersion, in introductory physics courses, by the time students are in their third or fourth year of physics study, it is important to expose them to the fundamental principles associated with a classical, macroscopic picture of matter. In particular, we believe that the following should be emphasized:

- Causality is easy to enforce in the time-domain, but the constitutive relations are non-local in time and involve convolution integrals.
- The constitutive relations are mathematically simple in the Fourier-domain, but causality is given by the Kramers–Kronig relations (the Hilbert transform pair).
- We should make it clear whether we are really transforming into the Fourier-domain, or whether we are assuming a monochromatic source in a time-domain experiment. Very often the results look the same, but as we have shown, confusing the two can lead to serious misunderstandings.
- Finally, it should be emphasized that Maxwell’s equations (in the time-domain) are purely real and involve only purely real quantities. The Fourier transformation promotes variables to the complex plane. As teachers, we should be careful when speaking of the real and imaginary parts of the response function, and preface our remarks with a note that we are working in the non-physical, but highly useful, Fourier-domain.

3.8 Acknowledgment

This material is based upon work supported in part by the U.S. Office of Naval Research as a Multi-disciplinary University Research Initiative on Sound and Electromagnetic Interacting Waves under grant number N00014-10-1-0958.

3.9 References Cited

- [1] D. J. Griffiths, Introduction to Electrodynamics, Prentice Hall, Upper Saddle River, NJ, third edition, pp. 382–383.
- [2] M. A. Heald, J. B. Marion, Classical Electromagnetic Radiation, Saunders, Fort Worth, TX, third edition, pp. 167–168.
- [3] I. S. Grant, W. R. Phillips, Electromagnetism, John Wiley & Sons, Chichester, second edition, p. 356.
- [4] P. Kinsler, How to be causal: time, spacetime and spectra, Eur. J. Phys. 32 (2011) 1687.
- [5] J. S. Toll, Causality and the dispersion relation: Logical foundations, Phys. Rev. 104 (1956) 1760–1770.
- [6] B. Y.-K. Hu, Kramers–Kronig in two lines, Am. J. Phys. 57 (1989) 821.
- [7] J. R. Reitz, F. J. Milford, R. W. Christy, Foundations of electromagnetic theory, Addison-Wesley, Reading, MA, fourth edition, pp. 610–615.
- [8] C. F. Bohren, What did Kramers and Kronig do and how did they do it?, Eur. J. Phys. 31 (2010) 573.
- [9] E. C. Titchmarsh, Introduction to the theory of Fourier Integrals, Clarendon Press, Oxford, second edition, pp. 128–129.
- [10] E. Beltrami, M. Wohlers, The Cauchy integral of tempered distributions and some theorems on analytic continuation, SIAM J. Appl. Math. 15 (1967) 1077–1087.
- [11] M. Orton, Hilbert transforms, Plemelj relations, and Fourier transforms of distributions, SIAM J. Math. Anal. 4 (1973) 656–670.
- [12] S. Ishikawa, Generalized Hilbert transforms in tempered distributions, Tokyo J. Math. 10 (1987) 119–132.

- [13] J. N. Pandey, The Hilbert transform of Schwartz distributions and applications, John Wiley & Sons, New York.
- [14] J. G. Taylor, Dispersion relations and Schwartz's distributions, *Annals of Physics* 5 (1958) 391–398.
- [15] F. W. King, Hilbert Transforms, volume 2, Cambridge University Press, New York, pp. 110–117.
- [16] N. W. Ashcroft, N. D. Mermin, Solid State Physics, Saunders College, Philadelphia.
- [17] L. D. Landau, E. M. Lifshitz, L. P. Pitaevskiĭ, Electrodynamics of Continuous Media, volume 8, Pergamon Press, Oxford, second edition.
- [18] M. Dressel, G. Grüner, Electrodynamics of Solids: Optical Properties of Electrons in Matter, Cambridge University Press, Cambridge.
- [19] B. J. Zadler, A. Grêt, J. A. Scales, Spectroscopy versus interferometry: Resolving small changes, *Am. J. Phys.* 73 (2005) 837–844.
- [20] L. Schwartz, Théorie des distributions, Hermann, Paris, pp. 243–248.
- [21] R. S. Strichartz, A Guide to distribution theory and Fourier transforms, World Scientific, River Edge, NJ, 2003.
- [22] A. Papoulis, The Fourier integral and its applications, McGraw-Hill, New York, pp. 281–282.
- [23] M. J. Lighthill, Introduction to Fourier Analysis and Generalised Functions, Cambridge University Press, London, 1959.
- [24] R. P. Kanwal, Generalized Functions Theory and Applications, Birkhäuser, Boston, third edition, 2004.
- [25] A. H. Zemanian, Distribution Theory and Transform Analysis, McGraw-Hill, New York, 1965.
- [26] I. M. Gel'fand, G. E. Shilov, Generalized Functions, volume 1, Academic Press, New York, 1964.

[27] J. D. Jackson, Classical Electrodynamics, John Wiley & Sons, New York, third edition, pp. 69–70.

A.1 Appendix A - Distribution theory

The ordinary (classical) functions may be thought of as a mapping between two sets of numbers. We can extend the idea of an ordinary function by considering a mapping (functional, if you will) between a set of *functions* and a set of numbers. The physical reason for extending the idea of an ordinary function lies in our inability to *experimentally* measure a function at a point, e.g., see [21, pp. 1–2], [22]. Let $f(x)$ represent temperature at some point x . To measure the temperature at that point, we place a thermometer there to obtain a value for $f(x)$, but do we actually obtain a value of the temperature at point x ? The bulb of the thermometer has finite size; thus, what we measure is an average temperature *around* the point x . Mathematically an average is a weighted sum, and our measurement only reveals the value $T_1 = \int f(x)\phi_1(x) dx$, where $\phi_1(x)$ is essentially zero away from the bulb of the thermometer. If we make another measurement of the temperature at point x using a different thermometer, then we would measure $T_2 = \int f(x)\phi_2(x) dx$, and hopefully, the ‘true’ temperature $T \approx (T_1 + T_2)/2$. The above discussion is meant to serve as a physical motivation for defining what we will call *generalized functions* as certain linear functionals. Generalized functions are also called *distributions*, and we will use both terms interchangeably. Our presentation of the generalized functions closely follows that of Strichartz [21]. A reader interested in a more detailed study may also find [23–26] helpful.

For our purposes, it will be sufficient to consider only a special class of distributions, namely, the *tempered* distributions. Before we can formally define tempered distributions, we must first define a set of ‘good’ functions. This set of ‘good’ functions is also called the *space of test functions*. For the tempered distributions, the space of test functions, denoted by S , contains all real or complex-valued functions $\phi(t)$ that are classically infinitely differentiable and, along with all its derivatives, vanish at infinity faster than the reciprocal of any polynomial. For example, any function of the form $\sum_{n=0}^N c_n t^n \exp(-t^2)$ belongs to

S . We are now ready to define the class of tempered distributions, denoted by S' , as all continuous⁷ *linear functionals* on S . A linear functional f on S is a rule by which we assign to *every* test function $\phi(t)$ a (real or complex) number denoted by $\langle f, \phi \rangle$, such that the identity $\langle f, c_1\phi_1 + c_2\phi_2 \rangle = c_1 \langle f, \phi_1 \rangle + c_2 \langle f, \phi_2 \rangle$ is satisfied for arbitrary test functions ϕ_1 and ϕ_2 and (real or complex) numbers c_1 and c_2 . The terminology and notation used for distributions can be confusing at times because the phrase ‘function f or even generalized function (distribution) f ’ may refer to f itself or to the value of $\langle f, \phi \rangle$. In other words, no distinction is made between a distribution and a ‘function’ from which the distribution was obtained.⁸ To make the notion of tempered distributions more concrete let’s consider a few simple examples. Let’s find a distribution defined by $f = \Theta'(t)$, i.e.

$$\begin{aligned} \mathcal{T}_f &= \left\langle \frac{d\Theta(t)}{dt}, \phi(t) \right\rangle \\ &= \int_{-\infty}^{\infty} \frac{d\Theta(t)}{dt} \phi(t) dt = - \int_{-\infty}^{\infty} \Theta(t) \frac{d\phi(t)}{dt} dt \end{aligned} \quad (\text{A.1})$$

$$= - \int_0^{\infty} \frac{d\phi(t)}{dt} dt = -(\phi(\infty) - \phi(0)) = \phi(0), \quad (\text{A.2})$$

where we integrated by parts in (A.1) and the integrated terms vanished because ϕ is a ‘good’ function, i.e. $\phi \in S$. By comparing (A.2) to the sifting property of the Dirac delta function

$$\langle \delta(t), \phi(t) \rangle = \int_{-\infty}^{\infty} \delta(t) \phi(t) dt = \phi(0), \quad (\text{A.3})$$

we conclude that the (generalized) derivative of the Heaviside step function equals the Dirac delta function. We can even differentiate (in a distributional sense, of course) more complicated functions. Let $f = g(t)\delta'(t)$, where $g(t)$ is a polynomial of any degree; then

⁷The definition of continuity of linear functionals is rather technical and not necessary for our purposes.

⁸Strictly speaking, this is an abuse of terminology but it is so common that one must be aware of it. Moreover, one often speaks of generalized functions (distributions) as if they were proper functions, e.g., the Dirac delta function $\delta(t)$.

$$\begin{aligned}\mathcal{T}_f &= \left\langle g(t) \frac{d\delta(t)}{dt}, \phi(t) \right\rangle \\ &= \int_{-\infty}^{\infty} \left(g(t) \frac{d\delta(t)}{dt} \right) \phi(t) dt = \int_{-\infty}^{\infty} \frac{d\delta(t)}{dt} \left(g(t) \phi(t) \right) dt.\end{aligned}\tag{A.4}$$

Integrating by parts and noticing that the product of $g(t)$ and $\phi(t)$ is still in S (so that the integrated terms vanish), yields

$$\begin{aligned}\mathcal{T}_f &= - \int_{-\infty}^{\infty} \delta(t) \left(g(t) \frac{d\phi(t)}{dt} + \frac{dg(t)}{dt} \phi(t) \right) dt \\ &= -g(0)\phi'(0) - g'(0)\phi(0).\end{aligned}\tag{A.5}$$

We can write (A.5) in a more standard form that doesn't involve the derivatives of $\phi(t)$.

Using (A.3) and noting that

$$\langle \delta'(t), \phi(t) \rangle = \int_{-\infty}^{\infty} \frac{d\delta(t)}{dt} \phi(t) dt = - \int_{-\infty}^{\infty} \delta(t) \frac{d\phi(t)}{dt} dt = -\phi'(0),$$

we obtain

$$\left\langle g(t) \frac{d\delta(t)}{dt}, \phi(t) \right\rangle = \langle g(0)\delta'(t), \phi(t) \rangle - \langle g'(0)\delta(t), \phi(t) \rangle.\tag{A.6}$$

It is a very common abuse of notation to ‘drop’ the \langle , \rangle brackets, along with $\phi(t)$, and write (A.6) simply as

$$g(t)\delta'(t) = g(0)\delta'(t) - g'(0)\delta(t).\tag{A.7}$$

In particular, if we let $g(t) = t$ in (A.4), then (A.7) yields $t\delta'(t) = -\delta(t)$; not just zero as one might have naïvely expected. An alert reader may have noticed that in the derivation of (A.7), we never used the assumption that $g(t)$ is a polynomial; all that the derivation required was $g(t)\phi(t) \in S$. While it is definitely true that $g(t)\phi(t) \in S$ when $g(t)$ is a polynomial, requiring $g(t)$ to be a polynomial is an unnecessary restriction. In other words, (A.7) holds for any function $g(t)$ as long as $g(t)\phi(t) \in S$. For example, $g(t)$ could be $\sin(t)$, but it cannot be $\exp(t^4)$ because then $g(t)\phi(t) \notin S$ and the integrated terms will not vanish. We considered this example in such detail because we will have numerous opportunities to

use (A.7) in appendix A.1.2.

A.1.1 The Fourier transform of tempered distributions

The key idea in generalizing the notation of a derivative is to move the derivative from a function (generalized function) onto a set of ‘good’ functions, namely, $\phi(t) \in S$. Moreover, we saw that by integrating by parts enough times, every (generalized) function had a derivative, because the space S is composed of classically infinitely differentiable functions. We will use this ‘moving idea’ (adjoint operator) to *define* the Fourier transform of a tempered distribution $f(t)$. By the Fourier transform of $f(t) \in S'$, denoted by $\tilde{f}(\omega)$ or by $\mathcal{F}[f(t)]$, we mean

$$\langle \mathcal{F}[f(t)], \phi(\omega) \rangle = \langle f(t), \mathcal{F}[\phi(\omega)] \rangle, \quad (\text{A.8})$$

where

$$\langle f(t), \mathcal{F}[\phi(\omega)] \rangle = \int_{-\infty}^{\infty} f(t) \left(\int_{-\infty}^{\infty} \phi(\omega) e^{+i\omega t} d\omega \right) dt. \quad (\text{A.9})$$

By the inverse Fourier transform of $\tilde{f}(\omega)$, denoted by $\mathcal{F}^{-1}[\tilde{f}(\omega)]$, we mean

$$\langle \mathcal{F}^{-1}[\tilde{f}(\omega)], \tilde{\phi}(t) \rangle = \langle \tilde{f}(\omega), \mathcal{F}^{-1}[\tilde{\phi}(t)] \rangle, \quad (\text{A.10})$$

where

$$\langle \tilde{f}(\omega), \mathcal{F}^{-1}[\tilde{\phi}(t)] \rangle = \int_{-\infty}^{\infty} \tilde{f}(\omega) \left(\frac{1}{2\pi} \int_{-\infty}^{\infty} \tilde{\phi}(t) e^{-i\omega t} dt \right) d\omega. \quad (\text{A.11})$$

By changing the order of integration in (A.9) and (A.11), we see that (A.9) and (A.11) are indeed consistent with the classical Fourier transform pair. The underlining reason for defining the Fourier transform pair by (A.8) and (A.10) lies in the fact that if $\phi \in S$ then $\tilde{\phi}$ is also in S ; the converse is also true. Moreover, it can be shown that $f \in S'$ if and only if $\tilde{f} \in S'$. For a proof of these and related matters, see [21, chapter 3], [24, chapter 6], [25, chapter 7] and [26, chapter 2]. Now, we will make (A.8)–(A.11) more concrete by considering a few simple examples.

For our first example, we will compute the generalized Fourier transform of $\delta(t)$, i.e. $\langle \mathcal{F}[\delta(t)], \phi(\omega) \rangle$. Substituting $\delta(t)$ into (A.9) and changing the order of integration yields

$$\int_{-\infty}^{\infty} \phi(\omega) \left(\int_{-\infty}^{\infty} \delta(t) e^{+i\omega t} dt \right) d\omega = \int_{-\infty}^{\infty} \phi(\omega) d\omega = \langle 1, \phi(\omega) \rangle. \quad (\text{A.12})$$

Thus, we see that $\mathcal{F}[\delta(t)] = 1$. Moreover, by taking the inverse Fourier transform, we obtain the famous integral representation of the Dirac delta function, namely,

$$\delta(t) = \frac{1}{2\pi} \int_{-\infty}^{\infty} e^{-i\omega t} d\omega. \quad (\text{A.13})$$

It's worth stressing that (A.13) should be interpreted in a distribution sense and, strictly speaking, writing (A.13) as we did is an abuse of notation. However, such abuses of notation are very common in physics; e.g., see the famous graduate electrodynamics textbook [27].

As another simple example, consider the generalized inverse Fourier transform of $2\pi\tilde{\delta}(\omega - \omega_0)$, where ω_0 is a real number; i.e. $\langle \mathcal{F}^{-1}[2\pi\tilde{\delta}(\omega - \omega_0)], \tilde{\phi}(t) \rangle$ when $\omega_0 \in \mathbb{R}$. Substituting $2\pi\tilde{\delta}(\omega - \omega_0)$ into (A.11), then changing the order of integration and integrating over ω yields

$$\int_{-\infty}^{\infty} \tilde{\phi}(t) e^{-i\omega_0 t} dt = \langle e^{-i\omega_0 t}, \tilde{\phi}(t) \rangle. \quad (\text{A.14})$$

Thus, we see that $\mathcal{F}^{-1}[\tilde{\delta}(\omega - \omega_0)] = \exp(-i\omega_0 t)$.

For our last example, let us compute the Fourier transform of the n th generalized derivative of $f(t) \in S'$. From (A.8), we have

$$\left\langle \mathcal{F} \left[\frac{d^n}{dt^n} f(t) \right], \phi(\omega) \right\rangle = \int_{-\infty}^{\infty} \left(\frac{d^n}{dt^n} f(t) \right) \tilde{\phi}(t) dt. \quad (\text{A.15})$$

Performing integration by parts n -times on the right-hand side (where the integrated terms vanished because $\tilde{\phi} \in S$), yields

$$\begin{aligned} (-1)^n \int_{-\infty}^{\infty} f(t) \left(\frac{d^n}{dt^n} \tilde{\phi}(t) \right) dt &= (-1)^n \int_{-\infty}^{\infty} f(t) \mathcal{F}[(+i\omega)^n \phi(\omega)] dt \\ &= \int_{-\infty}^{\infty} \mathcal{F}[f(t)] (-i\omega)^n \phi(\omega) d\omega, \end{aligned} \quad (\text{A.16})$$

where we obtained (A.16) by using the definition (A.8). Finally, comparing (A.16) with the left-hand side of (A.15) yields

$$\mathcal{F} \left[\frac{d^n}{dt^n} f(t) \right] = (-i\omega)^n \mathcal{F} [f(t)]. \quad (\text{A.17})$$

Notice that in this example, we have used the definition (A.8) *twice*; Strichartz [21, pp. 49–50] appropriately refers to this as ‘definition chasing’.

No discussion of the Fourier transform of tempered distributions would be complete without the Fourier transform of a convolution integral. For our purposes, it will be sufficient to only consider convolution of the tempered distribution f with a fixed element ψ from the space of ‘good’ functions. Let $f \in S'$ and $\psi \in S$; then, by the convolution of f with ψ , denoted by $(f * \psi)(t)$, we mean

$$(f * \psi)(t) = \int_{-\infty}^{\infty} f(t - t') \psi(t') dt'. \quad (\text{A.18})$$

By a simple change of variables, we see that convolution is commutative, i.e. $(f * \psi)(t) = (\psi * f)(t)$. Convolution defines an infinitely differentiable function and thus can be viewed as a ‘smoothing’ process. To see this, let $h(t) = (f * \psi)(t)$ then

$$\frac{d^n}{dt^n} h(t) = \frac{d^n}{dt^n} [(f * \psi)(t)] = \int_{-\infty}^{\infty} \left(\frac{d^n}{dt^n} f(t - t') \right) \psi(t') dt' \quad (\text{A.19})$$

$$= \frac{d^n}{dt^n} [(\psi * f)(t)] = \int_{-\infty}^{\infty} \left(\frac{d^n}{dt^n} \psi(t - t') \right) f(t') dt'. \quad (\text{A.20})$$

From (A.20), we conclude that all derivatives of $h(t)$ exist in the classical sense because $\psi \in S$, and from (A.19) we see that it doesn’t matter how ‘rough’ (e.g., $\delta'(t)$ is ‘rougher’ than $\delta(t)$) the distribution is. In passing, we note another useful property of (A.18), namely that its Fourier transform corresponds to multiplication in the Fourier-domain, i.e.

$$\langle \mathcal{F}[(\psi * f)(t)], \phi(\omega) \rangle = \langle \tilde{\psi}(\omega) \tilde{f}(\omega), \phi(\omega) \rangle. \quad (\text{A.21})$$

A.1.2 Support and structure of tempered distributions

We often want to speak about the local properties of distributions as if the distributions were ordinary (classical) functions. When speaking about an ordinary function $f(t)$, the statement ‘ $f(t)$ has a value of $f(t_1)$ when $t = t_1$ ’ has meaning, but the statement is nonsense if $f(t)$ is a distribution.⁹ However, we *can* identify a set of points where distribution f is non-zero. Loosely speaking, this set of points is known as the *support* of f . The formal definition of support requires us to define where a distribution f is zero. We say a distribution $f(t)$ is zero, $f(t) = 0$, on an *open* interval (a, b) if $\langle f(t), \psi(t) \rangle = 0$ for every infinitely differentiable test function $\psi(t)$ that vanishes in a *neighbourhood* of every point *not* in (a, b) interval. For example, if $f(t) = 0$ on $(-1, 1)$, then $\psi(t)$ vanishes *outside* the $(-1+\epsilon, 1-\epsilon)$ interval for some $\epsilon > 0$. We now formally define the support of a distribution $f(t)$, denoted by $\text{supp}[f(t)]$, as the *complement* of the set of points t such that $f(t) = 0$ in a *neighbourhood* of t . For example, if $f(t) = 0$ on $(-\infty, \infty)$, then $\text{supp}[f(t)]$ is the empty set and, as a less trivial example, $\text{supp}[\delta(t)] = \{0\}$. Moreover, we will show that

$$\text{supp}\left[\frac{d^n}{dt^n}\delta(t)\right] = \{0\}. \quad (\text{A.22})$$

Consider any open interval I_1 that does *not* contain the point $t = 0$; then,

$$\left\langle \frac{d^n}{dt^n}\delta(t), \psi(t) \right\rangle = (-1)^n \left\langle \delta(t), \frac{d^n}{dt^n}\psi(t) \right\rangle = (-1)^n \frac{d^n}{dt^n}\psi(0) = 0$$

because $\psi(t)$ vanishes in a *neighbourhood* of $t = 0$. Of course, for any open interval I_2 that *does* contain the point $t = 0$, the derivatives of ψ don’t vanish at the point $t = 0$ for every test function ψ . Thus, we see that all derivatives of $\delta(t)$ have the same point-support.

The above discussion was necessary to understand the following ‘structure’ theorem. A tempered distribution $f(t)$ with $\text{supp}[f(t)] = \{t_0\}$ must be of the form [21, pp. 82–88]

$$f(t) = \sum_{n=0}^N c_n \frac{d^n}{dt^n}\delta(t - t_0), \quad (\text{A.23})$$

⁹Recall that we have defined distributions only by their action on the space of test functions.

where the coefficients $c_{n=0,\dots,N}$ are complex numbers, i.e. $c_n \in \mathbb{C}$ for $n = 0, \dots, N$. In other words, any tempered distribution with a point-support may be expressed as a *finite* linear combination of the Dirac function and its derivatives; this is a powerful statement! In the next paragraph, we will show how we can use (A.23) to solve ‘algebraic’ equations in a distributional sense. These types of equations are frequently encountered when we solve differential equations by the Fourier transform technique.

As our first example, consider the following equation,

$$\langle (t - t_0) f(t), \phi(t) \rangle = \langle 1, \phi(t) \rangle, \quad (\text{A.24})$$

for all $\phi(t) \in S$. Before we find the unknown tempered distribution $f(t)$, we note that it is customary to abuse the notation and write (A.24) simply as

$$(t - t_0) f(t) = 1. \quad (\text{A.25})$$

Naively, we might expect that

$$f_p(t) = \frac{1}{t - t_0}, \quad (\text{A.26})$$

would solve (A.25), but this is only the particular part of the solution. We could have a tempered distribution $f_h(t)$ with $\text{supp}[f_h(t)] = \{t_0\}$ such that $(t - t_0)f_h(t) = 0$, and therefore, $f(t) = f_p(t) + f_h(t)$ would also satisfy (A.25). We refer to $f_h(t)$ as the homogeneous solution and, in light of the structure theorem in the previous paragraph, we know it must be of the form

$$f_h(t) = \sum_{n=0}^N c_n \frac{d^n}{dt^n} \delta(t - t_0). \quad (\text{A.27})$$

Substituting (A.27) into $\langle (t - t_0)f_h(t), \phi(t) \rangle = \langle 0, \phi(t) \rangle$ and integrating by parts until the derivatives only appear on ϕ yields

$$-c_1 \phi(t_0) + 2c_2 \phi'(t_0) - 3c_3 \phi''(t_0) + \dots + (-1)^N N c_N \phi^{(N-1)}(t_0) = 0.$$

The above equation must hold for all $\phi \in S$. Thus, the coefficients must vanish independently, i.e. $c_n = 0$ for $n = 1, 2, \dots, N$. Therefore, the homogeneous solution is given by

$$f_h(t) = c_0 \delta(t - t_0), \quad (\text{A.28})$$

and the full solution to (A.25) (or more formally, to (A.24)) is given by

$$f(t) = \frac{1}{t - t_0} + c_0 \delta(t - t_0). \quad (\text{A.29})$$

Loosely speaking, from (A.29) we see that we can divide by zero, provided we add an appropriate tempered distribution with a point-support. In general, using the same procedure as above, we can show that the distributional solution to $(t - t_0)^n f(t) = 1$ is given by $f(t) = f_p(t) + f_h(t)$, where

$$f_p(t) = \frac{1}{(t - t_0)^n}, \quad (\text{A.30})$$

$$f_h(t) = c_0 \delta(t - t_0) + c_1 \delta'(t - t_0) + \dots + c_{n-1} \delta^{(n-1)}(t - t_0). \quad (\text{A.31})$$

For our second and last example, consider (in a distributional sense, of course) the following equation,

$$(t - t_1)(t - t_2)f(t) = 1, \quad (\text{A.32})$$

where $t_1 \neq t_2$. From our previous example, we expect the solution to be of the form

$$f(t) = \frac{1}{(t - t_1)(t - t_2)} + \sum_{n=0}^N b_n \delta^{(n)}(t - t_1) + \sum_{m=0}^M c_m \delta^{(m)}(t - t_2). \quad (\text{A.33})$$

Substituting (A.33) into (A.32) (of course, we actually mean $\langle (t - t_1)(t - t_2)f(t), \phi(t) \rangle = \langle 1, \phi(t) \rangle$, for all $\phi \in S$) and integrating by parts until the derivatives only appear on ϕ yields

$$\begin{aligned} \sum_{n=1}^N (-1)^n b_n [n(n-1)\phi^{(n-2)}(t_1) + n(t_1 - t_2)\phi^{(n-1)}(t_1)] \\ + \sum_{m=1}^M (-1)^m c_m [m(m-1)\phi^{(m-2)}(t_2) - m(t_1 - t_2)\phi^{(m-1)}(t_2)] = 0. \end{aligned} \quad (\text{A.34})$$

From (A.34), we see that $b_n = 0$ for $n = 1, \dots, N$ and $c_m = 0$ for $m = 1, \dots, M$. Therefore, the full solution to (A.32) is given by $f(t) = f_p(t) + f_h(t)$, where

$$f_p(t) = \frac{1}{(t - t_1)(t - t_2)}, \quad (\text{A.35})$$

$$f_h(t) = b_0 \delta(t - t_1) + c_0 \delta(t - t_2). \quad (\text{A.36})$$

Notice that if $t_1 = t_2$ then (A.36) does *not* yield the correct solution, which is given by (A.31) (with $n = 2$ and $t_1 = t_2 \rightarrow t_0$). The reason for this ‘discrepancy’ is because our conclusion from (A.34), namely, that $b_{n=1,\dots,N} = 0$ and $c_{m=1,\dots,M} = 0$, is *not* valid if $t_1 = t_2$. In other words, we must be very careful when dealing with distributional solutions in limiting cases such as $t_2 \rightarrow t_1$. In the body of the paper, these limiting cases arise when we consider vanishing absorption.

CHAPTER 4

MEASURING THE VOID: THEORETICAL STUDY OF SCATTERING BY A CYLINDRICAL ANNULUS

A paper published in the *Journal of Quantitative Spectroscopy & Radiative Transfer*.

Alex J. Yuffa^{*}, John A. Scales

Department of Physics, Colorado School of Mines, Golden, CO 80401, USA

^{*}Primary researcher and author. E-mail: ayuffa@gmail.com

4.1 Abstract

In this paper, we analyze a monochromatic plane wave scattering from an infinite homogeneous cylindrical annulus. In particular, we study the effect that the inner part of the cylindrical annulus (cylindrical void, if you will) has on the scattered field. This is done by isolating the cylindrical void’s contribution to the scattered field. We show that if the cylindrical void is small, then its contribution to the scattered field may be approximated by the “screened cylindrical void” (SCV) approximation. We first develop the SCV approximation in a physically intuitive manner, and then show that it could also be obtained in a more mathematically rigorous manner. Numerical results comparing the SCV approximation to the exact solution are also presented.

4.2 Introduction

Consider a monochromatic plane wave scattering from an infinitely long homogeneous and isotropic cylindrical annulus with outer radius r_1 and inner radius r_2 , see Figure 4.1(a). Let ϵ_1 denote the permittivity of the space surrounding the cylindrical annulus and let ϵ_2 denote the permittivity of the cylindrical annulus itself, $r_2 < r < r_1$. Let us refer to the region of space inside the cylindrical annulus as the “cylindrical void” and ask what effect

the cylindrical void has on the scattered field(s) outside the cylindrical annulus. If one were to *experimentally* investigate this, one would do the following:

- (a) measure the total field $V^{(1)}(r, \theta)$ outside the cylindrical annulus ($r > r_1$);
- (b) measure the total field $U^{(1)}(r, \theta)$ outside an identical “host cylinder;” i.e., a cylinder of radius r_1 and permittivity ϵ_2 , as illustrated in Figure 4.1(b);
- (c) compute the difference between the two fields in (a) and (b):

$$W^{(\text{sca})}(r, \theta) = V^{(1)}(r, \theta) - U^{(1)}(r, \theta). \quad (4.1)$$

Following the above procedure, $W^{(\text{sca})}(r, \theta)$ contains the effect that the cylindrical void had on the scattered field. In this paper, we show that $W^{(\text{sca})}(r, \theta)$ can be approximated by the scattered field produced by the cylindrical void when a plane wave from a region of space with a permittivity of ϵ_2 is incident on it. This approximation holds if the “screening effect” (discussed in Section 4.3) of the cylindrical annulus is properly accounted for, and if the cylindrical void is sufficiently small. We refer to this approximation as the *screened cylindrical void* (SCV) approximation. Furthermore, we investigate the rate, denoted by \mathbb{W}^{ext} , at which the energy is extinguished (depleted) by the cylindrical void from the total field outside, $U^{(1)}(r, \theta)$, the host cylinder.

To the best of our knowledge, the SCV approximation and its physical interpretation (see Section 4.3) has not been previously considered in the literature. In order to make the paper accessible to the widest possible scientific community, we use the well-known Lorenz–Mie theory [1–4] to derive the SCV approximation. However, we do note that our intuitive derivation of the SCV approximation, which is presented in Section 4.3, is *physically guided* by the Debye series expansion [5]. In short, the Debye series expansion consists of re-expressing *each* Mie scattering coefficient in terms of an infinite series called the Debye series. Each term in the Debye series may be physically interpreted in terms of the number

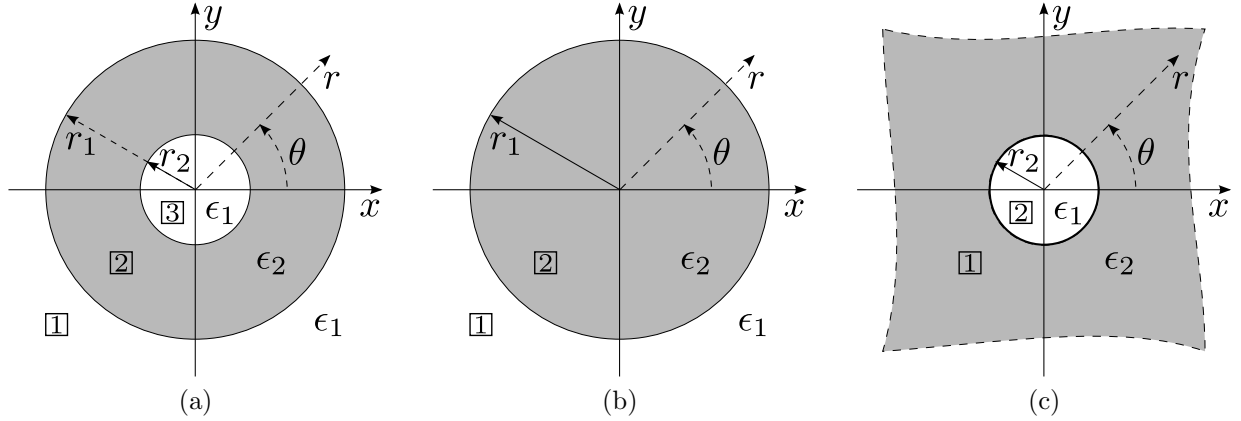


Figure 4.1: The cross-sectional view of the cylindrical scattering objects is shown. The origin of the coordinate system (r, θ) , where $-\pi \leq \theta < \pi$, is concentric with the cylindrical objects. In each panel, the region is denoted by a boxed number and the permittivity of each region is also indicated. For example, region three, $r < r_2$, in panel (a) has a permittivity of ϵ_1 and region one, $r > r_2$, in panel (c) has a permittivity of ϵ_2 .

of reverberations the wave has experienced. A reader interested in the use of the Debye series expansion in the context related to this paper, namely, plane wave scattering by a multilayered cylinder, may consult [6, 7] and references therein.

Although we do not explicitly consider many diverse areas of science where the scattering by a cylindrical void is important (e.g., see [3, 4]), we would like to mention one, namely, localization. Fifty years after the publication of Anderson's seminal work [8], localization continues to be a thriving area of research [9] in theoretical and experimental physics. Localization of millimeter/submillimeter electromagnetic waves is particularly interesting because both the amplitude and the phase of the electromagnetic field can be easily measured with a vector network analyzer [10]. At these wavelengths, the preparation of disordered samples is also inexpensive and straightforward with standard computer-numerically-controlled (CNC) milling techniques. A sample may be prepared by drilling small holes in a large Teflon (ultra low-loss material) cylinder. Further, by illuminating the sample from the side and putting it on a rotational stage, we can generate essentially arbitrary realizations of the same random disorder. When the number of small scatterers is large, say, over 1000, then what is impor-

tant is the rate at which the scatterer extinguishes the energy from the incident field, rather than the geometrical shape/size of each individual scatterer [11, 12]. Thus, the physical insight into scattering by a single small cylindrical void discussed in this paper may be of benefit in understanding the experimental model described above.

Throughout this paper, we will use the Gaussian unit system, and we will assume that all fields are harmonic in time with a $\exp(-i\omega t)$ time factor, where ω is the angular frequency. Furthermore, we will assume that all fields are polarized in the positive $\hat{\mathbf{z}}$ -direction. The positive $\hat{\mathbf{z}}$ -direction is out of the page in Figure 4.1. All media considered in this paper are assumed to be non-magnetic, and ϵ_1 is assumed to be purely real.

4.3 Intuitive derivation of the SCV approximation

In this section, a physically intuitive derivation of the SCV approximation is presented. The derivation is organized as follows. First, we imagine a unit plane wave $u^{(\text{inc})}(r, \theta)$ incident from region one onto the cylindrical void shown in Figure 4.1(c). Then, we compute the scattered field $u^{(\text{sca})}(r, \theta)$ in region one generated by the scattering of $u^{(\text{inc})}(r, \theta)$ from the cylindrical void. Second, to account for the screening effect of the cylindrical annulus, we use the previously found scattered field $u^{(\text{sca})}(r, \theta)$ as the *incident* (primary) field, i.e., $w^{(\text{inc})}(r, \theta) \equiv u^{(\text{sca})}(r, \theta)$, originating from the center of the host cylinder shown in Figure 4.1(b). Finally, we compute the total field $w^{(1)}(r, \theta)$ in region one shown in Figure 4.1(b) and physically interpret the terms contained in it to obtain an approximation to $W^{(\text{sca})}(r, \theta)$, see (4.1).

Let us note that all fields in this paper satisfy the two-dimensional (2D) Helmholtz equation. The radial solution of the 2D Helmholtz equation is composed of a linear combination of integer order Bessel functions of the first and second kind, which we denote by $J_n(\xi)$ and $Y_n(\xi)$, respectively. The Bessel functions $J_n(\xi)$ and $Y_n(\xi)$ also satisfy the Wronskian relationship [13], namely,

$$J_{n+1}(\xi)Y_n(\xi) - J_n(\xi)Y_{n+1}(\xi) = \frac{2}{\pi\xi}. \quad (4.2a)$$

Also, $J_n(\xi)$, $Y_n(\xi)$ and the Hankel function of the first kind, which we denote by $H_n(\xi) = J_n(\xi) + iY_n(\xi)$, satisfy the recurrence relation [13],

$$\frac{d}{d\xi}\Psi_n(\xi) = \frac{n}{\xi}\Psi_n(\xi) - \Psi_{n+1}(\xi), \quad (4.2b)$$

where Ψ denotes J , Y or H . Lastly, we note the Jacobi–Anger expansion of a plane wave [13], namely,

$$e^{i\xi \cos \theta} = \sum_{n=0}^{\infty} g_n i^n J_n(\xi) \cos(n\theta), \quad (4.2c)$$

where g_n denotes the Neumann factor: $g_0 = 1$ and $g_n = 2$ for $n \geq 1$.

Returning to the scattering of the unit plane wave from the cylindrical void shown in Figure 4.1(c), let the incident wave be $u^{(\text{inc})}(r, \theta) = \exp(ik_2 r \cos \theta)$, where $k_2 = \sqrt{\epsilon_2} \omega / c$ is the wavenumber and c is the speed of light in a vacuum. Then, the field in region two $u^{(2)}(r, \theta)$, and the total field in region one decomposed as $u^{(1)}(r, \theta) = u^{(\text{inc})}(r, \theta) + u^{(\text{sca})}(r, \theta)$, may be written as

$$\begin{bmatrix} u^{(\text{inc})}(r, \theta) \\ u^{(\text{sca})}(r, \theta) \\ u^{(2)}(r, \theta) \end{bmatrix} = \sum_{n=0}^{\infty} g_n i^n \begin{bmatrix} J_n(k_2 r) \\ \delta_n H_n(k_2 r) \\ \gamma_n J_n(k_1 r) \end{bmatrix} \cos(n\theta), \quad (4.3)$$

where $k_1 = \sqrt{\epsilon_1} \omega / c$. In writing (4.3), we used the Jacobi–Anger expansion (4.2c) to rewrite $\exp(ik_2 r \cos \theta)$ as an infinite sum, imposed the Sommerfeld radiation (*outgoing* cylindrical wave) condition on $u^{(\text{sca})}(r, \theta)$, and required $u^{(2)}(r, \theta)$ to be regular (finite) at $r = 0$. To find the unknown coefficients in (4.3), we require that the electric field and its normal derivative be continuous across the $r = r_2$ interface, i.e.,

$$u^{(1)} = u^{(2)} \quad \text{and} \quad \frac{\partial}{\partial r} u^{(1)} = \frac{\partial}{\partial r} u^{(2)} \quad \text{on } r = r_2, \quad (4.4)$$

to obtain a system of linear equations. Solving this system of linear equations for δ_n and using (4.2b) to simplify the result, yields

$$\delta_n = -\frac{J_{n+1}(k_1 r_2) J_n(k_2 r_2) - \kappa J_n(k_1 r_2) J_{n+1}(k_2 r_2)}{J_{n+1}(k_1 r_2) H_n(k_2 r_2) - \kappa J_n(k_1 r_2) H_{n+1}(k_2 r_2)}, \quad (4.5a)$$

where $\kappa = k_2/k_1$, $n \in \mathbb{Z}^+$, and \mathbb{Z}^+ denotes the set of all nonnegative integers. It is convenient to introduce curly bracket notation, $\{\Psi_{n+1}(\xi); \Phi(\eta)\}$, by which we mean

$$\{\Psi_{n+1}(\xi); \Phi(\eta)\} \equiv (\Psi_{n+1}(\xi)\Phi(\eta) - \kappa\Psi_n(\xi)\Phi_{n+1}(\eta)).$$

For example, (4.5a) in the curly bracket notation reads as

$$\delta_n = -\frac{\{J_{n+1}(k_1 r_2); J_n(k_2 r_2)\}}{\{J_{n+1}(k_1 r_2); H_n(k_2 r_2)\}}, \quad n \in \mathbb{Z}^+. \quad (4.5b)$$

Having found the expansion coefficients of the scattered wave $u^{(\text{sca})}(r, \theta)$, we are now ready to see how they should be modified in order to account for the screening effect of the cylindrical annulus.

Imagine a “line-source” embedded in the center of the host cylinder shown in Figure 4.1(b). We take the field produced by the line-source to be equal to $u^{(\text{sca})}(r, \theta)$ in (4.3). If we use this field as the incident field, i.e., $w^{(\text{inc})}(r, \theta) \equiv u^{(\text{sca})}(r, \theta)$, then the total field $w^{(2)}(r, \theta)$ *inside* the host cylinder (region two in Figure 4.1(b)) may be written as $w^{(2)}(r, \theta) = w^{(\text{inc})}(r, \theta) + w^{(\text{sca})}(r, \theta)$, where

$$w^{(\text{sca})}(r, \theta) = \sum_{n=0}^{\infty} g_n i^n \beta_n J_n(k_2 r) \cos(n\theta). \quad (4.6a)$$

Notice that in (4.6a), we required $w^{(\text{sca})}(r, \theta)$ to be regular at $r = 0$. This requirement is necessary because we are essentially treating the cylindrical void as a line-source in this paragraph. The field *outside* the host cylinder (region one in Figure 4.1(b)), $w^{(1)}(r, \theta)$, must satisfy the Sommerfeld radiation condition and thus, it is given by

$$w^{(1)}(r, \theta) = \sum_{n=0}^{\infty} g_n i^n \alpha_n H_n(k_1 r) \cos(n\theta). \quad (4.6b)$$

Imposing the boundary conditions $w^{(1)} = w^{(2)}$ and $(\partial/\partial r) w^{(1)} = (\partial/\partial r) w^{(2)}$ on $r = r_1$, then solving the resultant linear system for α_n and using (4.2a) with (4.2b) to simplify the result yields

$$\alpha_n = \left(\frac{-2i}{\pi k_1 r_1 \{H_{n+1}(k_1 r_1); J_n(k_2 r_1)\}} \right) \delta_n, \quad n \in \mathbb{Z}^+. \quad (4.7)$$

We physically interpret the term in parentheses in (4.7) as the screening effect of the cylindrical annulus on the scattered wave generated by the cylindrical void. The α_n coefficients are not quite the correct ones to use in $W^{(\text{sca})}(r, \theta)$ because they do *not* contain the screening effect that the cylindrical annulus had on the *incident* wave. A moment's thought reveals that this screening effect had to be the same as the screening effect on the scattered wave. Thus, the $W^{(\text{sca})}(r, \theta)$ expansion coefficients should be given by (4.7) with the parenthesis term *squared*. Therefore, $W^{(\text{sca})}(r, \theta)$ is approximately given by

$$W^{(\text{sca})}(r, \theta) \cong \sum_{n=0}^{\infty} g_n i^n \left(\frac{-2i}{\pi k_1 r_1 \{H_{n+1}(k_1 r_1); J_n(k_2 r_1)\}} \right)^2 \delta_n H_n(k_1 r) \cos(n\theta), \quad (4.8)$$

where the δ_n coefficients are given by (4.5).

4.4 Rigorous derivation of the SCV approximation

In this section, we present a rigorous derivation of $W^{(\text{sca})}(r, \theta)$ by directly computing $U^{(1)}(r, \theta)$ and $V^{(1)}(r, \theta)$ (recall the bullet list of Section 4.2). Once the *exact* $W^{(\text{sca})}(r, \theta)$ is found, we show that it is approximately equal to (4.8) if $k_1 r_2 \ll 1$ and $|k_2| r_2 \ll 1$. Furthermore, a numerical illustration of the SCV approximation is also presented.

If a plane wave, $U^{(\text{inc})}(r, \theta) = \exp(ik_1 r \cos \theta)$, is incident on the host cylinder shown in Figure 4.1(b), then by proceeding as in paragraph three of Section 4.3, the total field in region one is $U^{(1)}(r, \theta) = U^{(\text{inc})}(r, \theta) + U^{(\text{sca})}(r, \theta)$, where the scattered field is

$$U^{(\text{sca})}(r, \theta) = \sum_{n=0}^{\infty} g_n i^n A_n^{(\text{hc})} H_n(k_1 r) \cos(n\theta) \quad (4.9a)$$

with

$$A_n^{(\text{hc})} = -\frac{\{J_{n+1}(k_1 r_1); J_n(k_2 r_1)\}}{\{H_{n+1}(k_1 r_1); J_n(k_2 r_1)\}}, \quad n \in \mathbb{Z}^+, \quad (4.9b)$$

and the field in region two is given by

$$U^{(2)}(r, \theta) = \sum_{n=0}^{\infty} g_n i^n B_n^{(\text{hc})} J_n(k_2 r) \cos(n\theta). \quad (4.9c)$$

The superscript (hc) on the expansion coefficients in (4.9) is meant to remind the reader that these expansion coefficients are for the *host* cylinder.

Turning our attention to the cylindrical annulus shown in Figure 4.1(a), if we think of the cylindrical annulus as the host cylinder into which a scatterer, namely, the cylindrical void, has been inserted, then, the total fields in regions one, two, and three may be written as $V^{(1)}(r, \theta) = U^{(1)}(r, \theta) + W^{(\text{sca})}(r, \theta)$, $V^{(2)}(r, \theta) = U^{(2)}(r, \theta) + W^{(2)}(r, \theta)$ and $V^{(3)}(r, \theta) = W^{(3)}(r, \theta)$, respectively. Noting that the W -fields also satisfy the 2D Helmholtz equation and imposing the Sommerfeld radiation condition on $W^{(\text{sca})}(r, \theta)$, as well as requiring $W^{(3)}(r, \theta)$ to be regular at $r = 0$, yields

$$\begin{bmatrix} W^{(\text{sca})}(r, \theta) \\ W^{(2)}(r, \theta) \\ W^{(3)}(r, \theta) \end{bmatrix} = \sum_{n=0}^{\infty} g_n i^n \begin{bmatrix} A_n^{(\text{cv})} H_n(k_1 r) \\ B_n^{(\text{cv})} J_n(k_2 r) + C_n^{(\text{cv})} Y_n(k_2 r) \\ D_n^{(\text{cv})} J_n(k_1 r) \end{bmatrix} \cos(n\theta). \quad (4.10)$$

The superscript (cv) on the expansion coefficients in (4.10) reminds us of the presence of the *cylindrical void*. To find the unknown coefficients in (4.10), we require that the V -fields and their normal derivatives be continuous across the $r = r_1$ interface, as well as the $r = r_2$ interface to obtain

$$\underbrace{\begin{bmatrix} -H_n(k_1 r_1) & J_n(k_2 r_1) & Y_n(k_2 r_1) & 0 \\ -H'_n(k_1 r_1) & \kappa J'_n(k_2 r_1) & \kappa Y'_n(k_2 r_1) & 0 \\ 0 & J_n(k_2 r_2) & Y_n(k_2 r_2) & -J_n(k_1 r_2) \\ 0 & \kappa J'_n(k_2 r_2) & \kappa Y'_n(k_2 r_2) & -J'_n(k_1 r_2) \end{bmatrix}}_{=M} \begin{bmatrix} A_n^{(\text{cv})} \\ B_n^{(\text{cv})} \\ C_n^{(\text{cv})} \\ D_n^{(\text{cv})} \end{bmatrix} = \begin{bmatrix} J_n(k_1 r_1) + A_n^{(\text{hc})} H_n(k_1 r_1) - B_n^{(\text{hc})} J_n(k_2 r_1) \\ J'_n(k_1 r_1) + A_n^{(\text{hc})} H'_n(k_1 r_1) - \kappa B_n^{(\text{hc})} J'_n(k_2 r_1) \\ -B_n^{(\text{hc})} J_n(k_2 r_2) \\ -\kappa B_n^{(\text{hc})} J'_n(k_2 r_2) \end{bmatrix}, \quad (4.11)$$

and the prime denotes the derivative with respect to the argument. Solving (4.11) for $A_n^{(\text{cv})}$ and using (4.2b) to simplify the result, yields

$$\begin{aligned} \det(M) A_n^{(\text{cv})} &= -\{J_{n+1}(k_1 r_2); J_n(k_2 r_2)\} \\ &\quad \times (A_n^{(\text{hc})} \{H_{n+1}(k_1 r_1); Y_n(k_2 r_1)\} + \{J_{n+1}(k_1 r_1); Y_n(k_2 r_1)\}), \end{aligned} \quad (4.12a)$$

where

$$\begin{aligned} \det(M) = & \{H_{n+1}(k_1 r_1); Y_n(k_2 r_1)\} \{J_{n+1}(k_1 r_2); J_n(k_2 r_2)\} \\ & - \{H_{n+1}(k_1 r_1); J_n(k_2 r_1)\} \{J_{n+1}(k_1 r_2); Y_n(k_2 r_2)\}. \end{aligned} \quad (4.12b)$$

To simplify (4.12a) further, we use (4.9b) and note that

$$\begin{aligned} & \{Y_{n+1}(k_1 r_1); Y_n(k_2 r_1)\} \{J_{n+1}(k_1 r_1); J_n(k_2 r_1)\} \\ & - \{Y_{n+1}(k_1 r_1); J_n(k_2 r_1)\} \{J_{n+1}(k_1 r_1); Y_n(k_2 r_1)\} = \left(\frac{2}{\pi k_1 r_1}\right)^2 \end{aligned}$$

to obtain

$$A_n^{(\text{cv})} = \frac{i}{\det(M)} \left(\frac{2}{\pi k_1 r_1}\right)^2 \frac{\{J_{n+1}(k_1 r_2); J_n(k_2 r_2)\}}{\{H_{n+1}(k_1 r_1); J_n(k_2 r_1)\}}, \quad n \in \mathbb{Z}^+. \quad (4.13)$$

The $A_n^{(\text{cv})}$ coefficients in (4.13) are the *exact* expansion coefficients of $W^{(\text{sca})}(r, \theta)$. To obtain the approximate coefficients, we first note that $Y_n(k_2 r_2) \sim -iH_n(k_2 r_2)$ if $|k_2| r_2 \ll 1$ [13], which allows us to rewrite (4.13) as

$$\begin{aligned} A_n^{(\text{cv})} \cong & i \left(\frac{2}{\pi k_1 r_1}\right)^2 \frac{1}{\{H_{n+1}(k_1 r_1); J_n(k_2 r_1)\}} \\ & \times \left(\frac{\delta_n}{\{H_{n+1}(k_1 r_1); Y_n(k_2 r_1)\} \delta_n - i \{H_{n+1}(k_1 r_1); J_n(k_2 r_1)\}} \right), \end{aligned} \quad (4.14)$$

where δ_n is given by (4.5). To develop (4.14) further, we note that $|\delta_n| \ll 1$ if $k_1 r_2 \ll 1$ and $|k_2| r_2 \ll 1$, as can be seen from the small argument forms of $J_n(\xi)$ and $H_n(\xi)$ [13]. Therefore, we can expand (4.14) in powers of δ_n to finally obtain

$$A_n^{(\text{cv})} \approx \left(\frac{2i}{\pi k_1 r_1 \{H_{n+1}(k_1 r_1); J_n(k_2 r_1)\}} \right)^2 \delta_n, \quad n \in \mathbb{Z}^+. \quad (4.15)$$

Notice that the above $A_n^{(\text{cv})}$ coefficients are identical to the expansion coefficients given in (4.8) of Section 4.3.

To numerically illustrate the SCV approximation, the far-field pattern of $W^{(\text{sca})}(r, \theta)$ in the forward direction, $\theta = 0$, as a function of $k_2 r_2$ is show in Figure 4.2. The far-field pattern

of $W^{(\text{sca})}(r, \theta)$ is defined by

$$F(\theta) = - \sum_{n=0}^{\infty} g_n A_n^{(\text{cv})} \cos(n\theta). \quad (4.16)$$

From Figure 4.2, we see that the exact (computed with (4.13)) and the approximate (computed with (4.15)) far-field patterns are in good agreement for small $k_2 r_2$, say, $k_2 r_2 < 0.3$. Also from Figure 4.2, we see that the SCV approximation becomes progressively worse as $k_2 r_2$ approaches unity. This is expected as the SCV approximation requires that both $k_1 r_2$ and $k_2 r_2$ are much smaller than unity.

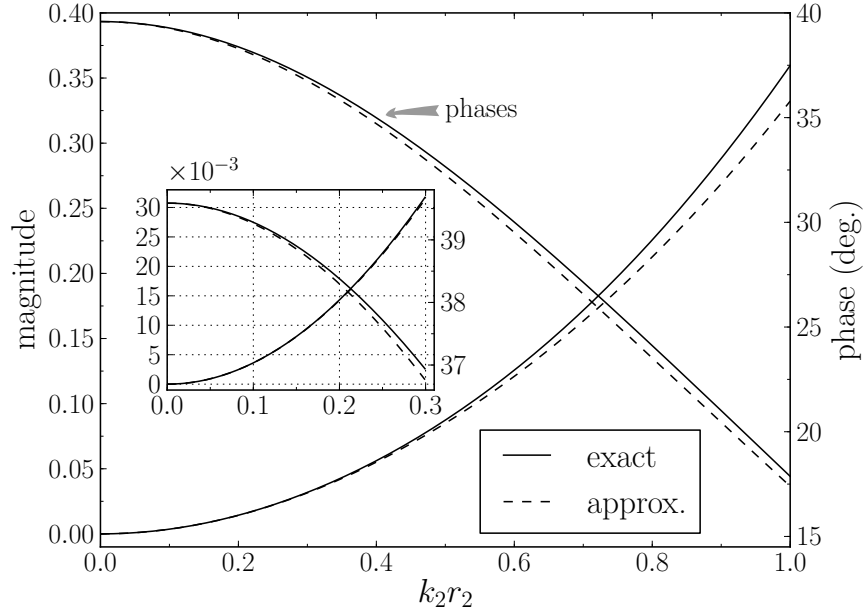


Figure 4.2: The magnitude and phase of the far-field pattern in the forward direction for a Teflon cylindrical annulus in vacuum, with an outer radius of 10 cm at 100 GHz, is shown. The permittivity of Teflon at 100 GHz is 2.05 with a negligible loss-tangent [10]. In the computation of (4.16), we only summed the first $N = \lceil k_1 r_2 + 4(k_1 r_2)^{1/3} + 2 \rceil$ terms [3, Appendix C].

4.5 Energy conservation

In this section, we present a relationship between the rate at which the energy is extinguished by the cylindrical void from the $U^{(1)}(r, \theta)$ field. Also, a numerical example illustrating that the SCV approximation is in good agreement with the derived energy conservation

relationship is presented.

We begin by constructing an imaginary concentric cylinder of radius $R > r_1$ and length L around the host cylinder shown in Figure 4.1(b). Then, the rate $\mathbb{W}_U^{(\text{abs})}$ at which the energy is absorbed within the imaginary concentric cylinder is given by

$$\mathbb{W}_U^{(\text{abs})} = -RL \int_{-\pi}^{\pi} \mathbf{S}_U \cdot \hat{\mathbf{r}} d\theta, \quad (4.17a)$$

where $\hat{\mathbf{r}} = \cos \theta \hat{\mathbf{x}} + \sin \theta \hat{\mathbf{y}}$ (see Figure 4.1), and the time-averaged Poynting vector is given by

$$\mathbf{S}_U = \frac{1}{2} \text{Re} \left[\frac{ic}{4\pi k} U^{(1)} \nabla (U^{(1)})^* \right]. \quad (4.17b)$$

In (4.17b), Re denotes the real part, $*$ denotes the complex conjugate, and $k = \omega/c$. Now, we consider the rate $\mathbb{W}_V^{(\text{abs})}$ at which the energy is absorbed by the *cylindrical annulus*. By proceeding as before, we immediately obtain

$$\mathbb{W}_V^{(\text{abs})} = -RL \int_{-\pi}^{\pi} \mathbf{S}_V \cdot \hat{\mathbf{r}} d\theta, \quad \text{where} \quad \mathbf{S}_V = \frac{1}{2} \text{Re} \left[\frac{ic}{4\pi k} V^{(1)} \nabla (V^{(1)})^* \right]. \quad (4.18)$$

Substituting $V^{(1)} = U^{(1)} + W^{(\text{sca})}$ into (4.18) and using (4.17) to simplify the result yields

$$\mathbb{W}^{\text{ext}} = \mathbb{W}_V^{(\text{abs})} - \mathbb{W}_U^{(\text{abs})} + \mathbb{W}_W^{(\text{sca})}, \quad (4.19a)$$

where

$$\mathbb{W}^{\text{ext}} = -\frac{RLc}{8\pi k} \int_{-\pi}^{\pi} \text{Re} \left[iU^{(1)} \nabla (W^{(\text{sca})})^* + iW^{(\text{sca})} \nabla (U^{(1)})^* \right] \cdot \hat{\mathbf{r}} d\theta, \quad (4.19b)$$

and

$$\mathbb{W}_W^{(\text{sca})} = \frac{RLc}{8\pi k} \int_{-\pi}^{\pi} \text{Re} \left[iW^{(\text{sca})} \nabla (W^{(\text{sca})})^* \right] \cdot \hat{\mathbf{r}} d\theta. \quad (4.19c)$$

We interpret \mathbb{W}^{ext} as the rate at which the energy is extinguished by a scatterer, namely, the cylindrical void, in the presence of the host cylinder. In other words, it is the rate at which the energy is depleted by the cylindrical void from the total field, $U^{(1)}$, outside the host cylinder. Moreover, from (4.19) we see that if the cylindrical annulus is nonabsorbing (ϵ_2 is purely real) then $\mathbb{W}^{\text{ext}} = \mathbb{W}_W^{(\text{sca})}$. Finally, substituting $U^{(1)}(r, \theta)$ and $W^{(\text{sca})}(r, \theta)$ (see

(4.9a) and (4.10)) into (4.19b), and then integrating the result over θ , yields

$$\mathbb{W}^{\text{ext}} = -\frac{Lc}{2\pi k} \sum_{n=0}^{\infty} g_n \left(\text{Re} [A_n^{(\text{cv})}] + 2\text{Re} [A_n^{(\text{cv})} (A_n^{(\text{hc})})^*] \right). \quad (4.20)$$

We interpret the first term in (4.20) as the rate at which $W^{(\text{sca})}$ extinguishes energy from $U^{(\text{inc})}$, and the second term as the rate at which $W^{(\text{sca})}$ extinguishes energy from $U^{(\text{sca})}$.

To illustrate that the SCV approximation is in good agreement with the energy conservation principle, we compute \mathbb{W}^{ext} using the exact and approximate $A_n^{(\text{cv})}$ coefficients. Recall that the exact $A_n^{(\text{cv})}$ coefficients are given by (4.13), and the approximate coefficients by (4.15). The results of the above-mentioned computations are shown in Figure 4.3. From Figure 4.3, we see that the SCV approximation conserves energy to roughly 10 percent for $k_2 r_2 \leq 1$, which does indicate that the SCV approximation is in good agreement with the energy conservation principle.

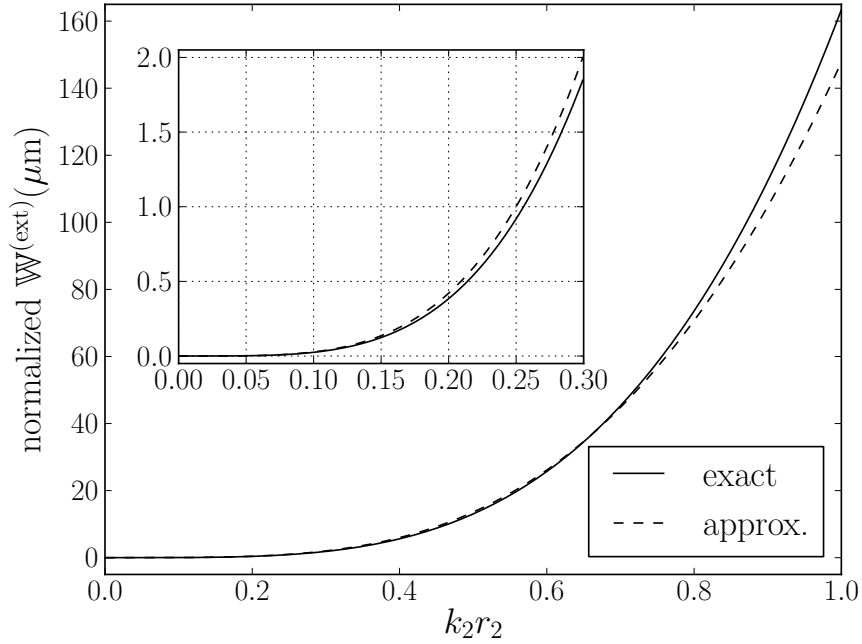


Figure 4.3: The rate \mathbb{W}^{ext} (normalized by $Lc/8\pi$) at which energy is extinguished by the cylindrical void from the total field outside the host cylinder is shown as a function of $k_2 r_2$. The above plot was produced with the same parameters as the ones described in the caption of Figure 4.2.

4.6 Conclusions

In this paper, we investigated a monochromatic plane wave scattering from a solid homogeneous cylinder (host cylinder) and a cylindrical annulus, referring to the inner part of the cylindrical annulus as the cylindrical void. It was shown that if the cylindrical void is thought of as a scatterer inserted into the host cylinder, then the scattered field due to the cylindrical void may be approximated by the screened cylindrical void (SCV) approximation, see Section 4.3. The SCV approximation was derived intuitively in Section 4.3 and rigorously in Section 4.4. Furthermore, a formula for the rate at which energy is depleted by the cylindrical void from the total field outside the host cylinder was derived in Section 4.5. The numerical examples in Sections 4.4 and 4.5 showed that the SCV approximation is in good agreement with the exact solution if the cylindrical void is small.

4.7 Acknowledgment

This material is based upon work supported in part by the U.S. Office of Naval Research as a Multi-disciplinary University Research Initiative on Sound and Electromagnetic Interacting Waves under grant number N00014-10-1-0958.

4.8 References Cited

- [1] M. Kerker, *The Scattering of Light and Other Electromagnetic Radiation*, Academic Press, New York, 1969.
- [2] H. C. van de Hulst, *Light Scattering by Small Particles*, Dover, New York, 1981.
- [3] C. F. Bohren, D. R. Huffman, *Absorption and Scattering of Light by Small Particles*, John Wiley & Sons, New York, 1983.
- [4] G. Gouesbet, Generalized Lorenz-Mie theories, the third decade: A perspective, *J. Quant. Spectrosc. Radiat. Transfer* 110 (2009) 1223–1238.
- [5] P. Debye, Das Elektromagnetische Feld um einen Zylinder und die Theorie des Regenbogens, *Phys. Z.* 9 (1908) 775–778. Reprinted and translated into English in P. L. Marston (Ed.), *Geometrical Aspects of Scattering*, volume MS89 of Milestone Series, SPIE, Bellingham, Wash., 1994, pp. 198–204.

- [6] R. Li, X. Han, H. Jiang, K. F. Ren, Debye series of normally incident plane-wave scattering by an infinite multilayered cylinder, *Appl. Opt.* 45 (2006) 6255–6262.
- [7] R. Li, X. Han, K. F. Ren, Generalized Debye series expansion of electromagnetic plane wave scattering by an infinite multilayered cylinder at oblique incidence, *Phys. Rev. E* 79 (2009) 036602.
- [8] P. W. Anderson, Absence of diffusion in certain random lattices, *Phys. Rev.* 109 (1958) 1492–1505.
- [9] A. Lagendijk, B. van Tiggelen, D. S. Wiersma, Fifty years of Anderson localization, *Physics Today* 62 (2009) 24–29.
- [10] J. A. Scales, L. D. Carr, D. B. McIntosh, V. Freilikher, Y. P. Bliokh, Millimeter wave localization: Slow light and enhanced absorption in random dielectric media, *Phys. Rev. B* 76 (2007) 085118.
- [11] M. Rusek, A. Orłowski, Analytical approach to localization of electromagnetic waves in two-dimensional random media, *Phys. Rev. E* 51 (1995) R2763–R2766.
- [12] M. Rusek, A. Orłowski, Example of self-averaging in three dimensions: Anderson localization of electromagnetic waves in random distributions of pointlike scatterers, *Phys. Rev. E* 56 (1997) 6090–6094.
- [13] M. Abramowitz, I. A. Stegun (Eds.), *Handbook of Mathematical Functions*, Dover, New York, 1965.

CHAPTER 5

SCATTERING FROM A LARGE CYLINDER WITH AN ECCENTRICALLY EMBEDDED CORE: AN ORDERS-OF-SCATTERING APPROXIMATION

A paper submitted to the *Journal of Quantitative Spectroscopy & Radiative Transfer*.

Alex J. Yuffa^{a,*}, Paul A. Martin^b, John A. Scales^a

^a*Department of Physics*

^b*Department of Applied Mathematics and Statistics*

Colorado School of Mines, Golden, CO 80401, USA

*Primary researcher and author. E-mail: ayuffa@gmail.com

5.1 Abstract

We develop an orders-of-scattering approximation, termed the “screened cylindrical void/core” (SCV) approximation, for a composite cylinder. The composite cylinder consists of a large host cylinder that contains a small, eccentrically embedded, core cylinder. The SCV approximation is developed via separation of variables in conjunction with addition theorems for cylindrical functions. We show that the SCV approximation is in good agreement with the numerically-exact solution. A simple physical interpretation of the SCV approximation is also presented.

5.2 Introduction

Consider a monochromatic plane wave scattering from an infinitely long homogeneous and isotropic composite cylinder. The composite cylinder is composed of a small core cylinder of radius b that is eccentrically embedded into a large host cylinder of radius a , as shown in Figure 5.1. To *experimentally* isolate the core cylinder’s contribution to the scattered field of the composite cylinder, one would measure the total field $U^{(1)}$ outside the composite cylinder and the total field $U^{(1)}$ outside an identical host cylinder. Then, the difference, $V^{(\text{sca})}(r, \theta) =$

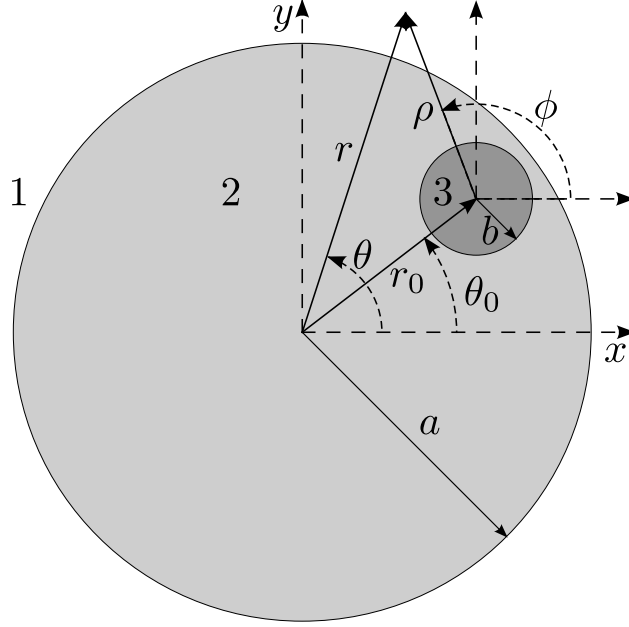


Figure 5.1: The cross-sectional view of the composite cylinder, with regions labeled by a number, is shown. Region 1 is the space outside of the composite cylinder ($r > a$), Region 2 is the host cylinder, and Region 3 is the core cylinder. The origin of the (r, θ) coordinate system, where $-\pi \leq \theta < \pi$, is centered on the host cylinder, and the origin of the (ρ, ϕ) coordinate system, where $-\pi \leq \phi < \pi$, is centered on the core cylinder. The axes of these two coordinate systems are parallel to each other and the center of the (ρ, ϕ) coordinate system is offset by $r_0 \cos \theta_0 \hat{\mathbf{x}} + r_0 \sin \theta_0 \hat{\mathbf{y}}$ with respect to the origin of the (r, θ) coordinate system.

$U^{(1)}(r, \theta) - \mathbb{U}^{(1)}(r, \theta)$, would contain the effect that the core cylinder had on the scattered field. In our recent paper [1], we considered the simplest composite cylinder geometry (the core cylinder is *concentric* with the host cylinder) and developed an approximation to $V^{(\text{sca})}$, which we termed the “screened cylindrical void/core” (SCV) approximation. In this paper, we derive an analogous formula for an eccentrically stratified composite cylinder, which can also be interpreted as an orders-of-scattering approximation. Furthermore, we numerically investigate the accuracy of the SCV approximation when $|k_2|a \approx 300$ and $0 < |k_3|b \leq 1$, where k_2 (k_3) is the wavenumber in the host (core) cylinder.

Scattering by an eccentrically stratified composite cylinder has previously been considered in the literature in various contexts [2–4] and by various techniques [5–7]. In the electromagnetic context, a perturbation series solution has been constructed in powers of $(k_3 - k_2)$ [8, 9],

b [10], and eccentricity [11, 12] by using separation of variables. An “exact” treatment based on separation of variables with a truncation of the resultant infinite size matrix is also available, e.g. in [13]. Our orders-of-scattering approach is also based on separation of variables, but the resultant power series expansion of the solution is different from the ones mentioned above.

There are many diverse applications where the scattering by an eccentrically stratified composite cylinder is important; for example, see [4, 8, 9] and references therein. As mentioned in [1], we are particularly interested in using the composite cylinder to study Anderson localization [14–16] at millimeter/sub-millimeter wavelengths. At these wavelengths, both the amplitude and the phase of the electromagnetic field can be easily measured with a vector network analyzer [17], and the preparation of disordered samples is straightforward with standard computer-numerically-controlled milling techniques. For example, a sample may be prepared by drilling small holes in a large Teflon (ultra low-loss material) cylinder. Furthermore, essentially arbitrary realizations of the same random disorder may be generated by putting the sample on a rotational stage and illuminating it from the side. When the number of small scatterers is large, say, over a thousand, then what is important is the rate at which the scatterer extinguishes the energy from the incident field, rather than the geometrical shape/size of each individual scatterer [18, 19]. Practically, the host cylinder needs to be rather large ($a \sim 10$ cm) in order to accommodate thousands of small holes ($b \sim 0.3$ mm); hence the numerical examples considered in this paper are for $k_2 a \approx 300$ and $0 < k_3 b \leq 1$. Therefore, the physical insight gained from considering the scattering by a single core cylinder eccentrically embedded into a large host, as discussed in this paper, may be of benefit in understanding the experimental model described above. Also, the approach taken in this paper may pave the way for methods that may accurately describe the full envisioned experiment, where thousands of core cylinders are eccentrically embedded into one large host cylinder.

5.3 Background and conventions

Throughout the paper, we will use the Gaussian unit system, and we will assume that all fields are harmonic in time with a $\exp(-i\omega t)$ time factor, where ω is the angular frequency. Furthermore, we will assume that all fields are polarized in the positive $\hat{\mathbf{z}}$ -direction. The positive $\hat{\mathbf{z}}$ -direction is out of the page in Figure 5.1. All media considered in this paper are assumed to be non-magnetic, and the permittivity of the host and the core cylinder are denoted by ϵ_2 and ϵ_3 , respectively. Furthermore, ϵ_1 denotes the permittivity of the space outside the composite cylinder (Region 1 in Figure 5.1) and is assumed to be purely real, whereas ϵ_2 and ϵ_3 may be complex.

Let us note that all fields in this paper satisfy the two-dimensional (2D) Helmholtz equation. The radial solution of the 2D Helmholtz equation is composed of a linear combination of an integer order Bessel function of the first kind and an integer order Hankel function of the first kind, which we denote by $J_m(\xi)$ and $H_m(\xi)$, respectively. The functions $J_m(\xi)$ and $H_m(\xi)$ satisfy the Wronskian relationship [20, §9.1]

$$J_m(\xi)H'_m(\xi) - J'_m(\xi)H_m(\xi) = \frac{2i}{\pi\xi}, \quad (5.1a)$$

and the recurrence relation [20, §9.2]

$$\Psi'_m(\xi) = \frac{m}{\xi}\Psi_m(\xi) - \Psi_{m+1}(\xi), \quad (5.1b)$$

where Ψ denotes J or H , and the prime denotes the derivative with respect to the argument. It is convenient to introduce the shorthand curly bracket notation, $\{\Psi_{m+1}(\xi); \Phi_m(\eta)\}$, by which we mean

$$\{\Psi_{m+1}(\xi); \Phi_m(\eta)\} \equiv \Psi_{m+1}(\xi)\Phi_m(\eta) - \frac{\eta}{\xi}\Psi_m(\xi)\Phi_{m+1}(\eta).$$

For example, if Ψ and Φ satisfy (5.1b), then

$$\{\Psi_{m+1}(\xi); \Phi_m(\eta)\} = \frac{\eta}{\xi}\Psi_m(\xi)\Phi'_m(\eta) - \Psi'_m(\xi)\Phi_m(\eta) \quad (5.1c)$$

Lastly, we note the Jacobi-Anger expansion of a plane wave [21, p. 37], namely,

$$e^{i\xi \cos \theta} = \sum_m i^m J_m(\xi) e^{im\theta}, \quad (5.2)$$

where \sum_m indicates the summation from $m = -\infty$ to $m = \infty$.

5.4 Host cylinder

Consider a unit plane wave, $\mathbb{U}^{(\text{inc})} = \exp(ik_1 r \cos \theta)$, incident from Region 1 onto the host cylinder, see Figure 5.1 with $b = 0$ (i.e., without the core cylinder). Then, after decomposing the total field in Region 1 as $\mathbb{U}^{(1)} = \mathbb{U}^{(\text{inc})} + \mathbb{U}^{(\text{sca})}$, we have [1]

$$\begin{bmatrix} \mathbb{U}^{(\text{sca})}(r, \theta) \\ \mathbb{U}^{(2)}(r, \theta) \end{bmatrix} = \sum_m i^m \begin{bmatrix} \mathbb{A}_m H_m(k_1 r) \\ \mathbb{B}_m J_m(k_2 r) \end{bmatrix} e^{im\theta}, \quad (5.3)$$

where $k_i = \sqrt{\epsilon_i} \omega / c$ for $i = 1, 2$ and c is the speed of light in vacuum. In (5.3), $\mathbb{U}^{(2)}$ denotes the total field inside the host cylinder, and the expansion coefficients are given by

$$\mathbb{A}_m = -\frac{\{J_{m+1}(k_1 a); J_m(k_2 a)\}}{\{H_{m+1}(k_1 a); J_m(k_2 a)\}}, \quad (5.4a)$$

$$\mathbb{B}_m = \frac{-2i}{\pi k_1 a \{H_{m+1}(k_1 a); J_m(k_2 a)\}}. \quad (5.4b)$$

5.5 Composite cylinder

If the plane wave $\mathbb{U}^{(\text{inc})}$ is incident from Region 1 onto the composite cylinder shown in Figure 5.1, then the total fields in Regions 1, 2, and 3 may be written as

$$U^{(1)}(r, \theta) = \mathbb{U}^{(1)}(r, \theta) + V^{(\text{sca})}(r, \theta), \quad (5.5a)$$

$$U^{(2)}(r, \theta; \rho, \phi) = \mathbb{U}^{(2)}(r, \theta) + V^{(2)}(r, \theta; \rho, \phi), \quad (5.5b)$$

and

$$U^{(3)}(\rho, \phi) = \sum_m i^m D_m J_m(k_3 \rho) e^{im\phi}, \quad (5.5c)$$

respectively, where

$$V^{(\text{sca})}(r, \theta) = \sum_m \mathbf{i}^m A_m H_m(k_1 r) e^{\mathbf{i}m\theta}, \quad (5.5d)$$

$$V^{(2)}(r, \theta; \rho, \phi) = \sum_m \mathbf{i}^m (B_m J_m(k_2 r) e^{\mathbf{i}m\theta} + C_m H_m(k_2 \rho) e^{\mathbf{i}m\phi}), \quad (5.5e)$$

and $k_3 = \sqrt{\epsilon_3} \omega / c$. In writing (5.5), we are thinking of the composite cylinder as the host cylinder into which a scatterer (the core cylinder) has been inserted. Also, notice that we required $U^{(3)}(\rho, \phi)$ to be finite at $\rho = 0$, and imposed the Sommerfeld radiation (*outgoing* cylindrical wave) condition on $V^{(\text{sca})}(r, \theta)$. To find the unknown expansion coefficients in (5.5), we require that the electric field and its normal derivative be continuous across the $\rho = b$ and $r = a$ interfaces.

To apply the continuity conditions at the $\rho = b$ interface, we first re-express $U^{(2)}(r, \theta; \rho, \phi)$ solely in terms of the (ρ, ϕ) coordinate system by using Graf's addition theorem [21, §2.5], [20, §9.2]. Namely, using

$$J_m(k_2 r) e^{\mathbf{i}m\theta} = \sum_n J_{m-n}(k_2 r_0) e^{\mathbf{i}(m-n)\theta_0} J_n(k_2 \rho) e^{\mathbf{i}n\phi},$$

and (5.3) with (5.2), we obtain

$$U^{(2)}(\rho, \phi) = \sum_n \mathbf{i}^{-n} J_n(k_2 \rho) e^{\mathbf{i}n\phi} \sum_m T_{nm} (\mathbb{B}_m + B_m) + \sum_m \mathbf{i}^m C_m H_m(k_2 \rho) e^{\mathbf{i}m\phi},$$

where $T_{nm} = \mathbf{i}^{m+n} J_{m-n}(k_2 r_0) e^{\mathbf{i}(m-n)\theta_0}$. Then, requiring that $U^{(2)} = U^{(3)}$ and $\frac{\partial}{\partial \rho} U^{(2)} = \frac{\partial}{\partial \rho} U^{(3)}$ on $\rho = b$ yields

$$D_p J_p(k_3 b) = C_p H_p(k_2 b) + (-1)^p J_p(k_2 b) \sum_m T_{pm} (\mathbb{B}_m + B_m), \quad (5.6a)$$

and

$$\frac{k_3}{k_2} D_p J'_p(k_3 b) = C_p H'_p(k_2 b) + (-1)^p J'_p(k_2 b) \sum_m T_{pm} (\mathbb{B}_m + B_m), \quad (5.6b)$$

respectively. Eliminating D_p from (5.6) yields

$$C_p = (-1)^p \Delta_p \sum_m T_{pm} (\mathbb{B}_m + B_m), \quad (5.7a)$$

where

$$\Delta_p = -\frac{\{J_{p+1}(k_3b); J_p(k_2b)\}}{\{J_{p+1}(k_3b); H_p(k_2b)\}}. \quad (5.7b)$$

Similarly, to apply the continuity conditions at the $r = a$ interface, we first re-express $U^{(2)}(r, \theta; \rho, \phi)$ solely in terms of the (r, θ) coordinate system by using Graf's addition theorem for $H_m(k_2\rho)e^{im\phi}$ [21, §2.5], [20, §9.2]. Namely, using

$$H_m(k_2\rho)e^{im\phi} = \sum_n (-1)^{m-n} J_{m-n}(k_2r_0)e^{i(m-n)\theta_0} H_n(k_2r)e^{in\theta}$$

for $r > r_0$, and (5.3) with (5.2), we obtain

$$U^{(2)}(r, \theta) = \sum_m i^m (\mathbb{B}_m + B_m) J_m(k_2r)e^{im\theta} + \sum_n i^n H_n(k_2r)e^{in\theta} \sum_m (-1)^m T_{nm} C_m,$$

for $r_0 + b < r < a$. Then, requiring that $U^{(1)} = U^{(2)}$ and $\frac{\partial}{\partial r}U^{(1)} = \frac{\partial}{\partial r}U^{(2)}$ on $r = b$ yields

$$(\mathbb{B}_p + B_p) J_p(k_2a) + H_p(k_2a) \sum_m (-1)^m T_{pm} C_m = J_p(k_1a) + (\mathbb{A}_p + A_p) H_p(k_1a), \quad (5.8a)$$

and

$$(\mathbb{B}_p + B_p) J'_p(k_2a) + H'_p(k_2a) \sum_m (-1)^m T_{pm} C_m = \frac{k_1}{k_2} [J'_p(k_1a) + (\mathbb{A}_p + A_p) H'_p(k_1a)], \quad (5.8b)$$

respectively. To solve (5.8) for A_p in terms of C_m , we eliminate $(\mathbb{B}_p + B_p)$ from (5.8), and then use (5.1a) and (5.4) to rewrite the result as

$$A_p = \mathbb{B}_p \sum_m (-1)^m T_{pm} C_m. \quad (5.9)$$

To solve (5.8) for B_p in terms of A_p , we eliminate C_m from (5.8), and use (5.1a) to obtain

$$\frac{2i}{\pi k_1 a} (\mathbb{B}_p + B_p) = (\mathbb{A}_p + A_p) \{H_{p+1}(k_1a); H_p(k_2a)\} + \{J_{p+1}(k_1a); H_p(k_2a)\}. \quad (5.10)$$

To simplify (5.10) further, we substitute (5.4) into (5.10) and note that

$$\begin{aligned} & \{J_{p+1}(k_1 a); H_p(k_2 a)\} \{H_{p+1}(k_1 a); J_p(k_2 a)\} \\ & - \{J_{p+1}(k_1 a); J_p(k_2 a)\} \{H_{p+1}(k_1 a); H_p(k_2 a)\} = \left(\frac{2}{\pi k_1 a}\right)^2 \end{aligned}$$

to obtain

$$B_p = \frac{\pi k_1 a}{2i} \{H_{p+1}(k_1 a); H_p(k_2 a)\} A_p. \quad (5.11)$$

Finally, substituting (5.11) into (5.7a), and putting the result into (5.9) yields

$$\sum_n (\delta_{mn} - F_{mn}) A_n = G_m, \quad (5.12a)$$

where

$$F_{mn} = \frac{\pi k_1 a}{2i} \mathbb{B}_m \left(\sum_p T_{mp} \Delta_p T_{pn} \right) \{H_{n+1}(k_1 a); H_n(k_2 a)\}, \quad (5.12b)$$

$$G_m = \sum_n \mathbb{B}_m \left(\sum_p T_{mp} \Delta_p T_{pn} \right) \mathbb{B}_n, \quad (5.12c)$$

and δ_{mn} denotes the Kronecker delta function.

Notice that in (5.12) the core cylinder parameters, namely, k_3 and b , are solely contained in Δ_p , see (5.7b). Furthermore, from (5.7b) and the small argument forms of J_p and H_p , we see that if the core cylinder is small, then so is Δ_p . This suggests that (5.12a) can be solved via the Neumann series (Taylor series expansion, if you will), i.e.,

$$\mathbf{A} = (\mathbf{I} - \mathbf{F})^{-1} \mathbf{G} = \sum_{\ell=0}^{\infty} \mathbf{F}^{\ell} \mathbf{G}, \quad (5.13)$$

where A_n , F_{mn} , G_m are the elements of \mathbf{A} , \mathbf{F} , \mathbf{G} , respectively, and \mathbf{I} is the identity matrix. The Neumann series in (5.13) converges, provided that the spectral radius of \mathbf{F} is less than one [22, §4.3]. The spectral radius of \mathbf{F} for a large host cylinder, $|k_2|a \approx 300$, with an eccentrically embedded core cylinder is shown in Figure 5.2. From Figure 5.2, we see that the spectral radius of \mathbf{F} is indeed much smaller than one and thus, we expect the Neumann series in (5.13) to converge rapidly. We will discuss the spectral radius of \mathbf{F} further in Sec. 5.7, but for now turn our attention to the physical interpretation of the SCV approximation.

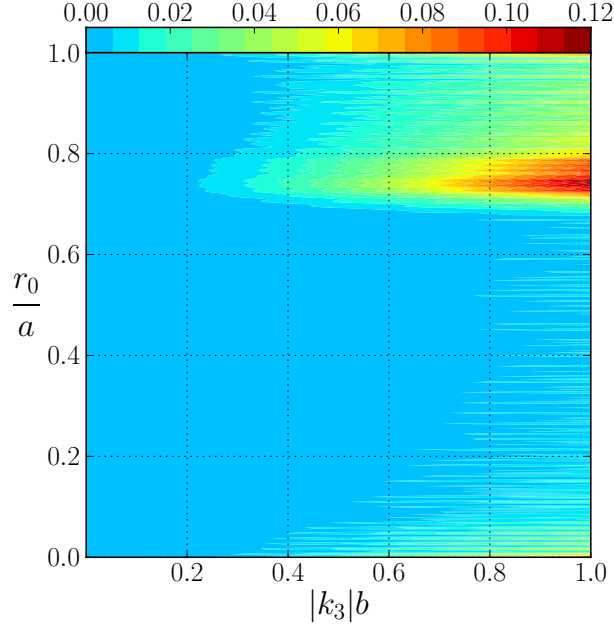


Figure 5.2: The spectral radius of \mathbf{F} at 100 GHz for a Teflon host cylinder ($a = 10$ cm) with an eccentrically embedded quartz core cylinder is shown as a function of $|k_3|b$, and eccentricity, r_0/a (with $\theta_0 = 0$). The permittivity of Teflon and quartz at 100 GHz is 2.1 and 3.8 with a negligible loss-tangent [23], respectively.

5.6 The SCV approximation and its physical interpretation

If only the $\ell = 0$ term is retained in (5.13), we obtain the SCV approximation, namely,

$$A_m \cong G_m = \sum_n \mathbb{B}_m \left(\sum_p T_{mp} \Delta_p T_{pn} \right) \mathbb{B}_n. \quad (5.14)$$

To interpret (5.14) physically, we consider the following three-step scattering process:

1. If a unit plane wave, $\mathbb{U}^{(\text{inc})} = \exp(ik_1 r \cos \theta)$, is incident on the host cylinder, then the field inside the host cylinder, $\mathbb{U}^{(2)}(r, \theta)$, is given by (5.3). Rewriting $\mathbb{U}^{(2)}$ terms of the (ρ, ϕ) coordinate system yields

$$\mathbb{U}^{(2)}(\rho, \phi) = \sum_n i^{-n} J_n(k_2 \rho) e^{in\phi} \sum_m T_{nm} \mathbb{B}_m. \quad (5.15)$$

2. If we use (5.15) as an *incident* field for the core cylinder, then the resulting scattered field is

$$\sum_m \mathbf{i}^m \tilde{C}_m H_m(k_2 \rho) e^{\mathbf{i}m\phi}, \quad (5.16a)$$

and the field inside the core cylinder is

$$\tilde{U}^{(3)}(\rho, \phi) = \sum_m \mathbf{i}^m \tilde{D}_m J_m(k_3 \rho) e^{\mathbf{i}m\phi}. \quad (5.16b)$$

Substituting (5.15) and (5.16) into the continuity conditions for the $\rho = b$ interface, and eliminating \tilde{D}_m from the resultant two equations, yields

$$\tilde{C}_p = (-1)^p \Delta_p \sum_m T_{pm} \mathbb{B}_m. \quad (5.17)$$

3. Finally, if we use (5.16a) with (5.17) as an *incident* field (from within the host cylinder) on the $r = a$ interface, then there will be an outgoing field outside the host cylinder given by

$$\tilde{V}^{(\text{sca})}(r, \theta) = \sum_m \mathbf{i}^m \tilde{A}_m H_m(k_1 r) e^{\mathbf{i}m\theta}, \quad (5.18a)$$

and a regular (finite at $r = 0$) field inside the host cylinder given by

$$\sum_m \mathbf{i}^m \tilde{B}_m J_m(k_2 r) e^{\mathbf{i}m\theta}. \quad (5.18b)$$

Rewriting (5.16a) in terms of the (r, θ) coordinate system and substituting it, as well as (5.18), into the continuity conditions for the $r = a$ interface, and eliminating \tilde{B}_m from the resultant two equations yields

$$\tilde{A}_m = \sum_n \mathbb{B}_m \left(\sum_p T_{mp} \Delta_p T_{pn} \right) \mathbb{B}_n. \quad (5.19)$$

By comparing (5.19) with (5.14), we conclude that the SCV approximation can be viewed as an orders-of-scattering approximation. Moreover, from the above three-step scattering process, we see that $T_{pn} \mathbb{B}_n$ is the “screening” effect of the host cylinder on $\mathbb{U}^{(\text{inc})}$ and $\mathbb{B}_m T_{mp}$ is the “screening” effect of the host cylinder on $\tilde{V}^{(\text{sca})}$. These two screening effects are identical

if the core cylinder is *concentric* with the host cylinder, as we have shown in [1]. To see that (5.19), or equivalently (5.14), reduces to our previous result, we note that $T_{pn} = i^{n+p} \delta_{pn}$ and $T_{mp} = i^{p+m} \delta_{mp}$ when $r_0 = 0$, and thus, the sums in (5.19) collapse and we obtain $\tilde{A}_m = \mathbb{B}_m^2 \Delta_m$.

5.7 Numerical examples and limitations

In practice, the computation of the A_m coefficients via (5.12) or (5.14) requires the truncation of the infinite sums, as well as the index m . From (5.12b), (5.12c), and (5.14), we see that the sum over p is controlled by the small core cylinder parameters, namely, Δ_p . This observation suggests that the summation over p be terminated at p_{\max} (i.e., $|p| \leq p_{\max}$), where p_{\max} is given by the well-known Wiscombe's criterion for small scatterers [24], namely,

$$p_{\max} = \left\lceil k_2 b + 4 (k_2 b)^{1/3} + 1 \right\rceil. \quad (5.20a)$$

The sum over n , as well as the index m , are controlled by the large host cylinder and thus, they are terminated at N_{\max} (i.e., $|n| \leq N_{\max}$ and $|m| \leq N_{\max}$), where N_{\max} is given by the Wiscombe's criterion for relatively large scatterers [24], namely,

$$N_{\max} = \left\lceil k_1 a + 4.05 (k_1 a)^{1/3} + 2 \right\rceil. \quad (5.20b)$$

We note that a termination criterion in terms of prescribed relative error has become available recently [25], but for our purposes, the termination condition given by (5.20) will be sufficient.

To numerically illustrate the accuracy of the SCV approximation, we compute the relative error in the rate at which the energy is extinguished by the core cylinder in the presence of the host cylinder. The rate at which the energy (per unit length of the composite cylinder) is depleted by the core cylinder from the total field, $\mathbb{U}^{(1)}$, outside the host cylinder is given by [1]

$$Q^{\text{ext}} = -\frac{c^2}{2\pi\omega} \sum_{m=-N_{\max}}^{N_{\max}} \left(\text{Re}[A_m] + 2\text{Re}[\mathbb{A}_m A_m^*] \right), \quad (5.21)$$

where Re denotes the real part and $*$ denotes the complex conjugate. We compute the SCV approximate and numerically-exact (≈ 7 significant digits) Q^{ext} by using (5.21) with (5.14) and (5.21) with (5.13), respectively. The top row of Figure 5.3 shows that the SCV approximation is in good agreement with the numerically-exact solution, and the bottom row of Figure 5.3 demonstrates that the Neumann series in (5.13) converges rapidly as one would expect from the spectral radius of \mathbf{F} , see Figure 5.2. Furthermore, from Figure 5.3 we see that the relative error in Q^{ext} is almost independent of the angular position of the core cylinder but does depend on its radial position, see Figure 5.3 with $r_0/a > 0.7$.

The dependence of the relative error in Q^{ext} on the radial position of the core cylinder may be explained in terms of the internal resonances of the host cylinder. These resonances are often referred to as Mie resonances, morphological resonances, whispering-gallery modes, or natural/eigen modes. At 100 GHz, the 10 cm host cylinder is about hundred times larger than the wavelength of the incident light and thus, the interaction of light with the host cylinder can be described by ray theory. If a ray inside the host cylinder strikes the surface of the host cylinder above the critical angle, then the ray's trajectory will be bounded by a cylindrical annulus with outer radius a and inner radius r_{caustic} . To find the caustic radius, r_{caustic} , we set the ray's angular momentum $|k_{2,\theta}|r\hbar$ equal to $|m|\hbar$ (the angular momentum of the m th eigenmode) and note that $k_2^2 = k_{2,\theta}^2 + k_{2,r}^2$ to obtain

$$r_{\text{caustic}} = \left| \frac{m}{k_2} \right|. \quad (5.22a)$$

In the derivation of (5.22a), we used the fact that the radial component of the wavevector must vanish on r_{caustic} , i.e., $k_{2,r}(r = r_{\text{caustic}}) = 0$ [26, 27]. Furthermore, we can deduce the range of potentially excited eigenmodes of the host cylinder as follows. If a ray inside the host cylinder strikes the surface at an angle γ with respect to the normal, then by equating the ray's and modal angular momenta ($|m| = |k_2|a \sin \gamma$), and using the total internal reflection condition, $\sqrt{\epsilon_1/\epsilon_2} \leq \sin \gamma \leq 1$, we obtain

$$|k_1|a \leq m \leq |k_2|a. \quad (5.22b)$$

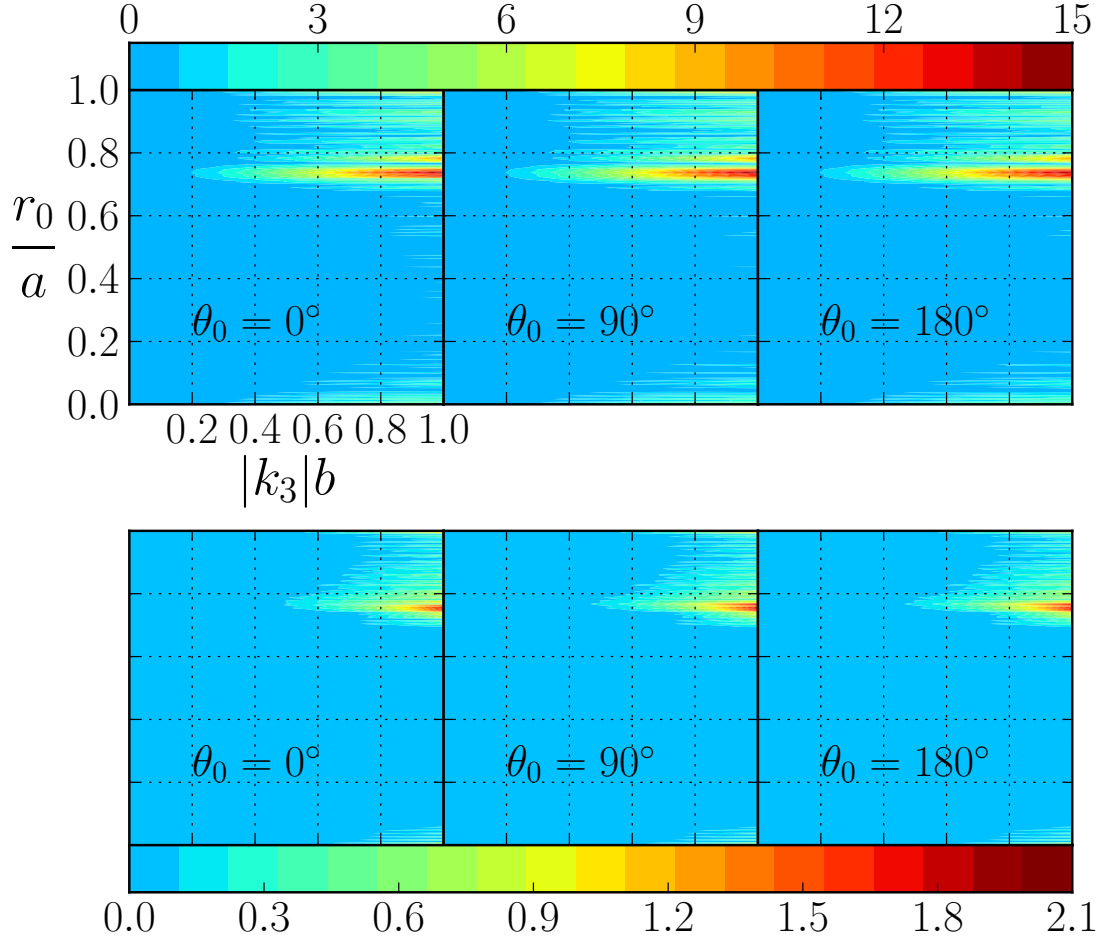


Figure 5.3: The relative error in Q^{ext} (in percent) is shown as a function of $|k_3|b$ and eccentricity, r_0/a , for various θ_0 angles. The top row shows the relative error if only the $\ell = 0$ term is retained in (5.13), i.e., the SCV approximation, and the bottom row shows the relative error if the $\ell = 0$ and $\ell = 1$ terms are retained. The above plot was produced with the same parameters as the ones described in the caption of Figure 5.2

Finally, from (5.22), we see why the SCV approximation worsens when the radial location of the core cylinder exceeds the caustic radius, see Figure 5.3 for $r_0/a \geq r_{\text{caustic}}/a \approx 0.7$.

If the frequency of the incident wave corresponds to one of the eigenfrequencies of the host cylinder, then the Neumann series in (5.13) will fail to converge *only* when $r_0 \geq r_{\text{caustic}}$. For example, the mode $m = 228$ is excited in resonance at approximately 99.823859 GHz, i.e., the denominator of \mathbb{B}_{228} vanishes at this frequency¹⁰, and the spectral radius of \mathbf{F} exceeds unity when $r_0/a \leq r_{\text{caustic}}/a = 228/(k_2 a) \approx 0.75$ as shown in Figure 5.4. Moreover, from Figure 5.2 we see that the SCV approximation remains valid even at resonance frequency, provided that $r_0/a < r_{\text{caustic}}/a \approx 0.75$.

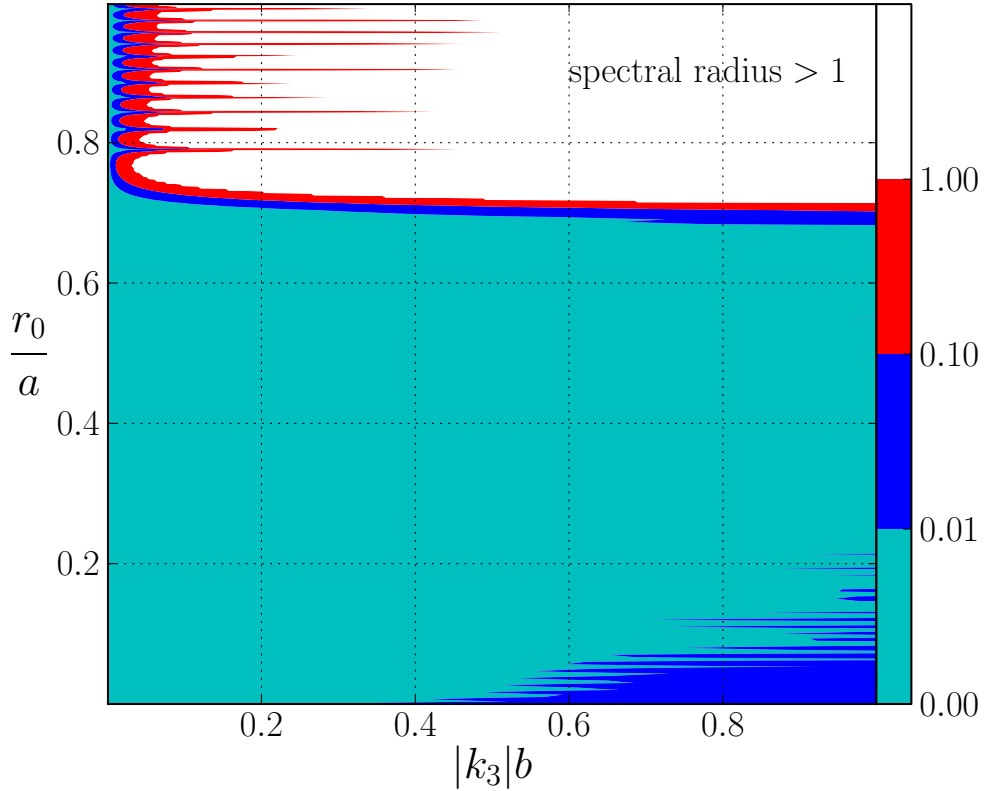


Figure 5.4: The spectral radius of \mathbf{F} at eigenfrequency 99.823859 GHz is shown as a function $|k_3|b$ and eccentricity, r_0/a (with $\theta_0 = 0$). The above plot was produced with the same parameters as the ones described in the caption of Figure 5.2

¹⁰Strictly speaking, this occurs at a *complex* eigenfrequency, where the imaginary part of the eigenfrequency is related to the spectral width of the mode [28].

5.8 Conclusions

In this paper, we have extended the screen cylindrical void/core (SCV) approximation [1] to a case where the small core cylinder is *eccentrically* embedded into a large host cylinder. We physically interpreted the SCV approximation as the screening effect of the host cylinder on the incident plane wave and the wave scattered by the core cylinder (see Section 5.6). Furthermore, we showed that the SCV approximation may be thought of as an orders-of-scattering approximation.

The accuracy of the SCV approximation was demonstrated numerically for an envisioned localization experiment, where a large host cylinder ($k_2a \approx 300$) contains a small ($k_3b \sim 1$) eccentrically embedded core cylinder. In general, the SCV approximation was shown to be in good agreement with the exact solution, even at the eigenfrequencies of the host cylinder. We showed that if the incident frequency corresponds to one of the eigenfrequencies of the host cylinder, then the SCV approximation remains valid, provided that the eccentricity r_0/a does not exceed the caustic radius of the mode (see Section 5.7). This condition was derived by considering the interplay between the ray and wave pictures of the scattering process. Moreover, the ray picture offered a valuable physical insight into the validity of the SCV approximation.

5.9 Acknowledgment

This material is based upon work supported in part by the U.S. Office of Naval Research as a Multi-disciplinary University Research Initiative on Sound and Electromagnetic Interacting Waves under grant number N00014-10-1-0958.

5.10 References Cited

- [1] A. J. Yuffa, J. A. Scales, Measuring the void: Theoretical study of scattering by a cylindrical annulus, J. Quant. Spectrosc. Radiat. Transfer (2013). [doi:10.1016/j.jqsrt.2013.02.017](https://doi.org/10.1016/j.jqsrt.2013.02.017).

- [2] J. A. Roumeliotis, N. B. Kakogiannos, Acoustic scattering from an infinite cylinder of small radius coated by a penetrable one, *Journal of the Acoustical Society of America* 97 (1995) 2074–2081.
- [3] J.-M. A. Noël, A. J. Patitsas, Modes of vibration in an ideal fluid bounded by two eccentric rigid infinite circular cylindrical boundaries, *Canadian Journal of Physics* 76 (1998) 729–738.
- [4] L.-W. Cai, Scattering of elastic anti-plane shear waves by multilayered eccentric scatterers, *Quarterly Journal of Mechanics and Applied Mathematics* 58 (2005) 165–183.
- [5] R. P. Shaw, T. George, Time harmonic acoustic radiation from nonconcentric circular cylinders, *The Journal of the Acoustical Society of America* 56 (1974) 1437–1443.
- [6] X. Yuan, D. R. Lynch, J. W. Strohbehn, Coupling of finite element and moment methods for electromagnetic scattering from inhomogeneous objects, *Antennas and Propagation, IEEE Transactions on* 38 (1990) 386–393.
- [7] E. B. Danila, J. M. Conoir, J. L. Izbicki, Generalized Debye series expansion: Part II, treatment of eccentric fluid-solid cylindrical interfaces, *Acta Acustica united with Acustica* 84 (1998) 38–44.
- [8] N. K. Uzunoglu, J. G. Fikioris, Scattering from an infinite dielectric cylinder embedded into another, *Journal of Physics A: Mathematical and General* 12 (1979) 825–834.
- [9] C. A. Valagiannopoulos, Electromagnetic scattering from two eccentric metamaterial cylinders with frequency-dependent permittivities differing slightly each other, *Progress In Electromagnetics Research B* 3 (2008) 23–34.
- [10] J. A. Roumeliotis, N. B. Kakogiannos, Scattering from an infinite cylinder of small radius embedded into a dielectric one, *Microwave Theory and Techniques, IEEE Transactions on* 42 (1994) 463–470.
- [11] J. A. Roumeliotis, J. G. Fikioris, G. P. Gounaris, Electromagnetic scattering from an eccentrically coated infinite metallic cylinder, *Journal of Applied Physics* 51 (1980) 4488–4493.
- [12] G. P. Zouros, J. A. Roumeliotis, G.-T. Stathis, Electromagnetic scattering by an infinite cylinder of material or metamaterial coating eccentrically a dielectric cylinder, *J. Opt. Soc. Am. A* 28 (2011) 1076–1085.
- [13] R. P. Parrikar, A. A. Kishk, A. Z. Elsherbeni, Scattering from an impedance cylinder embedded in a nonconcentric dielectric cylinder, *Microwaves, Antennas and Propagation, IEE Proceedings H* 138 (1991) 169–175.

- [14] P. W. Anderson, Absence of diffusion in certain random lattices, *Phys. Rev.* 109 (1958) 1492–1505.
- [15] A. Lagendijk, B. van Tiggelen, D. S. Wiersma, Fifty years of Anderson localization, *Physics Today* 62 (2009) 24–29.
- [16] T. Sperling, W. Bührer, C. M. Aegerter, G. Maret, Direct determination of the transition to localization of light in three dimensions, *Nature Photonics* 7 (2013) 48–52.
- [17] J. A. Scales, L. D. Carr, D. B. McIntosh, V. Freilikher, Y. P. Bliokh, Millimeter wave localization: Slow light and enhanced absorption in random dielectric media, *Phys. Rev. B* 76 (2007) 085118.
- [18] M. Rusek, A. Orłowski, Analytical approach to localization of electromagnetic waves in two-dimensional random media, *Phys. Rev. E* 51 (1995) R2763–R2766.
- [19] M. Rusek, A. Orłowski, Example of self-averaging in three dimensions: Anderson localization of electromagnetic waves in random distributions of pointlike scatterers, *Phys. Rev. E* 56 (1997) 6090–6094.
- [20] M. Abramowitz, I. A. Stegun (Eds.), *Handbook of Mathematical Functions*, Dover, New York, 1965.
- [21] P. A. Martin, *Multiple Scattering*, Cambridge University Press, Cambridge, 2006.
- [22] N. J. Higham, *Functions of Matrices*, SIAM, Philadelphia, 2008.
- [23] P. F. Goldsmith, *Quasioptical Systems: Gaussian Beam Quasioptical Propagation and Applications*, Wiley-IEEE Press, New York, 1998.
- [24] W. J. Wiscombe, Improved Mie scattering algorithms, *Appl. Opt.* 19 (1980) 1505–1509.
- [25] A. A. R. Neves, D. Pisignano, Effect of finite terms on the truncation error of Mie series, *Opt. Lett.* 37 (2012) 2418–2420.
- [26] G. Roll, G. Schweiger, Geometrical optics model of Mie resonances, *J. Opt. Soc. Am. A* 17 (2000) 1301–1311.
- [27] J. Schulte, G. Schweiger, Resonant inelastic scattering by use of geometrical optics, *J. Opt. Soc. Am. A* 20 (2003) 317–324.
- [28] P. R. Conwel, P. W. Barber, C. K. Rushforth, Resonant spectra of dielectric spheres, *J. Opt. Soc. Am. A* 1 (1984) 62–67.

CHAPTER 6

GENERALIZATION OF THE SCV APPROXIMATION TO A CLUSTER OF ECCENTRICALLY EMBEDDED CORES

The SCV approximation derived for a composite cylinder with one eccentrically embedded core cylinder may be generalized to a case of N eccentrically embedded core cylinders via the so-called cluster T -matrix. The cluster T -matrix [1, 2] [3, §5.9] [4, §7.11] relates the expansion coefficients of the wave incident on the cluster to the expansion coefficients of the wave scattered by the cluster. In other words, the cluster T -matrix allows us to treat all of the eccentrically embedded cylinders as one unit. Therefore, the derivation of the SCV approximation for N eccentrically embedded core cylinders will closely parallel the derivation in Chapter 5.

The composite cylinder with N eccentrically embedded core cylinders is shown in Figure 6.1, where a is the radius of the host cylinder and the radius of the i th core cylinder is denoted by b_i . In what follows, it is convenient to let

$$\Psi_n(k_j \mathbf{r}) = H_n(k_j r) e^{in\theta}, \quad (6.1a)$$

$$\hat{\Psi}_n(k_j \mathbf{r}) = J_n(k_j r) e^{in\theta}, \quad (6.1b)$$

where k_j is the wavenumber in the j th region, and express Graf's addition theorems [4, §2.5] [5, §10.23] in the notation of (6.1) as

$$\hat{\Psi}_m(k \mathbf{w}) = \sum_n \hat{\Psi}_{m-n}(k \mathbf{u}) \hat{\Psi}_n(k \mathbf{v}), \quad (6.2a)$$

$$\Psi_m(k \mathbf{v}) = \sum_n \Psi_{m-n}(-k \mathbf{u}) \hat{\Psi}_n(k \mathbf{w}), \quad |\mathbf{w}| < |\mathbf{u}|, \quad (6.2b)$$

$$\Psi_m(k \mathbf{v}) = \sum_n \hat{\Psi}_{m-n}(-k \mathbf{u}) \Psi_n(k \mathbf{w}), \quad |\mathbf{w}| > |\mathbf{u}|. \quad (6.2c)$$

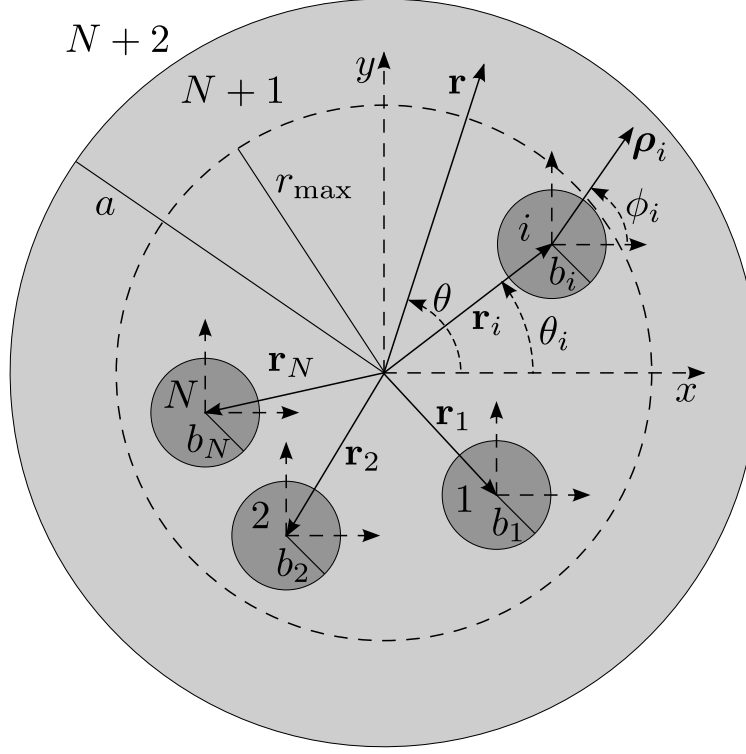


Figure 6.1: The cross-sectional view of the composite cylinder is shown. Region $N + 2$ is the space outside of the composite cylinder ($r > a$), region $N + 1$ is the host cylinder, and regions $1, \dots, N$ are the core cylinders. The origin of the global (r, θ) coordinate system, where $-\pi \leq \theta < \pi$, is centered on the host cylinder, and the origin of the local (ρ_i, ϕ_i) coordinate system, where $-\pi \leq \phi_i < \pi$, is centered on the i th core cylinder. The axes of the (r, θ) and (ρ_i, ϕ_i) coordinate systems are parallel to each other and the center of the (ρ_i, ϕ_i) coordinate system is offset by \mathbf{r}_i with respect to the origin of the (r, θ) coordinate system.

6.1 Host cylinder with and without core cylinders

If we assume that the incident wave on the host cylinder is regular (non-singular) and satisfies the 2D Helmholtz equation, then the total field outside and inside the host cylinder is given by

$$\mathbb{U}^{(N+2)}(\mathbf{r}) = \sum_m \mathbb{A}_m \Psi_m(k_{N+2}\mathbf{r}) + \mathbb{D}_m \widehat{\Psi}(k_{N+2}\mathbf{r}), \quad (6.3a)$$

$$\mathbb{U}^{(N+1)}(\mathbf{r}) = \sum_m \mathbb{B}_m \widehat{\Psi}(k_{N+1}\mathbf{r}), \quad (6.3b)$$

respectively. The expansion coefficients in (6.3) are given by

$$\mathbb{A}_m = -\frac{\{J_{m+1}(k_{N+2}a); J_m(k_{N+1}a)\}}{\{H_{m+1}(k_{N+2}a); J_m(k_{N+1}a)\}} \mathbb{D}_m, \quad (6.4a)$$

$$\mathbb{B}_m = \frac{-2i}{\pi k_{N+2}a \{H_{m+1}(k_{N+2}a); J_m(k_{N+1}a)\}} \mathbb{D}_m, \quad (6.4b)$$

where the \mathbb{D}_m coefficients are assumed to be the known expansion coefficients of the incident wave. If we insert the cluster of core cylinders into the host cylinder in the presence of the $\mathbb{U}^{(N+2)}(\mathbf{r})$ and $\mathbb{U}^{(N+1)}(\mathbf{r})$ fields, then the new fields are given by

$$U^{(N+2)}(\mathbf{r}) = \mathbb{U}^{(N+2)}(\mathbf{r}) + V^{(\text{sca})}(\mathbf{r}), \quad (6.5a)$$

$$U^{(N+1)}(\mathbf{r}) = \mathbb{U}^{(N+1)}(\mathbf{r}) + V^{(N+1)}(\mathbf{r}), \quad r_{\text{max}} \leq r < a, \quad (6.5b)$$

where

$$V^{(\text{sca})}(\mathbf{r}) = \sum_m A_m \Psi_m(k_{N+2}\mathbf{r}), \quad (6.5c)$$

$$V^{(N+1)}(\mathbf{r}) = \sum_m \left[B_m \hat{\Psi}_m(k_{N+1}\mathbf{r}) + C_m \Psi_m(k_{N+1}\mathbf{r}) \right], \quad (6.5d)$$

and r_{max} is the radius of the smallest *imaginary* cylinder that circumscribes the cluster of core cylinders, see Figure 6.1. It is important to stress that the $r_{\text{max}} \leq r < a$ condition in (6.5b) allows us to treat the cluster of core cylinders as one entity. Physically, we may interpret $\mathbb{U}^{(N+1)}(\mathbf{r}) + \sum_m B_m \hat{\Psi}_m(k_{N+1}\mathbf{r})$ as the incident field on the cluster and $\sum_m C_m \Psi_m(k_{N+1}\mathbf{r})$ as the field scattered by the cluster. Of course, the field we experimentally measured by the procedure outlined in Section 5.2 is $V^{(\text{sca})}(\mathbf{r})$ and *not* $\sum_m C_m \Psi_m(k_{N+1}\mathbf{r})$.

To find the unknown expansion coefficients of the experimentally measurable field, we require the total field and its normal derivative to be continuous across the $r = a$ interface, to obtain

$$\mathbb{D}_m J_m(k_{N+2}a) + (\mathbb{A}_m + A_m) H_m(k_{N+2}a) = (\mathbb{B}_m + B_m) J_m(k_{N+1}a) + C_m H_m(k_{N+2}a), \quad (6.6a)$$

$$\begin{aligned} \mathbb{D}_m J'_m(k_{N+2}a) + (\mathbb{A}_m + A_m) H'_m(k_{N+2}a) \\ = \frac{k_{N+1}}{k_{N+2}} \left[(\mathbb{B}_m + B_m) J'_m(k_{N+1}a) + C_m H'_m(k_{N+2}a) \right]. \end{aligned} \quad (6.6b)$$

Eliminating $(\mathbb{B}_m + B_m)$ from (6.6), and using (6.4) with (5.1a) to simplify the result, yields

$$\mathbb{D}_m A_m = \mathbb{B}_m C_m. \quad (6.7a)$$

Eliminating C_m from (6.6) and then using (6.4), (5.1a), and

$$\begin{aligned} \{J_{m+1}(k_{N+2}a); H_m(k_{N+1}a)\} \{H_{m+1}(k_{N+2}a); J_m(k_{N+1}a)\} \\ - \{J_{m+1}(k_{N+2}a); J_m(k_{N+1}a)\} \{H_{m+1}(k_{N+2}a); H_m(k_{N+1}a)\} = \left(\frac{2}{\pi k_{N+2}a} \right)^2 \end{aligned}$$

to simplify the result, yields

$$B_m = \frac{\pi k_{N+2}a}{2i} \{H_{m+1}(k_{N+2}a); H_m(k_{N+1}a)\} A_m. \quad (6.7b)$$

The expansion coefficients, $(\mathbb{B}_m + B_m)$, of the wave incident onto the cluster of core cylinders must be linearly related to the expansion coefficients, C_m , of the wave scattered by the cluster because the Maxwell equations, material properties of the media, and the continuity conditions are all linear. Traditionally, this relationship is denoted by the so-called T -matrix (transition matrix) [6–9]. Thus, from the definition of the T -matrix, we have

$$C_m = \sum_n T_{mn} (\mathbb{B}_n + B_n). \quad (6.8)$$

Combining (6.7) with (6.8) yields

$$\sum_n (\delta_{mn} - F_{mn}) A_n = G_m, \quad (6.9a)$$

where

$$F_{mn} = \frac{1}{\mathbb{D}_m} \left[\frac{\pi k_{N+2}a}{2i} \mathbb{B}_m T_{mn} \{H_{n+1}(k_{N+2}a); H_n(k_{N+1}a)\} \right], \quad (6.9b)$$

$$G_m = \frac{1}{\mathbb{D}_m} \sum_n \mathbb{B}_m T_{mn} \mathbb{B}_n, \quad (6.9c)$$

and δ_{mn} denotes the Kronecker delta function. Let us compare the system of equations for the cluster of core cylinders (6.9) to the system of equations for one eccentrically embedded core cylinder (5.12). In (6.9), the physical and morphological properties of the cluster of core cylinders are solely contained in the T -matrix. Likewise, in (5.12) the effects of one eccentrically embedded core cylinder on the scattered field are solely contained in the parentheses term¹¹ in (5.12). In other words, the T -matrix in (6.9) plays the same role as the parentheses term in (5.12), and thus, we conclude that (6.9) is identical¹² to (5.12). In light of this conclusion, it follows from Chapter 5 that (6.9) may be solved via the Neumann series, where the first term in the series will give the SCV approximation. The SCV approximation (an orders-of-scattering approximation) and its physical interpretation were presented in Section 5.6 and we will not repeated here.

We now turn our attention to the cluster T -matrix that appears in (6.9). If we denote the T -matrix for the i th core cylinder as $\mathbf{T}^{(i)}$, then, as shown in the next section, the cluster T -matrix will be composed of $\mathbf{T}^{(i=1,\dots,N)}$. The explicit form of $\mathbf{T}^{(i)}$ may be deduced by inspection of (6.4a) to be

$$T_{nm}^{(i)} = -\frac{\{J_{n+1}(k_{N+1}b_i); J_m(k_i b_i)\}}{\{H_{n+1}(k_{N+1}b_i); J_m(k_i b_i)\}} \delta_{nm}, \quad i = 1, \dots, N. \quad (6.10)$$

6.2 Cluster T -matrix

To derive an expression for the cluster T -matrix, we analyze the fields inside the imaginary cylinder of radius r_{\max} , which contains the core cylinders, see Figure 6.1. The scattered field produced by the i th core cylinder is

$$\sum_m C_m^{(i)} \psi(k_{N+1} \boldsymbol{\rho}_i), \quad |\boldsymbol{\rho}_i| > b_i, \quad (6.11)$$

¹¹The T_{mp} and T_{pn} quantities in $(\sum_p T_{mp} \Delta_p T_{pn})$ are *not* related to the T -matrix. This rather unfortunate notation is a mere coincidence.

¹²The appearance of $1/\mathbb{D}_m$ in (6.9b) and (6.9c) is not important, since we could have absorbed it into the definition of $V^{(\text{sca})}(\mathbf{r})$ via $A_m \rightarrow \mathbb{D}_m A_m$ as was done in Chapter 5.

and the “external” incident field on the i th cylinder is

$$\sum_m (\mathbb{B}_m + B_m) \hat{\Psi}_m(k_{N+1}\mathbf{r}). \quad (6.12)$$

According to Foldy’s principle [10], the *effective* incident field on the i th core cylinder consists of the external incident field and the scattered field produced by all *other* core cylinders. In other words, the effective incident field on the i th core cylinder is given by

$$\sum_m (\mathbb{B}_m + B_m) \hat{\Psi}_m(k_{N+1}\mathbf{r}) + \sum_{\substack{j=1 \\ j \neq i}}^N \sum_m C_m^{(j)} \Psi(k_{N+1}\boldsymbol{\rho}_j). \quad (6.13a)$$

Using (6.2a), with $\mathbf{w} = \mathbf{r}$, $\mathbf{u} = \mathbf{r}_i$, $\mathbf{v} = \boldsymbol{\rho}_i$, and (6.2b) with $\mathbf{u} = \mathbf{r}_i - \mathbf{r}_j$, $\mathbf{v} = \boldsymbol{\rho}_j$, $\mathbf{w} = \boldsymbol{\rho}_i$, to express $\hat{\Psi}_m(k_{N+1}\mathbf{r})$ and $\Psi(k_{N+1}\boldsymbol{\rho}_j)$ in (6.13a) in the local coordinate system of the i th core cylinder yields

$$\sum_n \underbrace{\left[\mathbb{B}_n^{(i)} + B_n^{(i)} + \sum_{\substack{j=1 \\ j \neq i}}^N \sum_m C_m^{(j)} \Psi_{m-n}(k_{N+1}(\mathbf{r}_j - \mathbf{r}_i)) \right]}_{\text{expansion coefficients of the effective incident field}} \hat{\Psi}_n(k_{N+1}\boldsymbol{\rho}_i), \quad i = 1, \dots, N, \quad (6.13b)$$

where

$$\mathbb{B}_n^{(i)} + B_n^{(i)} = \sum_m (\mathbb{B}_m + B_m) \hat{\Psi}_{m-n}(k_{N+1}\mathbf{r}_i). \quad (6.14)$$

The expansion coefficients of the scattered field produced by the i th core cylinder are related to the expansion coefficients of the effective incident field via the T -matrix for the i th core cylinder and thus, we have

$$C_\ell^{(i)} = \sum_p T_{\ell p}^{(i)} \left[\mathbb{B}_p^{(i)} + B_p^{(i)} + \sum_{\substack{j=1 \\ j \neq i}}^N \sum_m O_{pm}^{(i,j)} C_m^{(j)} \right], \quad i = 1, \dots, N, \quad (6.15)$$

where

$$O_{pm}^{(i,j)} = \Psi_{m-p}(k_{N+1}(\mathbf{r}_j - \mathbf{r}_i)). \quad (6.16)$$

If we let

$$\mathcal{B} = \begin{bmatrix} \mathbf{B}^{(1)} + \mathbf{B}^{(1)} \\ \mathbf{B}^{(2)} + \mathbf{B}^{(2)} \\ \vdots \\ \mathbf{B}^{(N-1)} + \mathbf{B}^{(N-1)} \\ \mathbf{B}^{(N)} + \mathbf{B}^{(N)} \end{bmatrix}, \quad (6.17a)$$

$$\mathcal{C} = \begin{bmatrix} \mathbf{C}^{(1)} \\ \mathbf{C}^{(2)} \\ \vdots \\ \mathbf{C}^{(N-1)} \\ \mathbf{C}^{(N)} \end{bmatrix}, \quad (6.17b)$$

$$\mathcal{T} = \begin{bmatrix} \mathbf{T}^{(1)} & \mathbf{0} & \dots & \mathbf{0} & \mathbf{0} \\ \mathbf{0} & \mathbf{T}^{(2)} & \dots & \mathbf{0} & \mathbf{0} \\ \mathbf{0} & \mathbf{0} & \ddots & \mathbf{0} & \mathbf{0} \\ \mathbf{0} & \mathbf{0} & \dots & \mathbf{T}^{(N-1)} & \mathbf{0} \\ \mathbf{0} & \mathbf{0} & \dots & \mathbf{0} & \mathbf{T}^{(N)} \end{bmatrix}, \quad (6.17c)$$

and

$$\mathcal{O} = \begin{bmatrix} \mathbf{0} & \mathbf{O}^{(1,2)} & \dots & \mathbf{O}^{(1,N-1)} & \mathbf{O}^{(1,N)} \\ \mathbf{O}^{(2,1)} & \mathbf{0} & \mathbf{O}^{(2,3)} & \dots & \mathbf{O}^{(2,N)} \\ \dots & \dots & \dots & \dots & \dots \\ \mathbf{O}^{(N-1,1)} & \mathbf{O}^{(N-1,2)} & \dots & \mathbf{0} & \mathbf{O}^{(N-1,N)} \\ \mathbf{O}^{(N,1)} & \mathbf{O}^{(N,2)} & \dots & \mathbf{O}^{(N,N-1)} & \mathbf{0} \end{bmatrix}, \quad (6.17d)$$

then, in the above block matrix notation, (6.15) reads

$$[\mathbf{I} - \mathcal{T}\mathcal{O}] \mathcal{C} = \mathcal{T}\mathcal{B}, \quad (6.18)$$

where \mathbf{I} is the identity matrix. Solving (6.18) for \mathcal{C} and using $[\mathbf{I} - \mathcal{T}\mathcal{O}]^{-1} \mathcal{T} = [\mathcal{T}^{-1} (\mathbf{I} - \mathcal{T}\mathcal{O})]^{-1}$ to simplify the result, yields

$$\mathcal{C} = \mathcal{J}\mathcal{B}, \quad (6.19a)$$

where

$$\mathcal{J} = [\mathcal{T}^{-1} - \mathcal{O}]^{-1}. \quad (6.19b)$$

We will finish the derivation of the cluster T -matrix shortly, but first, a few computational remarks.

- (i) From (6.10), we see that the T -matrix for the i th core cylinder is diagonal, and thus, so is \mathcal{T} . In other words, the computation of \mathcal{T}^{-1} in (6.19b) is trivial.
- (ii) The core cylinders must be labeled in such a way so that the dominant (numerically large) $\mathbf{O}^{(i,j)}$ block matrices appear near the main diagonal of the \mathbf{O} matrix. This is important for numerical stability, as diagonally dominant matrices tend to be numerically stable during inversion.
- (iii) It is tempting to compute \mathcal{T} by expanding $[\mathcal{T}^{-1} - \mathbf{O}]^{-1}$ in the Neumann series, i.e.,

$$[\mathcal{T}^{-1} - \mathbf{O}]^{-1} = \mathcal{T} + \mathcal{T}\mathbf{O}\mathcal{T} + \mathcal{T}\mathbf{O}\mathcal{T}\mathbf{O}\mathcal{T} + \dots, \quad (6.20)$$

but this should be *avoided*. The right-hand side of (6.20) may be interpreted as an orders-of-scattering approximation and thus, a large number of terms will need to be retained during the onset of localization. Loosely speaking, localization occurs when the wave becomes trapped (undergoes a large number of bounces) inside the cluster of core cylinders. However, it is perfectly sensible to use an orders-of-scattering approximation outside the cluster of core cylinders, as we have done in Section 6.1.

Returning to the derivation of the cluster T -matrix, if we partition the \mathcal{T} matrix into N^2 block matrices and denote these block matrices by $\mathcal{T}^{(i,j)}$, where $i = 1, \dots, N$ and $j = 1, \dots, N$, then (6.19) may be written as

$$\mathbf{C}^{(i)} = \sum_{j=1}^N \mathcal{T}^{(i,j)} (\mathbf{B}^{(j)} + \mathbf{B}^{(j)}). \quad (6.21)$$

Substituting (6.14) into (6.21) yields

$$\mathbf{C}^{(i)} = \sum_{j=1}^N \mathcal{T}^{(i,j)} \hat{\mathbf{O}}^{(j)}(\mathbf{r}_j) (\mathbf{B} + \mathbf{B}), \quad (6.22)$$

where

$$\hat{\mathbf{O}}_{nm}^{(j)}(\mathbf{r}_j) = \hat{\Psi}_{m-n}(k_{N+1}\mathbf{r}_j). \quad (6.23)$$

The expansion coefficients of the scattered field produced by the i th core cylinder, $\mathbf{C}^{(i)}$, are related to the \mathbf{C} coefficients appearing in the second term on the right hand side of (6.5d). To establish this relationship, we express (6.11) in the global coordinate system by using (6.2c) with $\mathbf{u} = \mathbf{r}_i$, $\mathbf{v} = \boldsymbol{\rho}_i$, and $\mathbf{w} = \mathbf{r}$ to obtain

$$\sum_n \left[\sum_m \widehat{\Psi}_{m-n}(-k_{N+1}\mathbf{r}_i) C_m^{(i)} \right] \Psi_n(k_{N+1}\mathbf{r}), \quad |\mathbf{r}| > |\mathbf{r}_i|, \quad i = 1, \dots, N. \quad (6.24)$$

Summing (6.24) over i yields the desired relationship, namely,

$$\mathbf{C} = \sum_{i=1}^N \widehat{\boldsymbol{\Theta}}^{(i)}(-\mathbf{r}_i) \mathbf{C}^{(i)}. \quad (6.25)$$

Finally, multiplying (6.22) by $\widehat{\boldsymbol{\Theta}}^{(i)}(-\mathbf{r}_i)$, then summing the result over i , and using (6.25) yields the cluster T -matrix, namely,

$$\mathbf{T} = \sum_{i=1}^N \sum_{j=1}^N \widehat{\boldsymbol{\Theta}}^{(i)}(-\mathbf{r}_i) \mathcal{T}^{(i,j)} \widehat{\boldsymbol{\Theta}}^{(j)}(\mathbf{r}_j). \quad (6.26)$$

6.3 Connection with localization and random matrices

If we let the radius of the host cylinder go to infinity, and the radius of each core cylinder shrink to zero, then the scattering geometry shown in Figure 6.1 may be treated by Foldy's method [10]. In this extreme limit, we can treat each core cylinder as a dipole, with the field scattered by each core cylinder given by

$$k_{N+1}^2 p_i G(\mathbf{r}, \mathbf{r}_i), \quad i = 1, \dots, N, \quad (6.27)$$

where p_i is the dipole moment of the i th core cylinder, and $G(\mathbf{r}, \mathbf{r}_i)$ is the free-space Green's function. The free-space Green's function is given by [11, §2.2]

$$G(\mathbf{r}, \mathbf{r}_i) = \frac{i}{4} H_0(k_{N+1}|\mathbf{r} - \mathbf{r}_i|), \quad (6.28)$$

where we used the “negative Dirac delta function” convention in the definition of Green's function, i.e.,

$$(\nabla^2 + k_{N+1}^2) G(\mathbf{r}, \mathbf{r}') = -\delta(\mathbf{r} - \mathbf{r}').$$

To find the unknown dipole moments in (6.27), we proceed as in Section 6.2 by considering the effective incident field, $U^{(\text{eff})}(\mathbf{r}_i)$, on the i th dipole. The effective field incident on the i th dipole consists of the external incident field $U^{(\text{inc})}$, as well as the fields produced by all other dipoles; thus, we have

$$U^{(\text{eff})}(\mathbf{r}_i) = U^{(\text{inc})}(\mathbf{r}_i) + \sum_{\substack{j=1 \\ j \neq i}}^N k_{N+1}^2 p_j G(\mathbf{r}_i, \mathbf{r}_j), \quad i = 1, \dots, N. \quad (6.29)$$

If we *assume*, as Foldy did, that the dipole moment is proportional to the effective incident field¹³, i.e.,

$$p_i = \varrho_i U^{(\text{eff})}(\mathbf{r}_i), \quad (6.30)$$

then (6.29) becomes

$$U^{(\text{eff})}(\mathbf{r}_i) = U^{(\text{inc})}(\mathbf{r}_i) + \sum_{\substack{j=1 \\ j \neq i}}^N k_{N+1}^2 \varrho_j U^{(\text{eff})}(\mathbf{r}_j) G(\mathbf{r}_i, \mathbf{r}_j), \quad i = 1, \dots, N. \quad (6.31)$$

In principle, the proportionality constant ϱ_i is arbitrary. However, if we assume that each core cylinder, as well as the host medium, is non-absorbent, then conservation of energy mandates that ϱ_i must satisfy [12] [4, §8.3.1]

$$\frac{ik_{N+1}^2 \varrho_i}{2} = \exp(2i\alpha_i) - 1, \quad (6.32)$$

where α_i is the phase angle of ϱ_i . Substituting (6.28), (6.32) into (6.31), and assuming that ϱ_i is the same for each dipole (i.e., identical core cylinders) yields

$$\mathbf{F}\mathbf{U}^{(\text{eff})} = \mathbf{U}^{(\text{inc})}, \quad (6.33)$$

where

$$\mathbf{F} = \mathbf{I} - \frac{e^{2i\alpha} - 1}{2} \mathbf{G}, \quad \mathbf{U}^{(\text{eff})} = \begin{bmatrix} \mathbf{U}^{(\text{eff})}(\mathbf{r}_1) \\ \mathbf{U}^{(\text{eff})}(\mathbf{r}_2) \\ \vdots \\ \mathbf{U}^{(\text{eff})}(\mathbf{r}_N) \end{bmatrix}, \quad \mathbf{U}^{(\text{inc})} = \begin{bmatrix} U^{(\text{inc})}(\mathbf{r}_1) \\ U^{(\text{inc})}(\mathbf{r}_2) \\ \vdots \\ U^{(\text{inc})}(\mathbf{r}_N) \end{bmatrix}, \quad (6.34a)$$

¹³This assumption forces us to treat each core cylinder as an isotropic scatterer. It should be noted that it is possible to extend Foldy's method to anisotropic scatterers, as was shown by Martin [4, §8.3.3].

and

$$\mathbb{G}_{ij} = \begin{cases} H_0(k_{N+1}|\mathbf{r}_i - \mathbf{r}_j|) & \text{for } i \neq j \\ 0 & \text{for } i = j \end{cases}. \quad (6.34b)$$

From (6.33) and (6.30), we see that if \mathbf{F} has a zero eigenvalue, then $\mathbf{U}^{(\text{eff})}$ is non-zero even if $\mathbf{U}^{(\text{inc})} = \mathbf{0}$. Clearly, this state corresponds to perfect localization; we define perfect localization by vanishing of the total (scattered + incident) time-averaged energy density sufficiently far away from the cluster of core cylinders. It has been proven by Rusek *et al.* [12] that this perfect localized state *cannot* exist for a finite N . Although it is impossible to have perfect localized states, we may have quasi-localized states characterized by *almost* zero eigenvalues of \mathbf{F} . Through extensive numerical studies, Rusek *et al.* [12–14] was able to demonstrate that the density of eigenvalues of \mathbf{G} cluster near negative one for sufficiently large dipole densities. In other words, if we denote the eigenvalues of \mathbf{G} by g , then $\text{Re}(g) \approx -1$ for almost any random distribution of dipoles with sufficiently large density. Of course, the eigenvalues of \mathbf{G} are related to the eigenvalues of \mathbf{F} by

$$f = 1 - \frac{e^{2i\alpha} - 1}{2}g, \quad (6.35)$$

where f denotes the eigenvalues of \mathbf{F} , and from (6.35) we see that α may always be chosen such that $f \approx 0$ for $\text{Re}(g) \approx -1$. The choice for α is dictated by the imaginary part of g . For example, if $\text{Im}(g) = 0$ or -1 , then we may choose $\alpha = \pi/2$ or $\pi/4$, respectively, to obtain $f \approx 0$ (quasi-localized state). Furthermore, Rusek *et al.* numerically demonstrated that if the number of dipoles is increased while keeping their density constant, the eigenvalue density of \mathbf{G} approaches the $\text{Re}(g) = -1$ boundary fastest along the $\text{Im}(g) = 0$ line (resonating dipole line). It is interesting to note that very little is known about the distribution of eigenvalues of non-Hermitian random matrices such as \mathbf{G} [15]. In fact, papers devoted to this study only recently started to appear in the literature [16–19].

Returning to the original cluster of core cylinders with finite radii, we see that (6.19) is analogous to (6.33). More specifically, the role of \mathbf{F} in (6.33) is analogous to the role of $\mathcal{T}^{-1} = \mathcal{T}^{-1} - \mathbf{0}$ in (6.33); recall that \mathcal{T}^{-1} is a diagonal matrix that depends only on

the properties of the core cylinders and the \mathbf{O} matrix depends only on the relative position of the core cylinders. To the best of our knowledge, there is no formula connecting the eigenvalues of $\mathbf{T}^{-1} - \mathbf{O}$ to the eigenvalues of \mathbf{T}^{-1} and \mathbf{O} . However, the discussion in the previous paragraph suggests that quasi-localization is most likely to occur when the core cylinders are near resonance. Therefore, with a fixed “resonant” \mathbf{T}^{-1} , we can study whether there is, indeed, a signature of quasi-localization in the spectrum of \mathbf{O} . It is important to stress that our model allows us to do this numerically and *experimentally*, unlike the above mentioned Foldy-based model.

6.4 Summary

In this chapter, we have generalized the SCV approximation to the case where the host cylinder contains N eccentrically embedded core cylinders. This was accomplished via the cluster T -matrix approach. We demonstrated that the SCV approximation retains its physical interpretation, as was previously discussed in Section 5.6. Furthermore, we have discussed how our model can be used to study localization, and suggested some avenues for future research.

6.5 References Cited

- [1] B. Peterson, S. Ström, Matrix formulation of acoustic scattering from an arbitrary number of scatterers, J. Acoust. Soc. Am. 56 (1974) 771–780.
- [2] R. Lim, R. H. Hackman, A formulation of multiple scattering by many bounded obstacles using a multicentered, T supermatrix, J. Acoust. Soc. Am. 91 (1992) 613–638.
- [3] M. I. Mishchenko, L. D. Travis, A. A. Lacis, Scattering, Absorption, and Emission of Light by Small Particles, Cambridge University Press, Cambridge, 2002.
- [4] P. A. Martin, Multiple Scattering, Cambridge University Press, Cambridge, 2006.
- [5] F. W. J. Olver, D. W. Lozier, R. F. Boisvert, C. W. Clark (Eds.), NIST Handbook of Mathematical Functions, Cambridge University Press, New York, NY, 2010.

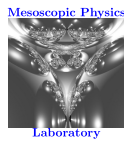
- [6] P. C. Waterman, Matrix formulation of electromagnetic scattering, *Proc. IEEE* 53 (1965) 805–812.
- [7] P. C. Waterman, New formulation of acoustic scattering, *J. Acoust. Soc. Am.* 45 (1969) 1417–1429.
- [8] M. I. Mishchenko, P. A. Martin, Peter Waterman and T -matrix methods, *J. Quant. Spectrosc. Radiat. Transfer* 123 (2013) 2–7.
- [9] M. I. Mishchenko, G. Videen, N. G. Khlebtsov, T. Wriedt, Comprehensive T -matrix reference database: A 2012–2013 update, *J. Quant. Spectrosc. Radiat. Transfer* 123 (2013) 145–152.
- [10] L. L. Foldy, The multiple scattering of waves. I. General theory of isotropic scattering by randomly distributed scatterers, *Phys. Rev.* 67 (1945) 107–119.
- [11] P. Sheng, *Introduction to Wave Scattering, Localization and Mesoscopic Phenomena*, Springer, Berlin, second edition, 2006.
- [12] M. Rusek, A. Orłowski, Analytical approach to localization of electromagnetic waves in two-dimensional random media, *Phys. Rev. E* 51 (1995) R2763–R2766.
- [13] M. Rusek, A. Orłowski, J. Mostowski, Band of localized electromagnetic waves in random arrays of dielectric cylinders, *Phys. Rev. E* 56 (1997) 4892–4895.
- [14] M. Rusek, A. Orłowski, Anderson localization of electromagnetic waves in confined dielectric media, *Phys. Rev. E* 59 (1999) 3655–3660.
- [15] M. Rusek, J. Mostowski, A. Orłowski, Random Green matrices: From proximity resonances to Anderson localization, *Phys. Rev. A* 61 (2000) 022704.
- [16] F. A. Pinheiro, M. Rusek, A. Orłowski, B. A. van Tiggelen, Probing Anderson localization of light via decay rate statistics, *Phys. Rev. E* 69 (2004) 026605.
- [17] S. E. Skipetrov, A. Goetschy, Eigenvalue distributions of large Euclidean random matrices for waves in random media, *J. Phys. A* 44 (2011) 065102.
- [18] A. Goetschy, S. E. Skipetrov, Non-Hermitian Euclidean random matrix theory, *Phys. Rev. E* 84 (2011) 011150.
- [19] A. Goetschy, S. E. Skipetrov, Euclidean random matrices and their applications in physics, *ArXiv e-prints* (2013). arXiv:1303.2880v1 [math-ph].

Modern Electromagnetic Scattering

Alex J. Yuffa
ayuffa@gmail.com

Mesoscopic Physics Laboratory
Department of Physics — Colorado School of Mines

August 20, 2013



Overview: Publications

A. J. Yuffa and J. A. Scales

Object-oriented electrodynamic S-matrix code with modern applications
Journal of Computational Physics, **231**, 4823–4835, 2012.

A. J. Yuffa and J. A. Scales

Causality and linear response in classical electrodynamics
European Journal of Physics, **33**, 1635–1650, 2012.

A. J. Yuffa and J. A. Scales

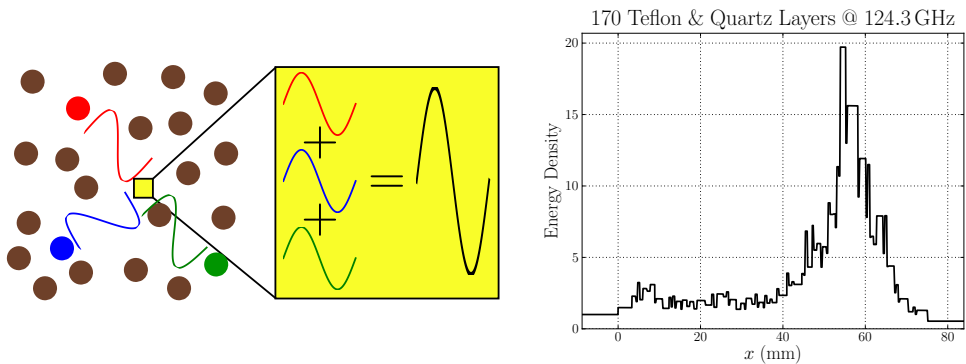
Measuring the void: Theoretical study of scattering by a cylindrical annulus
Journal of Quantitative Spectroscopy & Radiative Transfer (in press, 2013)

A. J. Yuffa, P. A. Martin, and J. A. Scales

Scattering from a large cylinder with an eccentrically embedded core: An orders-of-scattering approximation
Journal of Quantitative Spectroscopy & Radiative Transfer
(submitted in June, 2013)

Overview: Multiple scattering effects

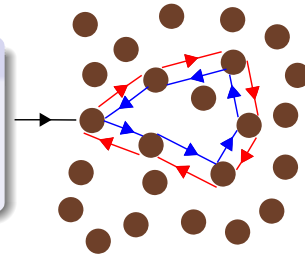
- Develop **experimentally** verifiable models
 - ▶ Theoretically sound
 - ▶ Computationally tractable
 - ▶ AB Millimetre millimeter/sub-millimeter Vector Network Analyzer
- Localization



Overview: Localization

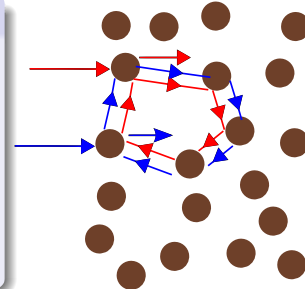
Weak localization: Coherent backscattering

- Time-reversed paths
- Configurational Average
 - ▶ Time-reversed paths survive: Factor of 2

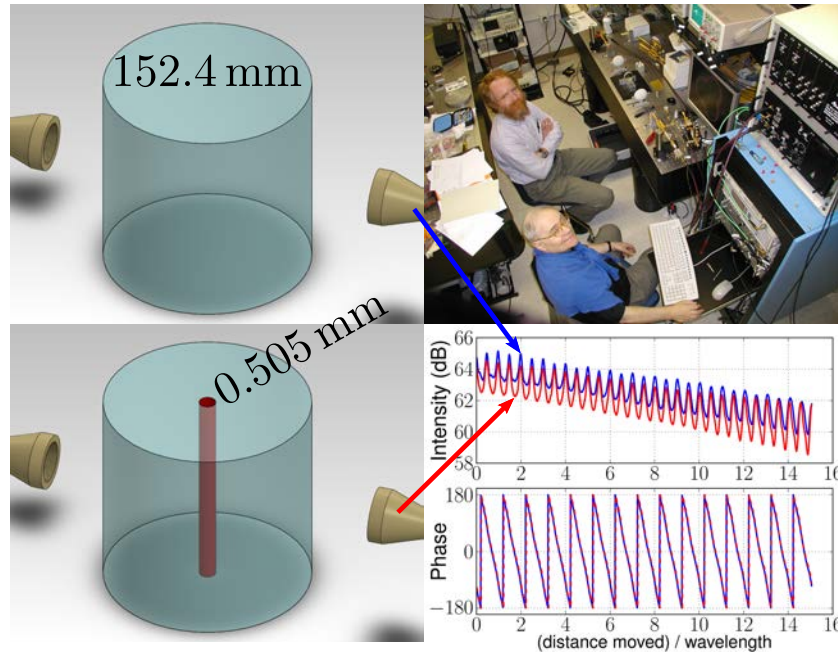


Strong localization: Anderson localization

- Coherent forward scattering
- Scaling theory
 - ▶ $T \sim \exp\left(-\frac{\text{sys. size}}{\text{loc. length}}\right)$
- Ioffe–Regel criterion
 - ▶ two/three scatterers per wavelength

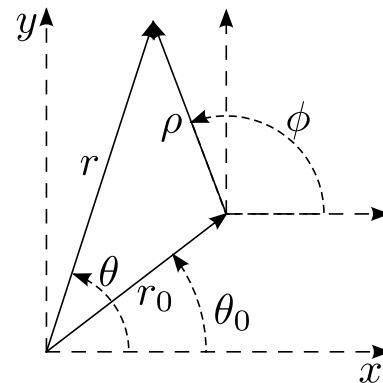


What can we measure?

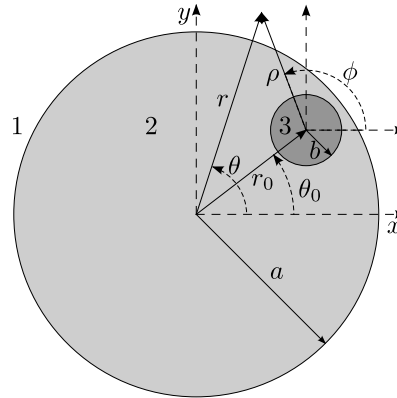


Graf's addition theorems

- $\hat{\Psi}_n(k\mathbf{r}) = J_n(kr)e^{in\theta}$
 - ▶ $\hat{\Psi}_m(k\mathbf{r}) = \sum_n \hat{\Psi}_n(k\boldsymbol{\rho})\hat{\mathcal{O}}_{nm}(\mathbf{r}_0)$
- $\Psi_n(k\mathbf{r}) = H_n(kr)e^{in\theta}$
 - ▶ $\Psi_m(k\boldsymbol{\rho}) = \sum_n \Psi_n(k\mathbf{r})\hat{\mathcal{O}}_{nm}(-\mathbf{r}_0), \quad r > r_0$
- $\hat{\mathcal{O}}_{nm}(\mathbf{r}_0) = \hat{\Psi}_{m-n}(k\mathbf{r}_0)$
- Regular wavefunction: $\hat{\Psi}$
- Outgoing wavefunction: Ψ
- Mode-mixing



Scattering by a small core cylinder inside of a host cylinder



$$U^{(1)}(\mathbf{r}) = \underbrace{\mathbb{U}^{(1)}(\mathbf{r})}_{\text{host cyl.}} + V^{(\text{sca})}(\mathbf{r})$$

$$U^{(2)}(\mathbf{r}; \boldsymbol{\rho}) = \underbrace{\mathbb{U}^{(2)}(\mathbf{r})}_{\text{host cyl.}} + V^{(2)}(\mathbf{r}; \boldsymbol{\rho})$$

$$U^{(3)}(\boldsymbol{\rho}) = V^{(3)}(\boldsymbol{\rho})$$

Host cylinder

$$\mathbb{U}^{(\text{inc})}(\mathbf{r}) = \sum_m \mathbb{D}_m \hat{\Psi}_m(\mathbf{r})$$

$$\mathbb{U}^{(\text{sca})}(\mathbf{r}) = \sum_m \mathbb{A}_m \Psi_m(\mathbf{r})$$

$$\mathbb{U}^{(2)}(\mathbf{r}) = \sum_m \mathbb{B}_m \hat{\Psi}_m(\mathbf{r})$$

- Continuity conditions on $r = a$

► $\mathbb{U}^{(1)} = \mathbb{U}^{(2)}$ and $\frac{\partial}{\partial r} \mathbb{U}^{(1)} = \frac{\partial}{\partial r} \mathbb{U}^{(2)}$

$$\mathbb{A}_m = -\frac{\{J_{m+1}(k_1 a); J_m(k_2 a)\}}{\{H_{m+1}(k_1 a); J_m(k_2 a)\}} \mathbb{D}_m$$

$$\mathbb{B}_m = \frac{-2i}{\pi k_1 a \{H_{m+1}(k_1 a); J_m(k_2 a)\}} \mathbb{D}_m$$

- Curly bracket notation

$$\{f_{m+1}(u); g_m(v)\} \equiv f_{m+1}(u)g_m(v) - \frac{v}{u} f_m(u)g_{m+1}(v)$$

Composite cylinder

$$V^{(\text{sca})}(\mathbf{r}) = \sum_m A_m \Psi_m(k_1 \mathbf{r})$$

$$V^{(2)}(\mathbf{r}; \boldsymbol{\rho}) = \sum_m \left(B_m \hat{\Psi}_m(k_2 \mathbf{r}) + C_m \Psi_m(k_2 \boldsymbol{\rho}) \right)$$

$$V^{(3)}(\boldsymbol{\rho}) = \sum_m D_m \hat{\Psi}_m(k_3 \boldsymbol{\rho})$$

- Continuity conditions on $r = a$ & on $\rho = b$

- ▶ Graf's addition theorems

$$\sum_n (\delta_{mn} - F_{mn}) A_n = G_m$$

$$\mathbb{D}_m F_{mn} = \frac{\pi k_1 a}{2i} \mathbb{B}_m \left(\sum_p \hat{\mathcal{O}}_{mp}(-\mathbf{r}_0) \Delta_p \hat{\mathcal{O}}_{pn}(\mathbf{r}_0) \right) \{H_{n+1}(k_1 a); H_n(k_2 a)\}$$

$$\mathbb{D}_m G_m = \sum_n \mathbb{B}_m \left(\sum_p \hat{\mathcal{O}}_{mp}(-\mathbf{r}_0) \Delta_p \hat{\mathcal{O}}_{pn}(\mathbf{r}_0) \right) \mathbb{B}_n$$

Composite cylinder cont'd

- Core cylinder's contribution is **small & contained** in

$$\Delta_p = - \frac{\{J_{p+1}(k_3 b); J_p(k_2 b)\}}{\{J_{p+1}(k_3 b); H_p(k_2 b)\}}.$$

- If the spectral radius of \mathbf{F} is < 1

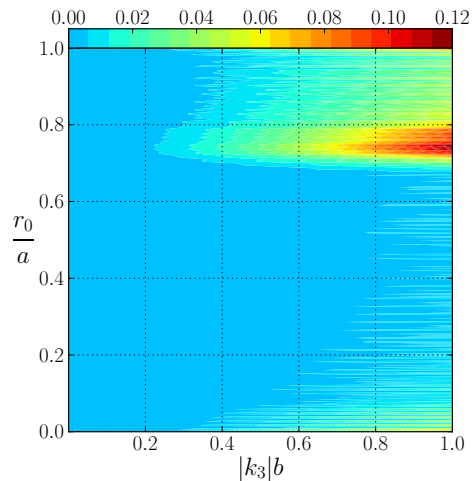
- ▶ $\mathbf{A} = (\mathbf{I} - \mathbf{F})^{-1} \mathbf{G} = \sum_{\ell=0}^{\infty} \mathbf{F}^{\ell} \mathbf{G}$

- Teflon host cylinder

- ▶ Radius 10 cm, $k_2 a \approx 300$
 - ▶ Permittivity 2.1 at 100 GHz

- Quartz core cylinder

- ▶ Permittivity 3.8 at 100 GHz



Physical interpretation of the SCV approximation

- SCV (orders-of-scattering) approximation: $\ell = 0$

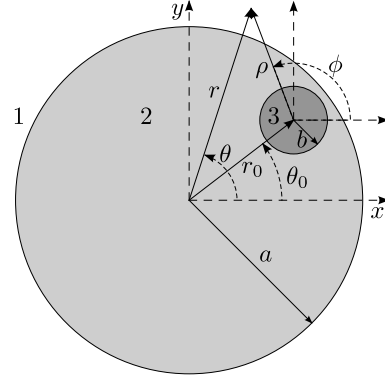
$$A_m \cong G_m = \sum_{n,p} \mathbb{B}_m \hat{\mathcal{O}}_{mp}(-\mathbf{r}_0) \Delta_p \hat{\mathcal{O}}_{pn}(\mathbf{r}_0) \mathbb{B}_n$$

- Physical interpretation

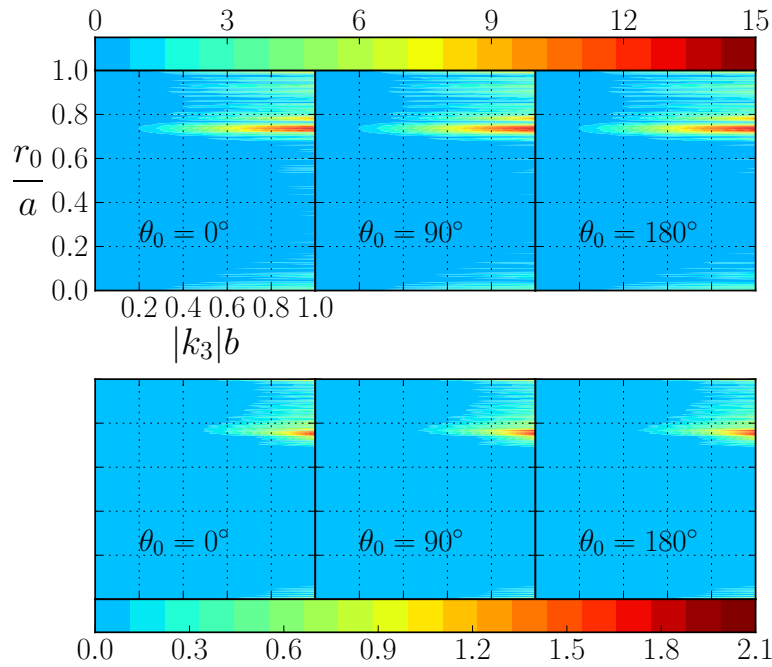
- ▶ $\hat{\mathcal{O}}_{pn}(\mathbf{r}_0) \mathbb{B}_n$ is the “screening” effect of the host cylinder on $\mathbb{U}^{(\text{inc})}$
- ▶ $\mathbb{B}_m \hat{\mathcal{O}}_{mp}(-\mathbf{r}_0)$ is the “screening” effect of the host cylinder on $V^{(\text{sca})}$

- Concentric cylinders: $\mathbf{r}_0 = \mathbf{0}$

- ▶ $\hat{\mathcal{O}}_{mp} = \delta_{mp}$ and $\hat{\mathcal{O}}_{pn} = \delta_{pn}$
- ▶ $A_m = \mathbb{B}_m \Delta_m \mathbb{B}_m$



Relative error in energy



Host cylinder: Morphological-dependent resonances

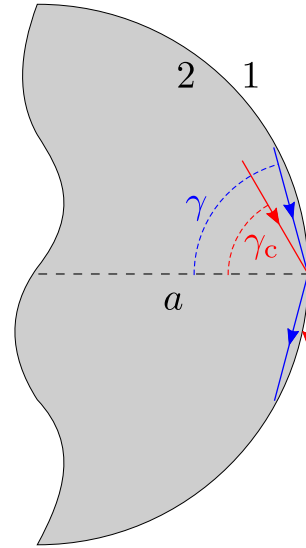
- Host cylinder \gg wavelength
 - ▶ Ray theory
- Caustic radius
 - ▶ Ray's angular momentum: $|k_{2,\theta}|r\hbar$
 - ▶ m th eigenmode angular momentum: $|m|\hbar$
 - ▶ $k_{2,r}(r = r_{\text{caustic}}) = 0$

$$r_{\text{caustic}} = \left| \frac{m}{k_2} \right|$$

- Bound on m
 - ▶ Ray's angular momentum: $|k_2|a \sin \gamma$
 - ▶ Total internal reflection: $\sqrt{\epsilon_1/\epsilon_2} \leq \sin \gamma \leq 1$

$$|k_1|a \leq m \leq |k_2|a$$

- SCV approximation: $r_0 < r_{\text{caustic}}$
 - ▶ $r_{\text{caustic}} \geq |k_1/k_2|a \approx 0.7a$

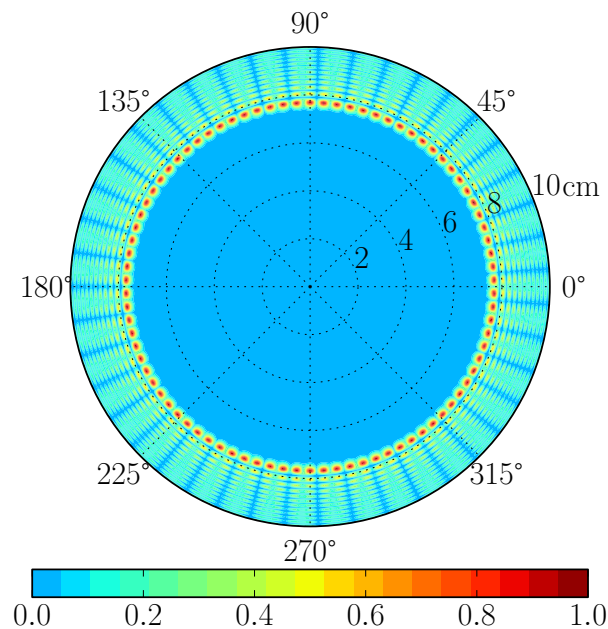


Host cylinder resonance: Energy density

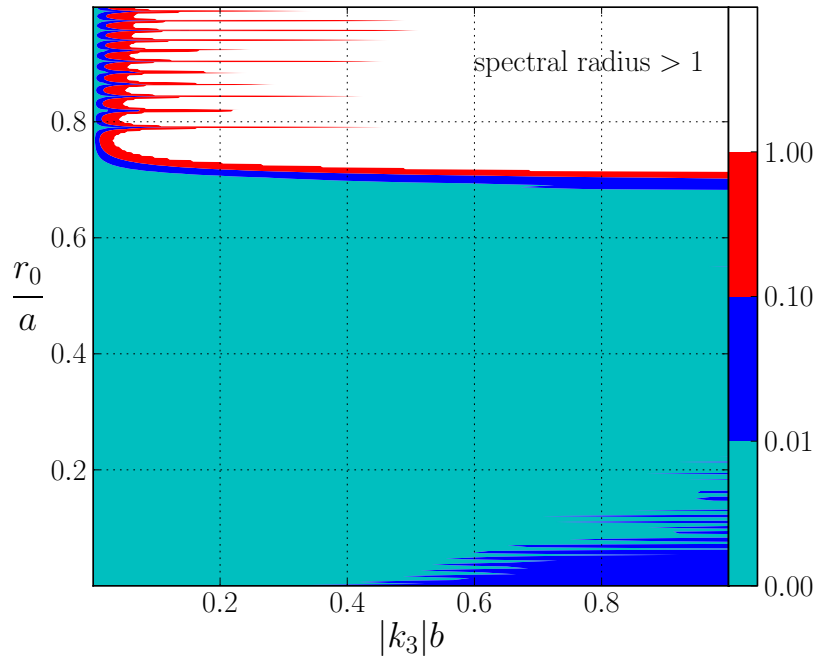
- Eigenmode
 - ▶ $m = 228$
 - ▶ 99.82385859... GHz

- Caustic radius

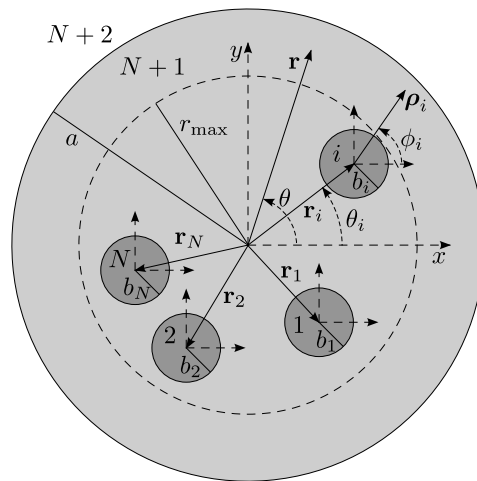
$$r_{\text{caustic}} = \frac{228}{k_2} \approx 7.5$$



Host cylinder resonance: Spectral radius



Scattering by a cluster of eccentrically embedded cores



$$U^{(N+2)}(\mathbf{r}) = \underbrace{\mathbb{U}^{(N+2)}(\mathbf{r})}_{\text{host cyl.}} + V^{(\text{sca})}(\mathbf{r})$$

$$U^{(N+1)}(\mathbf{r}) = \underbrace{\mathbb{U}^{(N+1)}(\mathbf{r})}_{\text{host cyl.}} + \underbrace{V^{(N+1)}(\mathbf{r})}_{r_{\max} \leq r < a}$$

N core cluster

$$V^{(\text{sca})}(\mathbf{r}) = \sum_m \mathbf{A}_m \Psi_m(k_{N+2}\mathbf{r})$$

$$V^{(N+1)}(\mathbf{r}) = \sum_m \left[B_m \hat{\Psi}_m(k_{N+1}\mathbf{r}) + C_m \Psi_m(k_{N+1}\mathbf{r}) \right]$$

- Physical interpretation

- Cluster's incident field

$$\mathbb{U}^{(N+1)}(\mathbf{r}) + \sum_m B_m \hat{\Psi}_m(k_{N+1}\mathbf{r})$$

- Cluster's scattered field

$$\sum_m C_m \Psi_m(k_{N+1}\mathbf{r})$$

- Cluster T -matrix

- Incident and scattered coefficients **must be linearly related**

$$C_m = \sum_n T_{mn} (\mathbb{B}_n + B_n)$$

N core cluster cont'd

- Continuity conditions on $r = a$
- Definition of the cluster T -matrix

$$\sum_n (\delta_{mn} - F_{mn}) \mathbf{A}_n = G_m$$

$$\mathbb{D}_m G_m = \sum_n \mathbb{B}_m \mathbf{T}_{mn} \mathbb{B}_n$$

$$\mathbb{D}_m F_{mn} = \frac{\pi k_{N+2} a}{2i} \mathbb{B}_m \mathbf{T}_{mn} \{H_{n+1}(k_{N+2}a); H_n(k_{N+1}a)\}$$

- Same linear system as before

$$\left(\sum_p \hat{\mathcal{O}}_{mp}(-\mathbf{r}_0) \Delta_p \hat{\mathcal{O}}_{pn}(\mathbf{r}_0) \right) \rightarrow T_{mn}$$

- \mathbf{T}_{mn} is unknown

Cluster T -matrix: i th core cylinder

- Scattered field by the i th core cylinder

$$\sum_m C_m^{(i)} \Psi(k_{N+1} \boldsymbol{\rho}_i)$$

- Effective incident field

$$\underbrace{\sum_m (\mathbb{B}_m + B_m) \hat{\Psi}_m(k_{N+1} \mathbf{r})}_{\text{"external" incident field}} + \underbrace{\sum_{j=1, j \neq i}^N \sum_m C_m^{(j)} \Psi(k_{N+1} \boldsymbol{\rho}_j)}_{\text{scattered by all other core cyl.}}$$

- T -matrix: i th core cylinder

$$C_\ell^{(i)} = \sum_p T_{\ell p}^{(i)} \left[\mathbb{B}_p^{(i)} + B_p^{(i)} + \sum_{j=1, j \neq i}^N \sum_m O_{pm}^{(i,j)} C_m^{(j)} \right], \quad i = 1, \dots, N$$

$$T_{nm}^{(i)} = -\frac{\{J_{n+1}(k_{N+1} b_i); J_m(k_i b_i)\}}{\{H_{n+1}(k_{N+1} b_i); J_m(k_i b_i)\}} \delta_{nm}, \quad O_{pm}^{(i,j)} = \Psi_{m-p}(k_{N+1}(\mathbf{r}_j - \mathbf{r}_i))$$

Cluster T -matrix: Block matrices

$$\boxed{\mathbf{c} = \overbrace{[\mathcal{T}^{-1} - \mathcal{O}]^{-1}}^{\equiv \mathcal{I}} \mathcal{B}}, \quad \mathbf{c} = \begin{bmatrix} \mathbf{C}^{(1)} \\ \mathbf{C}^{(2)} \\ \vdots \\ \mathbf{C}^{(N-1)} \\ \mathbf{C}^{(N)} \end{bmatrix}, \quad \mathcal{B} = \begin{bmatrix} \mathbb{B}^{(1)} + \mathbf{B}^{(1)} \\ \mathbb{B}^{(2)} + \mathbf{B}^{(2)} \\ \vdots \\ \mathbb{B}^{(N-1)} + \mathbf{B}^{(N-1)} \\ \mathbb{B}^{(N)} + \mathbf{B}^{(N)} \end{bmatrix}$$

$$\mathcal{T} = \begin{bmatrix} \mathbf{T}^{(1)} & \mathbf{0} & \dots & \mathbf{0} & \mathbf{0} \\ \mathbf{0} & \mathbf{T}^{(2)} & \dots & \mathbf{0} & \mathbf{0} \\ \mathbf{0} & \mathbf{0} & \ddots & \mathbf{0} & \mathbf{0} \\ \mathbf{0} & \mathbf{0} & \dots & \mathbf{T}^{(N-1)} & \mathbf{0} \\ \mathbf{0} & \mathbf{0} & \dots & \mathbf{0} & \mathbf{T}^{(N)} \end{bmatrix}$$

$$\mathcal{O} = \begin{bmatrix} \mathbf{0} & \mathbf{O}^{(1,2)} & \dots & \mathbf{O}^{(1,N-1)} & \mathbf{O}^{(1,N)} \\ \mathbf{O}^{(2,1)} & \mathbf{0} & \mathbf{O}^{(2,3)} & \dots & \mathbf{O}^{(2,N)} \\ \dots & \dots & \dots & \dots & \dots \\ \mathbf{O}^{(N-1,1)} & \mathbf{O}^{(N-1,2)} & \dots & \mathbf{0} & \mathbf{O}^{(N-1,N)} \\ \mathbf{O}^{(N,1)} & \mathbf{O}^{(N,2)} & \dots & \mathbf{O}^{(N,N-1)} & \mathbf{0} \end{bmatrix}$$

Cluster T -matrix: Block matrices cont'd

- Global coordinate system: ρ_i to \mathbf{r}

$$\mathbf{T} = \sum_{i=1}^N \sum_{j=1}^N \hat{\mathbf{O}}^{(i)}(-\mathbf{r}_i) \mathcal{T}^{(i,j)} \hat{\mathbf{O}}^{(j)}(\mathbf{r}_j)$$

- ▶ $\mathcal{T}^{(i,j)}$ block matrices

$$\mathcal{T} = \begin{bmatrix} \mathcal{T}^{(1,1)} & \mathcal{T}^{(1,2)} & \dots & \mathcal{T}^{(1,N)} \\ \mathcal{T}^{(2,1)} & \mathcal{T}^{(2,2)} & \dots & \mathcal{T}^{(2,N)} \\ \vdots & \vdots & \ddots & \vdots \\ \mathcal{T}^{(N,1)} & \mathcal{T}^{(N,2)} & \dots & \mathcal{T}^{(N,N)} \end{bmatrix}$$

- Compare \mathbf{T} to one eccentrically embedded core cylinder

Random matrices connection

- Foldy's method: Isotropic point scatterers

- ▶ Assume dipole moment: $p_i = \rho_i U^{(\text{eff})}(\mathbf{r}_i)$
- ▶ Conservation of energy: $ik_{N+1}^2 \rho_i = 2 \exp(2i\alpha_i) - 2$

$$\underbrace{\left[\mathbf{I} - \frac{e^{2i\alpha} - 1}{2} \mathbf{G} \right]}_{\equiv \mathbf{F}} \mathbf{U}^{(\text{eff})} = \mathbf{U}^{(\text{inc})}; \quad \mathbb{G}_{ij} = \begin{cases} H_0(k_{N+1} |\mathbf{r}_i - \mathbf{r}_j|) & \text{if } i \neq j \\ 0 & \text{if } i = j \end{cases}$$

- Quasi-localized state: Eigenvalues of $\mathbf{F} \approx 0$

- ▶ Real part of eigenvalues of $\mathbf{G} \approx -1$
- ▶ Choose α : Resonating dipole

Rusek *et al.* PRE **51**, 1995

Rusek *et al.* PRE **56**, 1997

Outlook and Summary

Outlook

- Role of \mathbf{F} : $\mathcal{T}^{-1} - \mathbf{0}$
 - Non-Hermitian
 - \mathcal{T}^{-1} diagonal but $[\mathcal{T}^{-1}, \mathbf{0}] \neq [\mathbf{0}, \mathcal{T}^{-1}]$
- Role of \mathbf{G} : $\mathbf{0}$
- Eigenvalues of random matrices
 - Localization signature in the spectrum

Summary

- Produced 3 + 1 publications
- Created start-of-the-art open-source E&M software
- Analyzed interplay between absorption and causality
- Developed experimentally verifiable model to study localization

Thank you!

Questions/Comments?

APPENDIX B - PERMISSIONS TO USE COPYRIGHTED MATERIAL

1. Chapter 2. *Object-oriented electrodynamic S-matrix code with modern applications*, A. J. Yuffa and J. A. Scales, Journal of Computational Physics **231**, 4823–4835 (2012), [doi:10.1016/j.jcp.2012.03.018](https://doi.org/10.1016/j.jcp.2012.03.018). Copyright (2012) by Elsevier Inc. Permission is provided by Elsevier according to the [Elsevier copyright policy](#).
2. Chapter 3. *Causality and linear response in classical electrodynamics*, A. J. Yuffa and J. A. Scales, European Journal of Physics **33**, 1635–1650 (2012), [doi:10.1088/0143-0807/33/6/1635](https://doi.org/10.1088/0143-0807/33/6/1635). Copyright (2012) by IOP Publishing Ltd. Permission is provided by IOP Publishing Limited according to the [IOP copyright notice](#).
3. Chapter 4. *Measuring the void: Theoretical study of scattering by a cylindrical annulus*, A. J. Yuffa and J. A. Scales, Journal of Quantitative Spectroscopy & Radiative Transfer (2013), [doi:10.1016/j.jqsrt.2013.02.017](https://doi.org/10.1016/j.jqsrt.2013.02.017). Copyright (2013) by Elsevier Inc. Permission is provided by Elsevier according to the [Elsevier copyright policy](#).
4. Chapter 5. *Scattering from a large cylinder with an eccentrically embedded core: An orders-of-scattering approximation*, Journal of Quantitative Spectroscopy & Radiative Transfer, under review. Permission is provided by Elsevier according to the [Elsevier copyright policy](#).